UNIVERSITY OF ALABAMA IN HUNTSVILLE

FINAL RESEARCH REPORT

NUMERICAL STUDIES OF SURFACE TENSIONS

Supported by NASA Grant Number: NAG8-938

Prepared by R.J. Hung, Ph.D.
The University of Alabama in Huntsville
Huntsville, Alabama 35899

Submitted to NASA/Marshall Space Flight Center
Huntsville, Alabama 35812

Submitted by University of Alabama in Huntsville
Huntsville, Alabama 35899

September 1995

Abstract

Liquid-vapor (bubble) interface disturbances caused by various types of accelerations, including centrifugal, lateral and axial impulses, gravity gradient and g-jitter accelerations associated with spinning and slew motion in microgravity, have been reviewed. Understanding of bubble deformations and its fluctuations are important in the development of spacecraft orbital and attitude control techniques to secure its normal operation. This review discusses bubble deformations and oscillations driven by various forces in microgravity environment. The corresponding bubble mass center fluctuations and slosh reaction forces and torques due to bubble deformations have also been reviewed.

Acknowledgements

The author appreciates the support received from the National Aeronautics and Space Administration/George C. Marshall Space Flight Center (NASA/MSFC) through the NASA Grant Number: NAG8-938. He would like to express his heartly appreciation to the contractive lengthy suggestions and discussions provided by Fred W. Leslie of NASA/MSFC.

CONTENTS

I. Introduction

For the purpose to carry out scientific experiments, some experimental spacecraft use cryogenic cooling for observation instrumentation and telescope, superconducting sensors for gyro read-out and maintain very low temperature near absolute zero for mechanical stability. The approaches to both cooling and control involve the use of superfluid liquid helium II. In this work, sloshing dynamics associated with spinning and/or slew motions are reviewed and investigated. The potential problems for cryogenic liquid in dewar container could be due to asymmetry in the static liquid helium distribution and to perturbations in the liquid-vapor interface (bubble) caused by slosh wave excitation driven by pointing control, machinery vibration, etc.

With liquid helium II, at a temperature below a λ-point (2.17 K), there is negligibly small temperature gradients. In the absence of temperature gradient along the surface which drive Marangoni convection, the equilibrium shape of the free surface is governed by a balance of capillary, centrifugal and gravitational forces. Determination of liquid-vapor interface (bubble) profiles based on computational experiments can uncover details of the flow which can not be easily visualized or measured experimentally in a microgravity environment.

The instability of the liquid-vapor interface surface can be induced by the presence of longitudinal and lateral accelerations. Slosh waves are, thus, excited which produces high and low frequency oscillations in the liquid systems. The sources of the residual accelerations range from the effects of the Earth's gravity gradient[1-3] and g-jitter[4] accelerations which include, atmospheric drag on the spacecraft, vibration of compressor, spacecraft attitude motions arising from machinery vibrations, thruster firings, spacecraft slew motion, pointing control of spacecraft, crew motion, etc. A recent study[5] suggests that the high frequency accelerations may be unimportant in comparison to the residual motions caused by low frequency accelerations.

Time-dependent dynamical behavior of partially-filled rotating fluids in reduced gravity environments was simulated by numerically solving the Navier Stokes equations subject to the initial and boundary conditions[6-20]. At this interface between the liquid and the vapor fluids, both the kinematic surface boundary condition, and the interface stress conditions for components tangential and normal to the interface, were applied[10-15]. The initial conditions were adopted from the steady-state formulations developed by Hung et al[7-9]. Some of the steady-state formulations of interface shapes were compared with the available experiments carried out by Leslie[21] in a free-falling aircraft (KC-135). The experiments carried out by Mason et al[22] showed that the classical fluid mechanics theory is applicable for cryogenic liquid helium with sufficiently large velocities, exceeding critical velocity, and also in the larger containers[23-25]. As to the dynamical behavior of cryogenic helium bubble deformations in microgravity, there is only very limited numbers of poor quality record for the scientific experimental observation available in a very short time interval and in reduced but not microgravity environment[26],. It is anticipated that microgravity experiments will be carried in the near future shuttle flights by NASA scientists. In the computer code validation, results of model computation for cryogenic liquid draining and shut-off in reduced gravity with geyser excitation have been compared with experimental observation with excellent agreement[27]. However, the results of mathematical modelling is still urgently important to provide the key data for the design of the scientific spacecraft , in particular, for their design of guidance and attitude control systems.

During the spacecraft orbit around the Earth, the direction of azimuth angle of Earth toward the location of the spacecraft mass center varies from 0° along the spin axis of spacecraft to a full circle of 360° which requires the adaptation of three dimensional calculation.

As the spacecraft moves along the orbit, any fluid capable of motion

relative to the spacecraft is subject to the acceleration that arises from the gravity gradients of the Earth which is essentially tidal in nature. Detailed description of the characteristics of gravity gradient will be given in Section(II-D). The interaction between the mass of fluid element and the spacecraft mass due to gravity gradient accelerations[1-3] are capable to excite slosh waves and induce the fluctuations of slosh reaction forces and its moment acting on the dewar of spacecraft fluid systems. Slosh wave excitations in a spinning container of a linearized fluid have been carried out by Bauer[28,29].

At temperatures close to absolute zero, quantum effects begin to be of importance in the properties of fluids. At a temperature of 2.17 K, liquid helium has a λ-point (a second-order phase transition); at temperatures below this point, liquid helium (helium II) has a number of remarkable properties, the most important of which is superfluidity. This is the property of being able to flow without viscosity in narrow capillaries or gaps. At temperatures other than zero, helium II behaves as if it were a mixture of two different liquids. One of these is a superfluid and moves with zero viscosity along a solid surface. The other is a normal viscous fluid. The two motions occur without any transfer of momentum from one to another for velocities below a critical velocity[23-25]. For the components of normal and superfluid velocities above a critical velocity, the two fluids are coupled[23-25].

Experiment made by Andronikashvili[23,24] for rotating helium II shows that it is necessary to exceed a critical velocity for the interaction between the normal and superfluid components to establish entire bucket in rotation[23,24]. This is due to the fact that the high fluid velocity can produce great enough vortex lines to snarl in a complex tangle to assure and interaction between the normal and superfluid components[23-25,28,29]. For the rotating dewar with outer diameter of 1.56 m and inner diameter of 0.276 m, the critical velocities to assume the interaction between the normal and super-fluid components are 6.4×10^{-7}

and 3.6×10^{-6} m/s, respectively[23,24]. With rotating speed of 0.1 rpm, the linear velocities along the outer and inner walls of rotating dewar are 8.17×10^{-3} and 1.45×10^{-3} m/s, respectively, which are at least several hundred times greater than that of the corresponding critical velocities to assure the interaction between the normal and superfluid components of helium II. These vortex lines snarling with a complex tangle between the normal and superfluid components warrant the adoption of Newtonian fluid model[23-25].Based on this illustration, the problem under consideration have the special features to warrant an adoption of viscous Newtonian fluids formulation in this study.

Density concentration of superfluid is a function of temperature, which is also true for the surface tension and viscous coefficient for helium II[30,31]. In general two fluid model shall be adopted to compare the dynamical behavior of helium II. For the cases with fluid velocities exceed a critical velocity, single fluid model can be employed. In this study, the theory of viscous Newtonian fluids is employed with modification of transport coefficients adjusted by normal and superfluid density concentration which is a function of temperature. Most of the research works pertaining to the cryogenic helium sloshing dynamics in microgravity are carried out by NASA Marshall Space Flight Center (NASA/MSCF), while some of the cryogenics hydrogen sloshing dynamiics in reduced gravity are operated by NASA Lewis Research Center[26]. Majority of the present works of cryogenics helium II are based on the works accompanied by a group of scientists, affiliated with the NASA/MSCF in the past 8 years. In addition to the application of helium II sloshing dynamics with velocities exceeding critical velocity in microgravity, present works are also fully applicable to sloshing dynamics with regular Newtonian fluids.

For the purpose of examining the sloshing dynamics affected liquid-vapor interface in a partially liquid-filled dewar subject to various conditions of spacecraft orbiting around the Earth, examples are given to illustrate the

dynamics of bubble deformations under the following conditions: (1) Bubble spin-up from rest with and without a completion of wrapping around the well of rotating dewar, (2) Bubble spin-down from steady state with wrapping around central column of rotating dewar, (3) Rotating bubble subject to lateral and axial impulses, (4) Bubble subject to gravity gradient or g-jitter accelerations associated with slew motion, and (5) Rotating bubble subject to various magnitudes of combined gravity gradient and g-jitter accelerations.

Dynamics of Bubble deformation introduce additional problems of spacecraft orbital mechanics in guidance and attitude controls under microgravity environment. These problems include: (a) bubble mass center fluctuations, and (b) fluctuations of slosh reaction forces and torques exerted on the liquid container of spacecraft fluid systems due to bubble deformations. In this review paper, it is our intention to discuss (a) the cross-linkage between bubble deformation driven by various orbital accelerations and their impacts on bubble mass center fluctuations, and (b) the corresponding fluctuations of slosh reaction forces and torques acting on the fluid container due to bubble deformations. Better understanding of these linkages is a key to develop the reliable spacecraft guidance and attitude control techniques.

Present research has resulted in numerous refereed journal article publications. List of journal article publications sponsored by present NASA Grant Number: NAG8-938 are as follows:

(1) Hung, R. J., and Shyu, K. L., Constant Reverse Thrust Activated Reorientation of Liquid Hydrogen with Geyser Initiation, Journal of Spacecraft and Rockets, 29, 279-285, 1992.

(2) Hung, R. J., and Shyu, K. L., Fluid Resettlement and Slosh Wave Excitement During the Spacecraft Reorientation in Cryogenic Propellant System, Proceedings of National Science Council (A), 16, 131-148, 1992.

(3) Hung, R. J., Lee, C. C., and Leslie, F. W., Spacecraft Dynamical Distribution of Fluid Stresses Activated by Gravity Jitters Induced Slosh Waves, Journal of Guidance, Control and Dynamics, 15, 817-824, 1992.

(4) Hung, R. J., Shyu, K. L., Lee, C. C., Liquid Hydrogen Slosh Wave Excited by Constant Reverse Gravity Acceleration of Geyser Initiation, Journal of Spacecraft and Rockets, 29, 523-528, 1992.

(5) Hung, R. J., Shyu, K. L., and Lee, C. C., Medium Frequency Impulsive Thrust Excited Slosh Waves During Propellant Reorientation with Geyser, Journal of Propulsion and Power, 8, 778-785, 1992.

(6) Hung, R. J., and Shyu, K. L., Excitation of Slosh Waves Associated with Low Frequency Impulsive

Reverse Gravity Acceleration of Geyser Initiation, Acta Astronautica, 26, 425-433, 1992.

(7) Hung, R. J., and Lee, C. C., Characteristics and Behaviors of Gravity Probe-B Spacecraft Propulsion System, Proceedings of National Science Council (A), 16, 239-252, 1992.

(8) Hung, R. J., and Shyu, K. L., Suction Dip, Liquid Residual and Liquid Propellant Shut-Off in Spacecraft Propulsion System, Proceedings of National Science Council (A), 16, 347-364, 1992.

(9) Hung, R. J., Lee, C. C., and Leslie, F. W., Similarity Rules in Gravity Jitter-Related Spacecraft Liquid Propellant Slosh Waves Excitation, Journal of Fluids and Structures, 6, 493-522, 1992.

(10) Hung, R. J., and Shyu, K. L., Medium Frequency Impulsive Thrust Activated Liquid Hydrogen Reorientation with Geyser, Journal of Propulsion and Power, 8, 987-994, 1992.

(11) Hung, R. J., Lee, C. C., and Leslie, F. W., Effect of the Baffle on the Spacecraft Fluid Propellant Viscous Stress and Moment Fluctuations, Transactions of the Japan Society for Aeronautical and Space Sciences, 35, 187-207, 1993.

(12) Hung, R. J., and Shyu, K. L., Suction Dip, Liquid Residual and Slosh Wave Excitation During Liquid Draining in Microgravity, Advances in Space Research, 13(7), 147-154, 1993.

(13) Hung, R. J., and Shyu, K. L., Liquid Settlement, Resettlement, Slosh Wave Excitation and Geyser Motion During Reorientation in Microgravity, Advances in Space Research, 13(7), 155-163, 1993.

(14) Hung, R. J., Lee, C. C., and Leslie, F. W., Effect of the Baffle on the Asymmetric Gravity-Jitter Excited Slosh Waves and Spacecraft Moment and Angular Momentum Fluctuations, Journal of Aerospace Engineering, (United Kingdom), 207, 105-120, 1993.

(15) Hung, R. J., and Pan, H. L., Asymmetric Slosh Wave Excitation in Liquid-Vapor Interface Under Microgravity, Acta Mechanica Sinica, 9(4), 298-311, 1993.

(16) Hung, R. J., and Lee, C. C., Effect of the Baffle on On-Orbit Spacecraft Fluid System Angular Momentum Fluctuations and Action of Viscous Stress Moment Exerted on the Container, Proceedings of National Science Council (A), 17, 214-235, 1993.

(17) Hung, R. J., and Pan, H. L., Differences in Gravity Gradient and Gravity Jitter-Excited Slosh Waves in Microgravity, Transactions of the Japan Society for Aeronautical and Space Sciences, 36, 153-169, 1993.

(18) Hung, R. J., and Shyu, K. L., Liquid Hydrogen Shut-Off Geyser Excitation Induced by Sloshing Dynamics During Draining in Microgravity. Aeronautical Journal (Royal Aeronautical Society of United Kingdom),98, No.977, 237-250, 1994.

(19) Hung, R. J., and Pan, H. L., Gravity Gradient or Gravity Jitter Induced Viscous Stress and Moment Fluctuations in Microgravity, Fluid Dynamics Research, 14(1), 29-51, 1994.

(20) Hung, R. J., and Pan, H. L., Cryogenic Helium System Angular Momentum and Moment Fluctuations Driven by Gravity Gradient Acceleration in Microgravity, Advances in Cryogenic Engineering, 39, 231-240, 1994.

(21) Hung, R. J., and Lee, C. C., Effect of the Baffle on the Cryogenic Helium Container Angular Momentum and Moment Fluctuations Due to Asymmetric Gravity Jitter Excited Slosh Waves, Advances in Cryogenic Engineering, 39, 261-270, 1994.

(22) Hung, R. J., and Pan, H. L., Gravity Gradient Induced Viscous Stress and Moment Fluctuations of Cryogenic Helium System in Microgravity, Advances in Cryogenic Engineering, 39, 241-250, 1994.

(23) Hung, R. J., and Shyu, K. L., Cryogenic Liquid Hydrogen Suction Dip and Slosh Wave Excitation During Draining in Microgravity, Advances in Cryogenic Engineering, 39, 219-229, 1994.

(24) Hung, R. J., and Lee, C. C., Effect of the Baffle on the Cryogenic Helium Container Viscous Stress and Moment Fluctuations in Microgravity, Advances in Cryogenic Engineering, 39, 251-260, 1994.

(25) Hung, R. J., Lee, C. C., and Leslie, F. W., Dynamic Characteristics of the Partially Filled Rotating Dewar of the Gravity Probe-B Spacecraft, Acta Astronautica, 32(3), 199-209, 1994.

(26) Hung, R. J., and Lee, C. C., Effect of Baffles on Gravity Gradient Driving Bubble Imbalance Perturbations in Microgravity, Canadian Aeronautics and Space Journal, 40(3), 107-124, 1994.

(27) Hung, R. J., Lee, C. C., and Leslie, F. W., Dynamics of Gravity Probe-B Spacecraft Due to Gravity Jitter Induced Cryogenic Helium Disturbances in Rotating Dewar, Advances in Space Research, 14(5), 115-122, 1994.

(28) Hung, R. J., Pan, H. L., and Leslie, F. W., Fluid System Angular Momentum and Moment Fluctuations

Driven by Gravity Gradient or Gravity Jitter in Microgravity, Journal of Flight Sciences and Space Research (Zeitschrift fur Flugwissenschaften und Weltraumforschung), 18, 195-202, 1994.

(29) Hung, R. J., and Pan, H. L., Mathematical Formulation of Gravity Gradient and Gravity Jitter Accelerations Acting on the Fluid Systems of On-Orbit Orbital Spacecraft, Proceedings of National Science Council (A), 18(3), 236-247, 1994.

(30) Hung, R. J., and Pan, H. L., Numerical Modeling of Bubble Oscillations in Microgravity, Scientific Computing and Automation, 10(6), 21-25, 1994.

(31) Hung, R. J., and Pan, H. L., Turn-Around Gravity Jitter Excited Slosh Waves and Their Effects on Angular Momentum and Viscous Stress Exerted on Spacecraft, Proceedings of National Science Council, (A), 18, 353-370, 1994.

(32) Hung, R. J., and Shyu, K. L., Liquid Hydrogen Suction Dip and Slosh Wave Excitation During Draining Under Normal and Reduced Gravity Environments, Transactions of the Japan Society for Aeronautical and Space Sciences, 36, 225-248, 1994.

(33) Hung, R. J., Pan, H. L., and Long, Y. T., Sloshing Dynamics Modulated Cryogenic Helium Fluids Driven by Gravity Gradient or Jitter Accelerations Associated with Slew Motion in Microgravity, Acta Mechanica Sinica, 10, 367-381, 1994.

(34) Hung, R. J., and Lee, C. C., Effect of a Baffle on Slosh Waves Excited by Gravity Gradient Acceleration in Microgravity, Journal of Spacecraft and Rockets, 31, 1107-1114, 1994.

(35) Hung, R. J., Pan, H. L., and Long, Y. T., Peculiar Behavior of Helium II Disturbances Due to Sloshing Dynamics Driven by Jitter Accelerations Associated With Slew Motion in Microgravity, Cryogenics, 34(8), 641-648, 1994.

(36) Hung, R. J., Long, Y. T., and Pan, H. L., Sloshing Dynamics Induced Angular Momentum Fluctuations Driven by Jitter Accelerations Associated with Slew Motion in Microgravity, Transactions of the Japan Society for Aeronautical and Space Sciences,37, 217-234,1994.

(37) Hung, R. J., and Pan, H. L., Simulation of Sloshing Dynamics Induced Forces and Torques Actuated on Dewar Container Driven by Gravity Gradient and Jitter Accelerations in Microgravity, Journal of Simulation Practice and Theory, 2, 91-120, 1994.

(38) Hung, R. J., and Pan, H. L., Sloshing Dynamics Modulated Fluid Angular Momentum and Moment Fluctuations Driven by Orbital Gravity Gradient and Jitter Accelerations in Microgravity, Applied Scientific Research Journal (International Journal of the Applications of Fluid Dynamics), 54, 51-68, 1995.

(39) Hung, R. J., and Lee, C. C., Effect of Baffle on Gravity Gradient Acceleration Excited Slosh Waves and Associated Viscous Stress Force Activated Spacecraft Dynamic Fluctuations, Aeronautical Journal (Royal Aeronautical Society of United Kingdom), in press, 1995.

(40) Hung, R. J., and Shyu, K. L., Slosh Wave and Geyser Excitations Due to Liquid Hydrogen Shut-off During Draining in Microgravity, Acta Astronautica, 35, No. 8, 509-523, 1995.

(41) Hung, R. J., and Lee, C. C., Effect of Baffles on Sloshing Modulated Fluid Force and Torque Fluctuations on the Dewar Driven by Gravity Gradient Acceleration in Microgravity, Applied Scientific Research Journal, (International Journal of the Application of Fluid Dynamics), 54, 69-94, 1995.

(42) Hung, R. J., and Pan, H. L., Fluid Force Activated Spacecraft Dynamics Driven by Gravity Gradient and Jitter Accelerations, Journal of Guidance, Control and Dynamics, 18,(No. 5), 1190-1196, 1995.

(43) Hung, R. J., and Pan, H. L., Baffle Effect on Sloshing-Modulated Torques Responsed to Orbital Accelerations in Microgravity, Journal of Spacecraft and Rockets, 32, No. 4, 723-731, 1995.

(44) Hung, R. J., and Lee, C.C., Longitudinal and Tranverse Modes of Slosh Wave Excitation in Rotating Dewar Associated with Gravity Jitters, Acta Astronautica, 32, in press, 1995.

(45) Hung, R. J., and Shyu, K.L., Liquid Resettlement and Slosh Wave Excitation During Fluid Reorientation in Microgravity. Acta Astronautica, 32, in press, 1995.

(46) Hung, R. J., and Long, Y. T., Effect of Baffle on Slosh Reaction Forces in Rotating Liquid Helium Subjected to a Lateral Impulse in Microgravity, Cryogenics, in press, 1995.

(47) Hung, R. J., and Pan, H. L, Rotational Speed and Wrapping of Different Size Cryogenic Helium Bubbles Around a Dewar Well in Microgravity, Aeronautical Journal (Royal Aeronautical Society of United Kingdom), in press, 1995.

(48) Hung, R. J., and Pan, H. L., Simulation of Bubble Spin-Up and Spin-Down in Microgravity, Scientific Computing and Automation, 12, No. 6, 19-22, 1995.

(49) Hung, R. J., and Pan, H. L., Mathematical Model of Bubble Sloshing Dynamics for Cryogenic Liquid Helium in Orbital Spacecraft Dewar Container, Applied Mathematical Modelling, 19, (August), 483-498, 1995.

(50) Hung, R. J., and Pan, H. L., Sloshing Modulated Liquid-Vapor Interface Fluctuations Activated by Orbital Accelerations Associated with Spinning and/or Slew Motions, Journal of Colloid and Interface Science, 170, 538-549, 1995.

(51) Hung, R. J., and Pan, H. L., Orbital Spacecraft Cryogenic Helium Dewar Sloshing Dynamics Driven by Gravity Gradient Acceleration Associated with Slew Motion, Japan Society of Mechanical Engineers International Journal/Fluid and Thermal Engineering, 38(3), 448-457, 1995.

(52) Hung, R. J., and Pan, H. L., Combined Gravity Gradient and Jitter Accelerations Acting on Liquid-Vapor Interface Oscillations in Reduced Gravity, International Journal of Mechanical Sciences, in press, 1995.

(53) Hung, R.J., Long, Y.T., and Pan, H.L., Actuation of Sloshing Modulated Force and Moment on Liquid Container Driven by Jitter Accelerations Associated with Slew Motion in Microgravity, Journal of Applied Mathematics and Mechanics, in press, 1995.

(54) Hung, R.J., and Pan, H.L., Sloshing Dynamics Modulated Angular Momentum Fluctuations Actuated by Gravity Gradient Acceleration Associated with Spacecraft Slew Motion, Space Technology, 6, 381-390, 1995.

(55) Hung, R.J., and Pan, H.L., Rotational Speed Spin-Down and Unwrapping of Various Size Symmetric Cryogenic Helium Bubbles Around Dewar Well in Microgravity, Transactions of the Japan Society for Aeronautical and Space Sciences, 37, in press, 1995.

(56) Hung, R.J., and Pan, H.L., Sloshing Induced Moment Driven by the Gravity Gradient Associated with Spacecraft Slew Motion, Journal of Spacecraft and Rocket, 32, in press, 1995.

(57) Hung, R.J., and Pan, H.L., Dynamical Behavior of Cryogenic Helium in a Partially Filled Dewar in Microgravity, Journal of Aerospace Engineering, in press, 1995.

(58) Hung, R.J., and Pan, H.L., Transient Flow Profiles of Spin-Up in a Filled Cylinder, Proceedings of National Science Council, 19, in press, 1995.

(59) Hung, R.J., and Lee, C.C., Effect of Baffle on Gravity Gradient Excited Slosh Waves and Spacecraft Moment and Angular Momentum Fluctuations in Microgravity, Il Nuovo Cimento, in press, 1995.

(60) Hung, R.J., and Long, Y.T., Response and Decay of Rotating Cryogenic Liquid Helium Reacted to Impulsive Accelerations in Microgravity, Transaction of Japan Society for Aeronautical and Space Sciences, 37, 291-310, 1995.

(61) Hung, R.J., and Pan, H.L., Sloshing Dynamics Governed Bubble Oscillations Driven by Gravity Gradient and Jitter Accelerations in Microgravity, Microgravity Quarterly, in press, 1995.

(62) Hung, R.J., and Long, Y.T., Mathematical Model of Variable Polarity Plasma Arc Welding Process and Fabrication of Space Station, Proceedings of National Science Council, 19, in press, 1995.

(63) Hung, R.J., and Pan, H.L., Three-Dimensional Transient Flow of Spin-Up in a Filled Cylinder with Oblique Gravity Force, Transaction of Japan Society for Aeronautical and Space Sciences, 38, No. 120, 136-150, 1995.

(64) Hung, R.J., and Long, Y.T., Cryogenic Rotating Helium in Response to Lateral and Axial Impulses in Microgravity. Advances in Cryogenic Engineering, 41, in press, 1995.

(65) Hung, R.J., Pan, H.L., and Zu, G.J., Behavior of Helium II Bubble During Spin-Up and Spin-Down Motions Wrapping Around Rotating Dewar Well. Advances in Cryogenic Engineering, 41, in press, 1995.

(66) Hung, R.J., Long, Y.T., and Zu, G.J., Sloshing of Cryogenic Helium Driven by Lateral Impulse/Gravity-Gradient-Dominated/or G-Jitter-Dominated Accelerations and Orbital Dynamics. Cryogenics, in press, 1995.

(67) Hung, R.J., and Long, Y.T., Response of Lateral Impulse on Liquid Helium Sloshing with Baffle Effect in Microgravity, International Journal of Mechanical Sciences, in press, 1995.

(68) Hung, R.J., Long, Y.T., and Zu, G.J., Coupling of Helium II Slosh Dynamics and Orbital Dynamics in Microgravity, Proceedings of National Science Council, (A), 19, in press, 1995.

(69) Hung, R.J., and Long, Y.T., Baffle Effect of Sloshing Induced Fluid Mass Center Disturbances and Slosh Reaction Force Acting on Spacecraft in Response to Impulse in Microgravity, Journal of Astronautics, 16, in press, 1995.

(70) Hung, R.J., and Pan, H.L., Modelling of Sloshing Modulated Angular Momentum Fluctuations Activated by Gravity Gradient Associated with Slew Motion, Applied Mathematical Modelling, 19, in press, 1995.

(71) Hung, R.J., and Pan, H.L., Spin-up and Wrapping of Cryogenic Helium Bubble Around Dewar Well from Rest in Microgravity, Mechanics Research and Communications, in press, 1995.

II. Basic Characteristics of Gravity Gradient and G-Jitter Accelerations

Any fluid element inside the on-orbit spacecraft fluid system is subject to the acceleration that arises from the gravity gradient of the Earth[1-3]. This acceleration can be calculated based on the non-inertial frame spacecraft bound coordinate. Thus, the coordinate system shall be transformed from ordinary inertial frame coordinate to non-inertial coordinate.

(A) Orbit Motion of Spacecraft

Let us consider the examples of Gravity Probe-B (GP-B) and Advanced X-Ray Astrophysics Facility-Spectroscopy (AXAF-S) spacecrafts, which are the Earth satellites orbiting at 650 km altitude directly over the poles, the orbit period, τ_o can be computed from following expression:

$$\tau_o = 2\pi \frac{R_c^{3/2}}{R_E g_o^{1/2}} \qquad (2\text{-}1)$$

where R_E denotes the radius of Earth (= 6373 km); R_c, the radius of the circular orbit (= R_E + h = 7023 km); h, orbit altitude (= 650 km); and g_o, Earth gravity acceleration (= 9.81 m/s^2). For the cases of both GP-B and AXAF-S spacecrafts, the orbit period τ_o = 97.6 min, and orbit rate n = $2\pi/\tau_o$ = 1.07 x 10^{-3} $^{rad}/_{s}$.

As the spacecraft is orbiting around the Earth, the azimuth angle of the Earth, ψ_E, toward the location of the spacecraft mass center varies with respect to time. At time t = 0, the rolling axis of the spacecraft is aligned with the

radial direction of the Earth's center to the spacecraft mass center. Assuming the spacecraft rolling axis is linearly turning around 0° to 360° in the orbit period, τ_o, of the spacecraft when the spacecraft is orbiting around the Earth. This is particularly true for the case of the GP-B spacecraft. Without the spacecraft slew motion, the azimuth angle (ψ_{Eo}) can be defined as

$$\psi_{E_o} = \frac{2\pi}{\tau_o} t \qquad (2\text{-}2)$$

where τ_o is the spacecraft orbit period [defined in Equation (2-1)]; and t is the time measured from the instant when the direction of the spacecraft rolling axis is aligned with the radial direction of the spacecraft mass center to the center of the Earth.

(B) Slew Motion of Spacecraft

For the purpose to carry out wide-range observations, some scientific spacecraft requires slew motion with respect to the mass center of the spacecraft. This is particularly true for the case of the AXAF-S spacecraft. For the case of the spacecraft slew motion, azimuth angle, shown in Equation (2-2), shall be modified through the coordinate transformation of slew motion when the spacecraft is orbiting around the Earth.

Let us assume that the slew motion starts with the center located at the mass center of the spacecraft. Let us choose cartesian coordinate (x", y", z") with z"-axis along the axis of the dewar container (see Figure 1). At time t = 0, the radial vector $\hat{r}_c$ from the spacecraft mass center to the center of the Earth lies on the x"-z" plane of the cartesian coordinate chosen (see Figure 1). The azimuth angle ψ_E is defined as the angle between the radial vector $\hat{r}_c$ and the z"-axis. Rotation matrices for spinning and/or slew motions along the x"-, y"- and z"-axes can be expressed as

$$\begin{bmatrix} 1 & 0 & 0 \\ 0 & \cos\omega_x t & \sin\omega_x t \\ 0 & -\sin\omega_x t & \cos\omega_x t \end{bmatrix}, \begin{bmatrix} \cos\omega_y t & 0 & -\sin\omega_y t \\ 0 & 1 & 0 \\ \sin\omega_y t & 0 & \cos\omega_y t \end{bmatrix}, \begin{bmatrix} \cos\omega_z t & \sin\omega_z t & 0 \\ -\sin\omega_z t & \cos\omega_z t & 0 \\ 0 & 0 & 1 \end{bmatrix}$$

respectively. Here, ω_x, ω_y and ω_z denote angular velocity of slew and/or spinning motions along the x'-, y'- and z'-axes, respectively. Radial vector $\hat{r}_c$ in cartesian coordinate without slew and spinning motion is (see Figure 1)

$$\hat{r}_{co} = [\sin\psi_{Eo}, 0, -\cos\psi_{Eo}] \tag{2-3}$$

For the successive operations of the spacecraft from spinning motion along the z"-axis, then slew motion along the y"-axis, and then slew motion along the x"-axis, radial vector $\hat{r}_c$ results

$$\hat{r}_{c\text{-}z,y,x} = \begin{bmatrix} 1 & 0 & 1 \\ 0 & \cos\omega_x t & \sin\omega_x t \\ 0 & -\sin\omega_x t & \cos\omega_x t \end{bmatrix} \begin{bmatrix} \cos\omega_y t & 0 & -\sin\omega_y t \\ 0 & 1 & 0 \\ \sin\omega_y t & 0 & \cos\omega_y t \end{bmatrix} \cdot$$

$$\begin{bmatrix} \cos\omega_z t & \sin\omega_z t & 0 \\ -\sin\omega_z t & \cos\omega_z & 0 \\ 0 & 0 & 1 \end{bmatrix} \begin{bmatrix} \sin\psi_{Eo} \\ 0 \\ -\cos\psi_{Eo} \end{bmatrix} \tag{2-4}$$

In addition to the modification of the azimuth angle made by the spacecraft slew motion through the formulation of coordinate transformation, shown in Equations (2-3) and (2-4), accelerations are also induced to activate on the fluid mass in the dewar container. Accelerations acting on the fluid particle in the dewar induced by the slew motion of the spacecraft with the coordinate fixed at the spacecraft mass center mass is as follows (see Figure 1):

$$\ddot{\vec{R}}_p = \vec{\omega} x (\vec{\omega} x \vec{R}_p) + \vec{\alpha} x \vec{R}_p + 2\vec{\omega} x \vec{v} \tag{2-5}$$

where $\vec{R}_p$ denotes the position vector of the fluid particle in the dewar container relative to the body frame of the spacecraft; $\vec{\omega}$, angular velocity of the

spacecraft body frame; $\vec{\alpha}$, angular acceleration of the spacecraft body frame; and $\vec{v}$, velocity of the fluid particle relative to the spacecraft body frame.

As we indicated earlier, let us assume that the slew motion starts with the center located at the spacecraft mass center, cartesian coordinate (x'', y'', z'') is chosen with origin located at the spacecraft mass center. Let us also assume that x''-z'' plane intersects the center of Earth and the spacecraft mass center. In other words, azimuth angle of Earth toward the spacecraft mass center lies in the x''-z'' plane. Slew motion is along both the x''- and y''-coordinates. Thus, $\vec{\omega}_s = (\omega_{sx}, \omega_{sy}, 0)$ and $\vec{\alpha}_s = (\alpha_{sx}, \alpha_{xy}, 0)$, $\vec{R}_p$ due to slew motion becomes

$$\ddot{\vec{R}}_{p,slew} = \begin{bmatrix} \ddot{\vec{R}}_{x''} \\ \ddot{\vec{R}}_{y''} \\ \ddot{\vec{R}}_{z''} \end{bmatrix}_{slew} = \begin{bmatrix} \omega_{sy}(\omega_{sx}R_y - R_x\omega_{sy}) + \alpha_{sy}R_z + 2\omega_{sy}V_z \\ -\omega_{sx}(\omega_{sx}R_y - R_x\omega_{sy}) - \alpha_{sx}R_z - 2\omega_{sx}V_z \\ -R_z(\omega_{sx}^2 + \omega_{sz}^2) + (\alpha_{sx}R_y - \alpha_{sy}R_x) + 2(\omega_{sx}V_y - \omega_{sy}V_x) \end{bmatrix}_{slew} \qquad (2\text{-}6)$$

(C) Coupling for the Accelerations of Spinning and Slew Motion of Spacecraft

As indicated in this review, with their specified functions of scientific observation, the dewar container of the GP-B is spinning with a certain rotating rate without slew motion during the normal operation while AXAF-S requires slew motion for pointing control to observe point and extended sources of astronomical objects without spinning. For some particular reasons required in other spacecraft, it might be faced with the situation that both spinning and slew motions are needed simultaneously. To encounter this case, the following formulations are made to deal with coupling for the accelerations of spinning and slew motion of the spacecraft:

$$\ddot{\vec{R}}_{p,\ slew\ and\ spinning} = \begin{bmatrix} \ddot{\vec{R}}_x \\ \ddot{\vec{R}}_y \\ \ddot{\vec{R}}_z \end{bmatrix}_{slew\ and\ spinning}$$

$$= \begin{bmatrix} \omega_{sy}(\omega_{sx}R_y - \omega_{sy}R_x) + \alpha_{sy}R_z + 2\omega_{sy}V_z \\ -\omega_{sx}(\omega_{sx}R_y - \omega_{sy}R_x) - \alpha_{sx}R_z - 2\omega_{sx}V_z \\ -R_z(\omega_x^2 + \omega_{sy}^2) + (\alpha_{sx}R_y - \alpha_{sy}R_x) + 2(\omega_{sx}V_y - \omega_{sy}V_x) \end{bmatrix}_{slew}$$

$$+ \begin{bmatrix} -(\omega_z R_x - \omega_{sx}R_z)\omega_z - \dot{\omega}_z R_y - 2\omega_z V_y \\ (\omega_{sy}R_z - \omega_z R_y)\omega_z + \dot{\omega}_z R_x + 2\omega_z V_x \\ (\omega_{sy}R_x + \omega_{sy}R_y)\omega_z \end{bmatrix}_{spinning\ and\ coupling} \qquad (2\text{-}7)$$

where ω_z and $\dot{\omega}_z$ denote angular velocity and angular acceleration, respectively, of spacecraft spinning motion along the z-axis.

For the case of the GP-B spacecraft, there is no slew motion and the spinning is the only acceleration acting on the spacecraft fluid system. Acceleration due to spacecraft spinning motion becomes

$$\ddot{\vec{R}}_{p,\,spinning} = \begin{bmatrix} \ddot{R}_x \\ \ddot{R}_y \\ \ddot{R}_z \end{bmatrix} = \begin{bmatrix} -R_x\omega_z^2 - R_y\dot{\omega}_z - 2\omega_z V_y \\ -R_y\omega_z^2 + R_x\dot{\omega}_z + 2\omega_z V_x \\ 0 \end{bmatrix}_{spinning} \qquad (2\text{-}8)$$

To convert the expression of Equation (2-8) in cartesian coordinate to cylindrical coordinate, by using the relationships of $(R_x, R_y) = (r\cos\theta, r\sin\theta)$ and $(v_x, v_y) = (u_r\cos\theta - u_\theta\sin\theta, u_r\sin\theta + u_\theta\cos\theta)$, Equation (2-8) becomes

$$\ddot{\vec{R}}_{p,\,spinning} = \begin{bmatrix} \ddot{R}_x \\ \ddot{R}_y \\ \ddot{R}_z \end{bmatrix} = \begin{bmatrix} -r\cos\theta\omega_z^2 - r\sin\theta\dot{\omega}_z - 2(u_r\sin\theta + u_\theta\cos\theta)\omega_z \\ -r\sin\theta\omega_z^2 + r\cos\theta\dot{\omega}_z + 2(u_r\cos\theta - u_\theta\sin\theta)\omega_z \\ 0 \end{bmatrix}_{spinning} \qquad (2\text{-}9)$$

and

$$\ddot{\vec{R}}_{p,\,spinning} = \begin{bmatrix} \ddot{R}_r \\ \ddot{R}_\theta \\ \ddot{R}_z \end{bmatrix} = \begin{bmatrix} \ddot{R}_x\cos\theta + \ddot{R}_y\sin\theta \\ -\ddot{R}_x\sin\theta + \ddot{R}_y\cos\theta \\ \ddot{R}_z \end{bmatrix}_{spinning} = \begin{bmatrix} -r\omega_z^2 - 2u_\theta\omega_z \\ r\dot{\omega}_z + 2u_r\omega_z \\ 0 \end{bmatrix}_{spinning} \qquad (2\text{-}10)$$

Accelerations induced by spacecraft spinning motion alone becomes

$$\begin{bmatrix} a_r \\ a_\theta \\ a_z \end{bmatrix}_{spinning} = -\begin{bmatrix} \vec{R}_r \\ \vec{R}_\theta \\ \vec{R}_z \end{bmatrix}_{spinning} = \begin{bmatrix} r\omega_z^2+2u_\theta\omega_z \\ =r\dot{\omega}_z-2u_r\omega_z \\ 0 \end{bmatrix}_{spinning} \qquad (2\text{-}11)$$

(D) Gravity Gradient Acceleration

The gravity gradient acceleration acting on the fluid mass of spacecraft can be shown as

$$\hat{a}_{gg}=-n^2\,[3\,(\hat{f}_c\cdot\hat{d})\,\hat{f}_c-\hat{d}] \qquad (2\text{-}12)$$

where $\hat{a}_{gg}$ denotes gravity gradient acceleration vector; $\hat{d}$, the vector (not a unit vector) from the fluid element to the spacecraft mass center; $\hat{f}_c$, a unit vector from the spacecraft mass center to the center of the Earth; and n, the orbit rate (see Figure 1).

It is assumed that the gravity gradient exerted on the mass center of the spacecraft orbiting around the Earth on its specified orbit is zero. In other words, all the gravity acceleration exerted on the spacecraft is nothing but the gravity gradient acceleration which is defined in Equation (2-12). In this study, we are interested in investigating how gravity gradient acceleration affects the dynamical behavior of cryogenic fluid elements of helium.

For the convenience of mathematical study, let us describe all the parameters involved in Equation (2-12) in terms of cartesian coordinates. In order to match with the computer simulation, mathematical derivation are considered in the first quadrant. Figure 1 illustrates the geometrical relationship of the parameters shown in Equation (2-12).

Let us consider the fluid element of interests, m, located at (r, θ, z) in cylindrical coordinates and at (x, y, z) in cartesian coordinates. The origin of the two coordinate systems is located at the center bottom of the dewar tank. The slew and/or spinning motions, mentioned earlier, are executed at the spacecraft mass center with cartesian coordinate (x", y", z"). The spacecraft

mass center is located at $z = L_c$. Assume that vector $\hat{r}_c$ lies in the x-z plane of the cartesian coordinate. Vector $\hat{d}$ in (x, y, z) coordinate becomes

$$\hat{d} = [-r\cos\theta, -r\sin\theta, -(z-L_c)] \tag{2-13}$$

Substituting Equations (2-4) and (2-13) in (2-12), non-inertial frame expression of gravity gradient acceleration with spinning motion in z-axis becomes

$$\begin{bmatrix} a_{gg,x} \\ a_{gg,y} \\ a_{gg,z} \end{bmatrix}_{spinning\ in\ z\text{-}axis} = -n^2 \begin{bmatrix} 3[-r\sin\psi_{Eo}\cos(\theta+\omega_z t)+(z-L_c)\cos\psi_{Eo}]\sin\psi_{Eo}\cos\omega_z t + r\cos\theta \\ -3[r\sin\psi_{Eo}\cos(\theta+\omega_z t)+(z-L_c)\cos\psi_{Eo}]\sin\psi_{Eo}\sin\omega_z t + r\sin\theta \\ -3[-r\sin\psi_{Eo}\cos(\theta+\omega_z t)+(z-L_c)\cos\psi_{Eo}]\cos\psi_{Eo} + (z-L_c) \end{bmatrix} \tag{2-14}$$

Similarly, non-inertial frame expressions of gravity gradient acceleration with slew motion in y-axis becomes

$$\begin{bmatrix} a_{gg,x} \\ a_{gg,y} \\ a_{gg,z} \end{bmatrix}_{slew\ in\ y\text{-}axis} = -n^2 \begin{bmatrix} 3[-r\sin\psi\cos\theta(z-L_c)]\sin\psi + r\cos\theta \\ r\sin\theta \\ -3[-r\sin\psi\cos\theta+\cos\psi(z-L_c)]\cos\psi + (z-L_c) \end{bmatrix} \tag{2-15}$$

where $\psi_E = \psi_{Eo} + \omega_y t$.

Also, non-inertial frame expressions of gravity gradient acceleration with slew motion in x-axis becomes

$$\begin{bmatrix} a_{gg,x} \\ a_{gg,y} \\ a_{gg,z} \end{bmatrix}_{slew\ in\ x\text{-}axis} = -n^2 \begin{bmatrix} 3A\sin\psi_{Eo} + r\cos\theta \\ 3A\cos\psi_{Eo}\sin\omega_x t + r\sin\theta \\ 3A\cos\psi_{Eo}\cos\omega_x t + (z-L_c) \end{bmatrix} \tag{2-16}$$

$$A = -r\cos\theta\sin\psi_{Eo} + \cos\psi_{Eo}[r\sin\omega_x t\sin\theta + \cos\omega_x t(z-L_c)]$$

The gravity gradient acceleration located at (r, θ, z) can be computed from that located at (x, y, z), from the following relation:

$$\hat{a}_{gg} = \begin{bmatrix} \hat{a}_{gg,r} \\ \hat{a}_{gg,\theta} \\ \hat{a}_{gg,z} \end{bmatrix} = \begin{bmatrix} \cos\theta & \sin\theta & 0 \\ -\sin\theta & \cos\theta & 0 \\ 0 & 0 & 1 \end{bmatrix} \begin{bmatrix} a_{gg,x} \\ a_{gg,y} \\ a_{gg,z} \end{bmatrix} \tag{2-17}$$

(E) G-Jitter Accelerations

In addition to gravity gradient acceleration acting on the fluid element

of on-orbit spacecraft fluid systems, there is another acceleration of g-jitter also exerted forces on the fluid systems.

Among varieties of g-jitter accelerations listed, accelerations induced by slew motion of the spacecraft dominate the forces activated on the spacecraft fluid systems. In the derivation of acceleration induced by the slew motion of the spacecraft, the coordinate system (x", y", z") is fixed at the spacecraft mass center. A detailed expression of $[\ddot{R}_x, \ddot{R}_y, \ddot{R}_z]_{slew}$ are shown in Equation (2-6) of this review. G-jitter acceleration is a summation of acceleration induced by slew motion and others, such as atmospheric drag on the spacecraft, spacecraft attitude motions arising from machinery vibration, thruster firing, crew motion, etc. Thus, g-jitter acceleration can be expressed as

$$\hat{a}_{gj} = \begin{bmatrix} a_{gj,r} \\ a_{gj,\theta} \\ a_{gj,z} \end{bmatrix}_{slew} = -\begin{bmatrix} F_r \\ F_\theta \\ F_z \end{bmatrix}_{slew} - \begin{bmatrix} F_r \\ F_\theta \\ F_z \end{bmatrix}_{others} [1+\frac{1}{2}\sin(2\pi ft)]$$

$$= -\begin{bmatrix} \cos\theta & \sin\theta & 0 \\ -\sin\theta & \cos\theta & 0 \\ 0 & 0 & 1 \end{bmatrix} \begin{bmatrix} F_x \\ F_y \\ F_z \end{bmatrix}_{slew} - \begin{bmatrix} F_r \\ F_\theta \\ F_z \end{bmatrix}_{others} [1+\frac{1}{2}\sin(2\pi ft)] \qquad (2\text{-}18)$$

where f is the jitter frequency (Hz) imposed on the fluid systems of the spacecraft. The amplitude of the g-jitter fluctuating component, assumed to be one-half the mean value, is based upon Russian experience in Mir experiments[4].

III. Non-Inertial Frame Mathematical Formulation of Fundamental Equations

Dynamical Behavior of fluid elements inside the on-orbit spacecraft fluid systems are strongly modified by the gravity gradient and g-jitter accelerations. In order to accommodate the effect of gravity gradient acceleration on the on-orbit fluid motion, one has to consider non-inertial frame spacecraft bound coordinate rather that adopting inertial frame coordinate used in ordinary fluid mechanics formulation.

Experiment made by Andronikashvili[23,24] for rotating helium II shows that

it is necessary to exceed a critical velocity for the interaction between the normal and superfluid components to establish entire bucket in rotation[25]. Based on this illustration shown earlier, the problem under consideration with normal and superfluid helium, which can produce great enough vortex line tangles to assure an interaction between the normal and superfluid components, suggests an adoption of Newtonian fluids in terms of corresponding temperature with proper concentration ratio of normal and superfluid helium in this review[30,31].

Consider a closed circular cylindrical dewar of radius, a, with height, L, which is partially filled with cryogenic liquid helium, and the ullage is filled with a helium vapor. Angular velocity of rotating cylinder is ω. Density and viscosity of liquid helium and helium vapor are ρ_L, μ_L, ρ_v, and μ_v, respectively. Let us use cylindrical coordinates (r, θ, z), with corresponding velocity components (u, v, w), and corresponding residual gravity acceleration, such as gravity gradient components ($a_{gg,r}$, $a_{gg,\theta}$, $a_{gg,z}$) and g-jitter components ($a_{gj,r}$, $a_{gj,\theta}$, $a_{gj,z}$). In the derivation of the governing equations, accelerations induced by the spinning motion of the spacecraft is included in the formulation. The rest of the acceleration such as slew motion, atmospheric drag on the spacecraft, spacecraft attitude motions arising from machinery vibrations, thruster firing, and others, are included in the jitter acceleration, shown in Equation (2-18). The governing equations for non-inertial frame of spacecraft bound coordinates can be shown as follows:

(A) Continuity Equation

$$\frac{1}{r}\frac{\partial}{\partial r}(ru)+\frac{1}{r}\frac{\partial v}{\partial \theta}+\frac{\partial w}{\partial z}=0 \qquad (3-1)$$

(B) Momentum Equations

$$\rho\left(\frac{\partial u}{\partial t}+u\frac{\partial u}{\partial r}+\frac{v}{r}\frac{\partial u}{\partial \theta}-\frac{v^2}{r}+w\frac{\partial u}{\partial z}\right)=-\frac{\partial p}{\partial r}+2\rho\omega_z v+\rho\left(a_{gj,r}+a_{gg,r}\right)+\rho r\omega_z^2$$

$$+\mu\left(\nabla^2 u-\frac{u}{r^2}-\frac{2}{r^2}\frac{\partial v}{\partial\theta}\right) \tag{3-2}$$

$$\rho\left(\frac{\partial v}{\partial t}+u\frac{\partial v}{\partial r}+\frac{v}{r}\frac{\partial v}{\partial\theta}+\frac{uv}{r}+w\frac{\partial v}{\partial z}\right)=-\frac{1}{r}\frac{\partial p}{\partial\theta}-2\rho\omega_z u+\rho\left(a_{gj,\theta}+a_{gg,\theta}\right)-r\dot{\omega}_z$$

$$+\mu\left(\nabla^2 v-\frac{v}{r^2}+\frac{2}{r^2}\frac{\partial u}{\partial\theta}\right) \tag{3-3}$$

$$\rho\left(\frac{\partial w}{\partial t}+u\frac{\partial w}{\partial r}+\frac{v}{r}\frac{\partial w}{\partial\theta}+w\frac{\partial w}{\partial z}\right)=-\frac{\partial p}{\partial z}+\rho\left(a_{gj,z}+a_{gg,z}\right)+\mu\nabla^2 w \tag{3-4}$$

where

$$\nabla^2=\frac{1}{r}\frac{\partial}{\partial r}\left(r\frac{\partial}{\partial r}\right)+\frac{1}{r^2}\frac{\partial^2}{\partial\theta^2}+\frac{\partial^2}{\partial z^2} \tag{3-5}$$

In these formulations, $2\omega_z v$ and $2\omega_z u$ are the Coriolis acceleration, $r\omega_z^2$ is the centrifugal acceleration, and $r\dot{\omega}_z$ is the angular acceleration induced by the spinning motion of the spacecraft.

IV. Initial and Boundary Conditions of Spacecraft Fluid System in Microgravity Environment

Governing equations of the fluid motion in on-orbit spacecraft fluid systems for non-inertial frame spacecraft bound coordinates have been illustrated in Equations (3-1) to (3-5). These equations shall be combined with the characteristics of gravity gradient and g-jitter accelerations as that formulated in Equations (2-1) to (2-18). Initial and boundary conditions shall be introduced to accommodate solving fluid motion in on-orbit spacecraft fluid system for non-inertial frame coordinate[7-9,32-34].

There are several ways to compute the dynamical behavior of liquid-vapor interface. One way is explicitly tracking the dynamics of interface fluctuations through the computation of the radius of curvature variations along the interface[35]. The other method is to implicitly capture the interface using a level set approach, and the interface will be identified as the zero level set

of a smooth function[36]. In this review, the method of explicitly tracking the interface fluctuations is described[35].

Let the profile of the interface between gaseous and liquid fluids be given by:

$$\eta(t, r, \theta, z) = 0 \qquad (4\text{-}1)$$

The initial condition of the profile of the interface between gaseous and liquid fluids at $t = t_o$ is assigned explicitly, and is given by:

$$\eta(t = t_o, r, \theta, z) = 0 \qquad (4\text{-}2)$$

A set of boundary conditions has to be supplied for solving the equations. These initial interface profiles used in this study have been given explicitly through the steady state computations made by Hung and Leslie[20] and Hung et al[7-9] which were checked by the experiments carried out by Leslie[21]. These boundary conditions are as follows:

(1) Along the container wall, the following three boundary conditions apply:

(a) Interface between solid and liquid fluid: No-penetration and no-slip conditions assure that both the tangential and the normal components of the liquid velocity along the solid walls will vanish.

(b) Interface between solid and gaseous (vapor) fluid: Similar no-penetration and no-slip conditions as that shown for interface between solid and liquid fluid will apply.

(c) At the location of solid-liquid-gaseous (vapor) three phases interface: No-penetration, but not no-slip condition apply. This will assure that normal components of liquid and vapor velocities along the solid walls will vanish, and allow a slipping flow of liquid and vapor fluids along the solid wall at three phase interface location. The velocity of slipping flow at this location is governed by the adhesive forces between fluids (liquid and gaseous) and solid

walls. Also, at this location of three phase interface, a constant contact angle is present in which the behaviors of wet or dry contacts are determined by Coulomb interaction between the fluids (liquid and vapor) and the surface phenomena (material and roughness) of solid walls[35-39].

(2) Along the interface between the liquid and gaseous fluids, the following two conditions apply:

(a) Kinematic surface boundary condition: The liquid (or gaseous) surface moves with the liquid (or gas) which implies

$$\frac{D\eta}{Dt}=0, or$$

$$\frac{\partial\eta}{\partial t}+u\frac{\partial\eta}{\partial r}+\frac{v}{r}\frac{\partial\eta}{\partial\theta}+w\frac{\partial\eta}{\partial z}=0 \ on \ \eta(t=t_a, r, \theta, z) \qquad (4-3)$$

(b) Interface stress condition: Across the liquid–vapor interface, the stress must be continuous. Based on Landau and Lifshitz[40], the stress across the liquid–vapor interface can be expressed as

$$(P_G-P_L)n_i-[(\tau_{ij})_G-(\tau_{ij})_L]n_j=\sigma(\frac{1}{R_1}+\frac{1}{R_2})n_i \qquad (4-4)$$

where R_1 and R_2 are the radii of curvatures of two major axes at the point of interests on the surface of the liquid vapor interface.

The expressions of radii of curvatures R_1 and R_2 in cylindrical coordinates from differential geometry can be shown as[40-42]

$$\frac{1}{R_1}+\frac{1}{R_2}=-\frac{1}{r}[\frac{\partial}{\partial r}(r\frac{H_r}{D})+\frac{\partial}{\partial\theta}(\frac{H_\theta}{rD})] \qquad (4-5)$$

where

$$[H_r, H_\theta]=[\frac{\partial}{\partial r}, \frac{\partial}{\partial\theta}]H, \ and \ D=(1+H_r^2+\frac{1}{r^2}H_\theta^2)^{\frac{1}{2}}$$

and the configuration of the liquid-vapor interface is $z = H(t, r, \theta)$. Here, in Equations (4-4) and (4-5)

$$\tau_{ij} = \mu\left(\frac{\partial u_i}{\partial x_j} + \frac{\partial u_j}{\partial x_i} + \frac{2}{3}\frac{\partial u_k}{\partial x_k}\delta_{ij}\right) + \xi\frac{\partial u_k}{\partial x_k}\delta_{ij}$$

is the viscous stress tensor; μ, the viscous coefficient of the first kind; ξ, the viscous coefficient of the second kind; P, the pressure; σ, the surface tension of the liquid-vapor interface; and n_j, the unit vector normal to the interface; and δ_{ij}, the Kronecker delta function. Also, subscripts G and L denote the conditions at gaseous and liquid fluids, respectively, across the liquid-vapor interface.

The fluid stresses across the liquid-vapor interface can be decomposed to the components normal (n_i, a unit vector) and tangential (t_i, a unit vector) to the interface. For the component tangential to the interface, one can take a dot product of a unit vector tangential to the interface, t_i, to Equations (4-4) and (4-5), which leads to

$$[(\tau_{ij}t_i n_j)]_L = [\tau_{ij}t_i n_j)]_G \qquad (4\text{-}6)$$

since $n_i t_i = 0$.

For the component normal to the interface, one can also take a dot product of a unit vector normal to the interface, n_i, to equations (4-4) and (4-5), which leads to

$$P_G - P_L - [(\tau_{ij}n_i n_j)_G - (\tau_{ij}n_i n_j)_L] = -\frac{\sigma}{r}\left[\frac{\partial}{\partial r}\frac{rH_r}{D}\right) + \frac{\partial}{\partial\theta}\left(\frac{H_\theta}{rD}\right)] \qquad (4\text{-}7)$$

For components normal to the interface along the (r, θ, z) directions in cylindrical coordinates can be obtained by taking dot products of n_r, n_θ, n_z separately to Equations (4-4) and (4-5), which are expressed as

$$(P_G - P_L)\begin{bmatrix} n_r \\ n_\theta \\ n_z \end{bmatrix} - \begin{bmatrix} (\tau_{rh}n_j)_G - (\tau_{rj}n_j)_L \\ (\tau_{\theta j}n_j)_G - (\tau_{\theta j}n_j)_L \\ (\tau_{zj}n_j)_G - (\tau_{zj}n_j)_L \end{bmatrix}$$

$$= -\frac{\sigma}{r}\left[\frac{\partial}{\partial r}\left(\frac{rH_r}{D}\right) + \frac{\partial}{\partial \theta}\left(\frac{H_\theta}{rD}\right)\right]\begin{bmatrix} n_r \\ n_\theta \\ n_z \end{bmatrix} \qquad (4\text{-}8)$$

where (n_r, n_θ, n_z) is the unit vector normal to the interface in cylindrical coordinates (r, θ, z).

For the purpose of solving bubble dynamic problems in microgravity, one must solve the governing equations shown in Equations (3-1) to (3-5), accompanied by a set of initial and boundary conditions, shown in Equations (4-1) to (4-8). The computational algorithm applicable to cryogenic fluid management under microgravity is also given earlier[32-37]. Summarized computational algorithm are illustrated in Figure 2. Most of the illustrations shown in this review adopt a full scale GP-B spacecraft dewar tank with an inner radius of 12 cm and an outer radius of 68 cm and a height of 145 cm. The dewar tank is partially filled with cryogenic helium and the rest of the ullage is filled with helium vapor. The temperature of cryogenic helium is 1.8 K. In this review the following data were used: liquid helium density = 0.146 g/cm^3, helium vapor density = 0.00147 g/cm^3, fluid pressure = 1.66 x 10^4 dyne/cm^2, surface tension coefficient at the interface between liquid helium and helium vapor = 0.353 dyne/cm, liquid helium viscosity coefficient = 9.61 x 10^{-5} cm^2/s, and contact angle = 0°.

A staggered grid for the velocity components is used in this computer program. MAC (marker-and-cell) method[41] of studying fluid flows along a free surface is adopted. VOF (volume of fluid) method is used to track interface by solving finite difference equations numerically. Figure 2 describes computational algorithm and numerical method to track liquid-vapor interface profiles numerically. The approximate flow velocity is calculated from the explicit approximation of momentum equations based on the results from the previous time

step. Computation of pressure and velocity at the new time step are, thus, obtained from iteratively solving the pressure equation through conjugate residual technique[41-44]. The configuration of liquid-vapor interface adjusted by the surface tension effect at the new time step are then finally obtained. The time step during this computation is automatically adjusted through the fulfillment of the stability criteria of computed grid size. Convergence criterion of the iteration of pressure equation is based on the computed velocity at each cell which satisfy continuity equation with the errors no more than 10^{-5} of the velocity difference[45,46]. As for the volume conservation of liquid, a deviation of less than 1 % error of volume is always guaranteed before a move to the next time step.

V. Mathematical Formulations of Slosh Reaction Forces and Torques Due to Bubble Deformations

Sloshing dynamics of fluid system will introduce bubble deformations and oscillations which can be characterized by the types of externally applied forces in the microgravity environment. These disturbed bubble through the deformations and oscillations also produce slosh reaction feedback forces and torques acting back on the fluid filled container. Computation of slosh reaction forces and torques due to bubble deformation is essential for the development of spacecraft orbital, attitude and guidance control techniques. Mathematical formulation is derived to proceed the computation of slosh reaction forces and torque fluctuations due to bubble deformation[47-50].

For the purpose of considering large amplitude slosh wave activated slosh reaction forces exerted on the solid walls of the dewar, the fluid stresses are decomposed into the tangential and normal components acting on the walls which can be expressed as follows:

$$\Pi_t = \mu\left(\frac{\partial u_\alpha}{\partial x_\beta} + \frac{\partial u_\beta}{\partial x_\alpha}\right)\hat{t}_\alpha \hat{n}_\beta \qquad (5\text{-}1)$$

$$\Pi_n = P\delta_{\alpha\beta} - \mu\left(\frac{\partial u_\alpha}{\partial x_\beta} + \frac{\partial u_\beta}{\partial x_\alpha}\right)\hat{n}_\alpha \hat{n}_\beta \qquad (5\text{-}2)$$

where Π_t denotes the tangential component of fluid stresses; Π_n, the normal component of fluid stresses; P, the thermodynamic pressure; u_α, fluid velocity in α direction; $\hat{t}_\alpha$, unit vector tangential to the wall; $\hat{n}_\beta$, unit vector normal to the wall; μ, the molecular viscosity coefficient of fluid; and $\delta_{\alpha\beta}$, the Kronecker delta function. Subscripts α and β imply the directions of flow fields.

The stress distribution shown in Equations (5-1) and (5-2) can be integrated with respect to area and obtain the tangential and normal forces acting on the container wall. Detailed mathematical derivations of slosh reaction forces acting on the walls have been fully illustrated[32,35,46,53-56], and will not be repeated in this review.

In order to accommodate the spacecraft dynamics of pitching, yawing and rolling, cylindrical coordinates of the rotating container is transformed into cartesian coordinates based on $(x,y,z) = (r\cos\theta, r\sin\theta, z)$ with corresponding velocity components $(v_x, v_y, v_z) = (u\cos\theta - v\sin\theta, u\sin\theta + v\cos\theta, w)$. For the case of the GP-B spacecraft, the axis of rotating is always fixed at the point of proof mass which is located at the geometrical center of the dewar at $(x_c, y_c, z_c) = (0, 0, L_c)$, where $L_c = 1/2$ L and L is the height of the dewar. For the case of the AXAF-S spacecraft which is located at $(x_c, y_c, z_c) = (0, 0, L_c)$ where L_c is the height of the axis of slew motion (see Figure 1).

In addition to the slosh reaction forces (F_x, F_y, F_z) along (x, y, z) coordinates, slosh reaction torques (M_x, M_y, M_z) acting on the dewar container also have been derived mathematically[32,35,46,53-56], and will not be repeated in

this review. Relationships of slosh reaction forces (F_x, F_y, F_z), slosh reaction torques (M_x, M_y, M_z) and slosh reaction moment arms (L_x, L_y, L_z) are as follows:

$$\begin{bmatrix} M_x \\ M_y \\ M_z \end{bmatrix} = \begin{bmatrix} L_y F_z - (L_z - L_c) F_y \\ (L_z - L_c) F_x - L_x F_z \\ L_x F_y - L_y F_x \end{bmatrix} \qquad (5\text{-}3)$$

By using the relation of $F_\alpha L_\alpha = 0$, or $F_x L_x + F_y L_y + F_z (L_z - L_c) = 0$, moment arms of slosh reaction torques induced by the slosh wave excitation can be computed from the following relations:

$$\begin{bmatrix} L_x \\ L_y \\ L_z - L_c \end{bmatrix} = \frac{1}{F_x^2 + F_y^2 + F_z^2} \begin{bmatrix} F_y M_z - F_z M_y \\ F_z M_x - F_x M_z \\ F_x M_y - F_y M_x \end{bmatrix} \qquad (5\text{-}4)$$

The problems illustrated can be applied to bubble deformations activated by various forms of accelerations. Following examples are given to illustrate the bubble deformations driven by (a) centrifugal forces - bubble spin-up and spin-down motions, (b) lateral and axial impulses, (c) slew motion accompanied accelerations, and (d) combined gravity gradient and g-jitter accelerations. In these applications, first of all the time sequence animation of bubble deformations, driven by the various forms of accelerations mentioned earlier, will be illustrated based on the interests of the fluid dynamics point of view. Bubble mass center fluctuations together with slosh reaction forces and torques induced due to bubble deformations will also be described based on the timely interests from spacecraft orbital, attitude, and guidance control technology development points of view.

VI. Bubble Spin-Up From Rest With and Without a Completion of Wrapping

Bubble is initially sitting at the location between outer and inner dewar wells without rotation. During the process of bubble deformation from spherical-shape to the final shape of bubble wrapping around the inner well of the rotating dewar, the critical point is that the rotating speed of the dewar shall be great enough to create a sufficiently large centrifugal force to overcome surface

tension of bubble such that the bubble can stretch, elongate, and finally wrap around the dewar well. Dimensionless parameters characterized by the Weber number (We) is[37,50,51]

$$We = \frac{\rho\omega^2 r^3}{\sigma} = \frac{centrifugal\ force}{surface\ tension\ force}$$

Here, ρ, ω, r, and σ denote fluid density, angular velocity, radius of the container, and surface tension of bubble at the interface between liquid and vapor helium. In other words, We number also characterizes the bubble wrapping around the dewar inner well during the spin-up motion. A greater value of We number is in favor of a complete wrapping of the bubble around the dewar inner well[52].

To show an example of bubble spin-up with a complete wrapping for 95% liquid-fill level, the dewar container is spinning up from ω = 0 to 0.4 rpm linearly in 2 s and keeps constant angular velocity thereafter. Figure 3(A) shows the time sequence evolution of the three dimensional dynamical behavior of bubble evolution through the processes of elongation, wrapping around the inner well of the dewar, and finally a completion of the bubble wrapping around the inner well during the spin-up rotating of dewar. It shows that the bubble gradually deforms from spherical shape to doughnut shape which wraps around the inner column of the dewar, and becomes quasi-symmetric profile at time t = 8700 s and thereafter.

For the purpose to check the results of numerical simulation, dimensionless time scale of $E_k^{-1/2}$ is used to estimate time required for the development of viscous boundary layer[53]. Parameter E_k is Ekman number which is defined by[53]

$$E_k = \frac{\nu}{\omega(\Delta R)^2} \qquad (6\text{-}1)$$

Here ν stands for kinematic viscosity, and $\Delta R = (r_o - r_i)/2$ where r_o and r_i denote

outer and inner radii, respectively, of the dewar. In reality, Ekman number is nothing but the reverse of Reynolds number for rotating system (R_e^{-1}). Estimated time required for the fluid to attain the angular velocity of new steady state is on the order of $E_k^{-1/2}/\omega$ during spin-up motion[53]. To show examples, estimated time required for cryogenic helium to reach steady state rotating speed of 0.4 rpm spin-up from rest is on the order of 10^4 s while that of the rotating speed of 0.2 rpm spin-up from rest is on the order of 1.4 X 10^4 s. This order of magnitude estimation of time required to attain steady state is agreeable with the numerical simulation shown in this review.

Weber number also characterizes the time required for bubble wrapping to reach equilibrium shapes. In other words, the higher the Weber number, the shorter the time required for the bubble to reach equilibrium shapes. It shows that the equilibrium bubble profiles with liquid fill level of 95% for bubble wrapping can be resulted with (a) We=56.65, ω=0.2 rpm, and time required to reach equilibrium at t=13,100 s; (b) We=14.18, ω=0.1 rpm, and time at t=34,200 s; and (c) We=3.54, ω=0.05 rpm, and time at t=87,000 s. Degrees of bubble wrapping with different Weber numbers for liquid fill level of 95% are illustrated in Figure 3(B). It shows that higher Weber number (higher rotating speed) suggests a higher degree of bubble wrapping. This figure shows that the minimum rotating speed for a completion of a full wrapping is 0.2 rpm with liquid fill level of 95%. In other words, bubble wrapping with a rotating speed less than 0.2 rpm will be ending at an incomplete bubble wrapping. Figure 3(B) also shows various angles of wrapping with liquid fill level of 95% for an incomplete bubble wrapping corresponding to different rotating speeds with ω<0.2 rpm. Angles of incomplete wrapping are 53°, 124°, and 178° for bubble wrapping with rotating speeds corresponding to 0.15, 0.1, and 0.05 rpm, respectively, with liquid fill level of 95%.

With reference to Figure 3(A) for bubble spin-up from rest to rotating

speed of 0.4 rpm with liquid fill level of 95%, Figure 4(A) shows the time evolution of bubble mass center fluctuations during the process of bubble wrapping around the dewar well. The figure shows the bubble mass center time evolution x_c, y_c and z_c along the x, y and z axes, respectively, in non-inertial bubble frame. This figure provides the following conclusions for bubble mass center fluctuations: (a) At time t = 0, the bubble with the spherical-shape was sitting at x_c = -38.2 cm, while y_c and z_c are basically located at a central position. (b) As the dewar container starts to spin-up, the bubble mass center along the x-axis gradually moves toward a central location while the bubble mass center along the y-axis shifts slightly from a central location with small amplitude oscillations and bubble mass center along the z-axis with negligible amplitude of oscillation. (c) The major driving forces for the oscillations of bubble mass fluctuations along the x- and y-axes are due to the centrifugal and Coriolis forces while none of these forces apply to the z-axis. (d) At the very beginning, x_c oscillates from - 38.2 cm toward the central position while y_c fluctuates from the central position toward negative y position. (e) Oscillation periods and amplitudes for bubble mass center fluctuations along the y-axis are such that the initial mode with a shorter periods (2000 s) and a greater amplitude (5 cm) and subsequent second mode with longer period (5000 s) and a smaller amplitude (3 cm). In other words, the bubble mass center oscillations along the y-axis change from a shorter period to a longer period, and from a greater amplitude to a smaller amplitude, and then gradually dies out. (f) Similar characteristics of the variation of a period and an amplitude for bubble mass center fluctuations and oscillations along the x-axis are shown which is similar to that of the figures along the y-axis.

Furthermore, one can study the time evolution of bubble mass center fluctuations with and without a completion of wrapping around the dewar well driven by the spin-up motion. Figures 4(B), 4(C), and 4(D) show bubble mass

center evolution with rotating speeds of 0.2, 0.15, and 0.05 rpm, respectively. These figures provide the following conclusions for bubble mass center fluctuations in addition to the conclusions given for Figure 3(A): (a) The bubble mass center oscillations along the x-axis finally move to a central location for the container rotating speeds $\omega \geq 0.2$ rpm while bubble mass center oscillations are ending at some equilibrium positions near but not at the central position for the container rotating speeds $\omega < 0.2$ rpm. (b) A greater gap between bubble equilibrium locations and central location along the x-axis is shown for the lower container rotating speeds or lower We number in comparison with $\omega = 0.2$ rpm and We=56.65 for minimum values required for the bubble to accomplish a complete wrapping process for the container liquid fill level of 95%.

Bubble spin-down from a complete wrapping with steady state is also investigated. At time t=0, the dewar container is spinning with 0.2 rpm with a full bubble wrapping around the dewar well for liquid-fill level of 95%. Figure 5(A) shows the time sequence evolution of the three dimensional bubble configuration and select times for spin-down motion of dewar with rotating speeds from 0.2 to 0.15 rpm. Bubble behaves dynamical evolution through the processes of deformations in terms of shrinking in the direction longitudinal to, and stretching in the direction transverse to the rotating axis, jointly, without unwrapping around the dewar well during spin-down motion.

Further decreasing of rotating speed during the spin-down motion than that illustrated in Figure 5(A) eventually causes the motion of bubble unwrapping around the dewar well for dewar with liquid fill level of 95%. Figure 5(B) shows the time sequence evolution of the three dimensional configuration at some select times for spin-down motion of dewar with rotating speeds from 0.2 to 0.05 rpm when bubble starts to unwrap around dewar well with liquid fill level of 95%. Figure 5(B) also clearly shows that the symmetric rotating bubble wrapping around the dewar well starts to create an asymmetric ripple along the surface of the

bubble at t=4,650 s. These ripple perturbations also quickly enhance and propagate. Finally the weakening centripetal forces resulted during the spin-down motion are unable to maintain the bubble wrapping around the dewar well. Thus, asymmetry in the imbalance liquid-vapor distribution is then starting to create.

There are some basic differences between the realistic practice and the theoretical computation for the problems of bubble spin-down motion in rotating dewar. In the theoretical computation, a symmetrical profile of distribution with respect to the rotating axis for centrifugal and Coriolis forces together with angular acceleration, which are all nothing but the function of angular velocity of rotating speed, shall be assumed during the time period of spin-down motion. In the realistic practice, a pronounced asymmetric force will be induced in these weakening forces of spin-down motion and initiates a cracking at this particular location of a symmetric force activating on the wrapped bubble which is the major cause of crack propapation leading to the final unwrapping of the rotating bubble around the dewar well. Thus, the symmetrical wrapping bubble will end up in unwrapping status during the spin-down motion. In the theoretical computation, one can never know where and when an asymmetric force shall be initiated unless this force is added into the computation artificially and arbitrarily. This is because there is no mechanism in the theoretical modelling to initiate such an asymmetric force to unwrap the rotating bubble to balance the weakening centrifugal forces during the spin-down motion. In other words, the basic differences between the realistic practice and computation are (a) the bubble will be unwrapped and still maintain in one piece or even two pieces encircling around the rotating dewar well depending upon the strength of surface tension which has a strong intention to maintain a single piece of rotating bubble for the case of realistic practice, and (b) the bubble will be broken into pieces because of the axial symmetric forces acting on the bubble with weakening

magnitude of centrifugal force which is unable to ensure bubble wrapping around the rotating dewar well for the case of theoretical computation[51].

The Weber numbers considered in the cases of bubble evolution, shown in Figures 5(A) and 5(B) are 31.87 and 3.54, respectively. It shows that the Weber number characterizes the possibility of the bubble with and without unwrapping around the dewar well. Results indicate that the rotating bubble can maintain its symmetric configurations without unwrapping around the dewar well if the Weber number is greater than 3.54 with dewar liquid fill level of 95%. Otherwise, the centripetal forces are too weak to maintain the rotating bubble without unwrapping around the dewar well.

A comparison of rotating dewar with liquid fill levels of 85 and 95% shows the results with the following conclusions: (a) The higher the liquid fill level of the rotating dewar, the higher the rotating speed required for a bubble to complete a full wrapping around the dewar well during spin-up motion (0.2 and 0.08 rpm rotating speeds are required for bubble to complete a full wrapping around dewar well with liquid fill levels of 95 and 85%, respectively.) (b) The higher the liquid fill level of the rotating dewar, the higher the rotating speed required for the bubble to maintain unwrapping around the dewar well during the spin-down motion (0.05 and 0.02 rpm rotating speeds are required to maintain a full wrapping bubble without unwrapping around the dewar well with liquid fill level of 95 and 85%, respectively). (c) The higher the liquid fill level of rotating dewar, the shorter the time required for the rotating bubble to accomplish a full wrapping around the dewar well (t=13,100 and 30,400 s are required for the rotating bubble to complete a full wrapping around the dewar well with liquid fill levels of 95 and 85%, respectively). (d) The higher the

liquid fill level of the rotating dewar, the shorter the time required for the rotating bubble during spin-down motion with full wrapping to become unwrapped from the minimum rotating speed required to accomplish a full wrapping during spin-up motion (t=4,650 and 10,600 s are required for the rotating bubble with full wrapping to become unwrapped from the minimum rotating speed required to accomplish a full wrapping around the dewar well with liquid fill levels of 95 and 85%, respectively, during the spin-down motion).

Comparison between minimum rotating speeds required for bubble to complete a full wrapping during spin-up motion, and minimum rotating speeds required for bubble to maintain a full wrapping without unwrapping around the dewar well during spin-down motion is quite different. It shows that a minimum speed to accomplish a full wrapping during spin-up motion, and a minimum speed to maintain a full wrapping without unwrapping during spin-down motion are 0.2 and 0.05 rpm, respectively, with liquid fill level of 95%, while the minimum rotating speeds for similar spin-up and spin-down motions are 0.08 and 0.02 rpm, respectively, with liquid fill level of 85%. These discrepancy in two figures between spin-up and spin-down motions are due to the fact that it needs additional energy to change any status of the most stable shape with minimum surface area required by the condition of minimum Gibbs free energy. The situation of the existence of energy barrier between these two motions which are very much similar to the motion of electron such as the thermionic-diode generator of the space-charge-barrier energy between cathode and anode.

VII. Rotating Bubble Subject to Lateral and Axial Impulses

In this review, the response of rotating bubble to impulsive disturbances is studied. In order to reduce the degree of asymmetry in the liquid-vapor distribution and damp its associated disturbances, a number of baffle are installed inside the dewar[50,54,55]. The difference in response on dewar with and without the baffle is also investigated.

Figures 6(A), 6(B), and 6(C) show three-dimensional configuration of baffle installation, the distribution of grid points for the dewar tank with baffle boards in the radial-axial plane and radial-circumferential plane, respectively, in cylindrical coordinates[56-60]. The baffle are installed with three parallel plates perpendicular to the rotating axis and four radial plates aligned with the rotating axis. The inner radius, outer radius and thickness of the three parallel baffle chosen in this review are 60, 77.48 and 0.1016 cm, respectively. These three baffles are installed at locations z_1, z_2, z_3 of 38.74, 80.94, and 84.4 cm, respectively. Four radial baffle-boards are located at 90° apart with the same inner and outer diameters and thickness as that of the three parallel baffles.

An example is given to illustrate sloshing dynamics in response to lateral impulse during the time period of guidance and/or attitude controls[63-66]. Dewar is spinning with a rotating rate of 0.1 rpm during its normal operation. In this review, with the following form of lateral impulse is assumed:

$\hat{a} = [a_x, a_y, a_z] = [1, 0, 0]\ 10^{-2} g_o$ in cartesian coordinates

$\hat{a} = [a_r, a_\theta, a_z] = [\cos\theta, -\sin\theta, 0]\ 10^{-2} g_o$ in cylindrical coordinates for

$0 < t \leq 10^{-2}$s

and $\hat{a} = [0.\ 0.\ 0]$ for $t > 10^{-2}$s

where g_o ($9.81 m/s^2$)is the Earth gravitational acceleration.

The time evolution of the bubble fluctuations without a baffle is first investigated. In order to illustrate that the bubble were experiencing finite deformation, Figure 27(A) shows the time evolution between time from 225 to 427 s for three-dimensional bubble oscillations without baffle. These three subfigures show a transition from left-side bubble swelling, equilibrium and right-side bubble swelling during these periods of time.

In this review, the time evolution of bubble oscillations for the container

with baffle due to the sloshing dynamics driven by the same impulse as that actuating on the dewar without baffle has been investigated. Figure 27(B) also illustrates the time evolution between time from 225 to 427 s for three-dimensional bubble oscillations for rotating dewar with baffle to show that bubble was experiencing finite deformation with a transition from left-side bubble swelling, equilibrium, to right-side bubble swelling.[54,55]

Another example is given to illustrate sloshing dynamics in response to axial impulse during the time period of guidance and/or attitude controls.[60,61] Dewar container is also spinning with a rotating rate of 0.1 rpm during its normal operation. In this review, the container bound coordinates with the following form of axial impulse are assumed:

$\hat{a} = [a_x, a_y, a_z] = [0, 0, 1]\ 10^{-2} g_o$ in cartesian coordinates

$\hat{a} = [a_r, a_\theta, a_z] = [0, 0, 1]\ 10^{-2} g_o$ in cylindrical coordinates for $0 < t \leq 10^{-2}$s and $\hat{a} = [0.\ 0.\ 0]$ for $t > 10^{-2}$s

Because of page limitation, time sequence evolution of bubble deformations activated by the axial impulse without and with baffle will not be illustrated in this review. Results of computer simulation show that the bubble is inflated at the lower half of the bubble as liquid is pushed upward along the axial direction at the very beginning; and then the bubble is inflated at the upper half of the bubble as the liquid is pushed downward along the axial direction during the up and down oscillations activated by axial impulse.

Bubble mass center fluctuations driven by lateral and axial impulses have also been studied. Figures 8(A) and 8(B) show the time evolution of bubble mass center at (x_c, y_c, z_c) driven by the lateral and axial impulses, respectively. Figure 8(A) shows the time evolution of the growth and decay of the bubble mass center fluctuations with solid lines for the rotating dewar with baffle in response to the impulse. Figures 8(A-a), 8(A-b), and 8(A-c) show the time evolution of the locations of the fluid mass center fluctuations in x_c, y_c, and

fluctuating locations in radial axis of cylindrical coordinates R_c [= (x_c^2 + $y_c^2)^{1/2}$], respectively, for the container with baffle. Similar to the container without baffle, the effect of Coriolis forces which carry over the fluctuations from x- to y-axes also applies to this case. This means that the fluid mass center fluctuations are primarily in the x- and y-axes and not in the z-axis. The locations of maximum absolute values of the fluid mass center fluctuations in the radial direction are Max($|x_c|$, $|y_c|$)=(2.24, 1.67) cm; while the fluctuating values of the maximum fluid mass center disturbances in the radial coordinates are Max(Δx_c, Δy_c)=(2.64, 2.52) cm. Similarly, it also shows $\Delta x_c > \Delta y_c$ for fluctuating fluid mass center disturbances in rotating dewar with baffle in response to the impulse along the x-axis.

A comparison between the container with and without baffle also illustrates some peculiar behavior of cryogenic helium fluids with temperature below λ-point (2.17 K) in which helium demonstrates a number of remarkable properties of superfluidity such as extremely low viscous and surface tension coefficients in response to impulse in microgravity environment. It can be concluded as follows: (a) Impulse started to actuate on the fluid system at time t = 0 with peak value and end at t = 10^{-2}s for both the container with and without baffle. However, the fluid mass center fluctuations reacted gradually in response to the impulse with a maximum amplitude of fluid mass center fluctuations in the x-axis about the same time as that between the container with and without baffle at time t = 80 s, there is a 15 s delay of maximum amplitude fluid mass center fluctuations in the y-axis for the container with baffle than that for the container without baffle. (b) Displacement of fluid mass center was sinusoidally shifting continuously for both the container with and without baffle even long after the ending of the impulsive force. This displacement of fluid mass center in the radial direction for both cases reached the maximum value at 82 s after the ending of impulsive force. Then the fluid mass center started to oscillate back

and forth with a longer period of oscillations for the container with baffle than that for container without baffle due to the effects of surface tension forces and viscous forces for the container with baffle, in addition to the reflection and bouncing of flows from the wall. (c) The oscillations of fluid mass center fluctuations continued for a long period of time even after the ending of impulsive forces due to extremely low viscosity of helium II fluid which eventually exponentially decays the mass center fluctuations. (d) As for the effect of viscous force between the liquid and solid interface in the container with baffle, it contributes a greater damping effect of mass center fluctuations. A comparison of the container with and without baffle shows that the container with baffle can reduce 13% of the maximum value of fluid mass center dislocation and decrease 25% of the maximum amplitude of fluid mass center fluctuations than that for the container without baffle.

Figure 8(B) shows the time evolution of the growth and decay of the fluid mass center fluctuations with broken lines in the rotating dewar without baffle in response to the axial impulse. The fluid mass center at time t = 0 is located at (x_c, y_c, z_c) = (0, 0, 80.9) cm. The highest amplitude fluctuations of fluid mass center is located at Max (x_c, y_c, z_c) = (0, 0, 86.3) cm at time t = 138 s, while the lowest amplitude fluctuations of fluid mass center is located at Min (x_c, y_c, z_c) = (0, 0, 76.6) cm at time t = 406 s for dewar without baffle. In this simulation, it shows that fluid mass center fluctuations reach to its maximum values at 138 s after the ending of the impulse actuating on the rotating dewar. The wave period of fluid mass center fluctuation is about 500 s for dewar without baffle.

Figure 8(B) also shows the time evolution of the growth and decay of the fluid mass center fluctuations with solid lines in the rotating dewar with baffle in response to the impulse. The highest amplitude fluctuations of fluid mass center is located at Max (x_c, y_c, z_c) = (0, 0, 84.2) cm at time t = 161 s, while

the lowest amplitude fluctuations of fluid mass center is located at Min (x_c, y_c, z_c) = (0, 0, 80) cm at time t = 863 s for dewar with baffle. In this simulation, it shows that fluid mass center fluctuations reach to its maximum at t = 161 s after the ending of the impulsive thrust actuating on the rotating dewar. The wave period of fluid mass center fluctuation is about 1000 s.

A comparison between the container with and without baffle in response to impulse in microgravity environment it can be concluded as follows: (a) Impulse started to actuate the fluid system at time t = 0 with peak value and end at t = 10^{-2}s for both the container with and without baffle. However, the fluid mass center fluctuations reacts gradually in response to the impulse with a maximum amplitude of fluid mass center fluctuations in the z-axis at t = 138 s for dewar without baffle, and at t = 161 s for dewar with baffle, a 23 s delay for dewar with baffle to that for dewar without baffle. (b) The oscillations of fluid mass center fluctuations continue for a long period of time even after the ending of impulse due to extremely low viscosity of helium II fluid which eventually decays the mass center fluctuations. (c) As for the effect of drag force between the liquid and solid interface in the container with baffle, the installation contributes greatly in the increasing of wave period oscillation for the dewar with baffle, which shifts the wave period from about 500 s for dewar without baffle to about 1000 s for the dewar with baffle. (d) The baffle also contributes to the reduction of fluid mass center fluctuations. Results show that the container with baffle can reduce 40% of the maximum amplitude of fluid mass center fluctuations and decrease 70% of the minimum amplitude of fluid mass center fluctuations than that for the container without baffle.

VIII. Bubble Deformations Subject to Gravity or G-Jitter Acceleration Associated with Slew Motion

By using the mathematical formulations illustrated in Sections II and III, one can numerically simulate bubble sloshing dynamics associated with slew

motions depending upon the specific scientific missions assigned to the spacecraft. An example is given to illustrate sloshing dynamics associated with slew motion for the AXAF-S spacecraft.

(VIII-A) Bubble Deformation Driven by Gravity Gradient Acceleration Associated with Slew Motion

As indicated earlier, the AXAF-S spacecraft is capable of observing point and extended sources of active galactic nuclei, clusters of galaxies, supernova remnants, x-ray binaries, etc., through the spacecraft slew motion of pointing control. Assuming that slew motion is along the y"-axis (see Figure 1), gravity gradient acceleration associated with slew motion can be computed from the non-inertial frame expressions of Equations (2-12) and (2-17). It is assumed that the slew motion operates at 90° in 600 s.

In this example, spacecraft sloshing dynamics driven by gravity gradient acceleration associated with slew motion in the y"-axis, shown in Figure 1, have been investigated. As the orbital period of AXAF-S spacecraft is 97.6 min and period of 90° slew motion in the y"-axis is 600 s, the component of gravity gradient acceleration along the (x, y, z) directions acted on the fluid mass located at $(r, \theta, z) = (12\ cm, \pi/2, 3\ cm)$ is shown in Figure 9(A). This figure shows that the magnitude of gravity gradient acceleration is on the order of 10^{-7} g_o for AXAL-S dewar on its operation orbit. The distance from the spacecraft mass center to the bottom of the dewar, L_c, shown in Figure 1, is 257.8 cm.

The equilibrium shape of the liquid-vapor interface for a dewar with 70% liquid-fill level under a residual gravity environment below 10^{-7} g_o, is a sphere. Figure 10(A) shows the time sequence evolution of the three-dimensional dynamical behavior of the bubble oscillations driven by gravity gradient acceleration associated with slew motion. The figures of liquid-vapor interface profiles with the time sequences chosen in this review are at time t = 334, 392, 431, 456, 487, 524, 554, 588, 600, 695, 784, and 800 s. It clearly shows that

there is a series of asymmetric oscillations excited along the surface of sloshing dynamics governed liquid-vapor interface driven by asymmetric gravity gradient acceleration associated with slew motion.

Comparison between Figures 9(A) and 10(A) shows the following results: (a) Components of gravity gradient acceleration in x and z directions are pointing toward the negative sides, which implies that the forces are pointing toward the southwestern direction. This indicates that the liquid is pushed toward the southwestern direction while the bubble is pushed toward the northeastern direction. These results are exactly shown in Figure 10(A). (b) Uneven and imbalance flow velocities toward the southwestern direction create similar uneven and imbalance pressure distribution reacting to bubble toward the northeastern direction. Because of extremely low surface tension coefficients of helium II between the liquid-vapor interface, a deformed irregular concave and convex-shaped oscillating bubble is created.

Figure 11(A) shows time fluctuations of the locations of bubble mass centers of the fluids inside the dewar container due to sloshing dynamics driven by gravity gradient acceleration associated with slew motion. The values of bubble mass center fluctuations are $(\Delta x_c, \Delta y_c, \Delta z_c) = (11.8, 1.25, 18.4)$ cm. It shows $\Delta z_c > \Delta x_c > \Delta y_c$ for bubble mass center fluctuations driven by gravity gradient acceleration associated with slew motion.

The trend of the bubble mass center fluctuations, $\Delta z_c > \Delta x_c > \Delta y_c$, exactly reflects the values of the major driving forces of gravity gradient acceleration associated with slew motion in which it shows $g_z > g_x > g_y$ as that shown in Figure 9(A).

Figures 12(A-a), 12(A-b), and 12(A-c) show the computed time variation of the fluctuations of slosh reaction forces acting on the dewar container driven by gravity gradient acceleration associated with slew motion in the y-axis with components along the x-, y-, and z-axes respectively. These figures show the

following results: (a) The values of slosh reaction force fluctuations are (ΔF_x, ΔF_y, ΔF_z) = (59.2, 4.11, 61.02) dynes; This clearly indicates $\Delta F_z > \Delta F_x > \Delta F_y$. The maximum absolute values of slosh reaction force are Max ($|F_x|$, $|F_y|$, $|F_z|$) = (47.42, 4.11, 78.68) dynes. This also indicates $|F_z| > |F_x| > |F_y|$. (b) The initial values of F_x and F_y start from zero, while that of F_z starts from a nonzero value. This is due to the fact that the major driving force of gravity gradient acceleration associated with slew motion at the beginning of slew motion is equal to zero along the x- and y-axes, and is non-zero along the z-axis. (c) The characteristics of slosh reaction forces and their fluctuations are more likely to follow the trend of the major driving force of gravity gradient acceleration associated with slew motion in the y-axis as that shown in Fig. 11. Comparison between Fig. 12(A) and 9(A) reflects that the fluid system serves as a nonlinear modulator of spring mass and damper systems amplifying and damping the forces acting on the fluid flows and then responds back to the spacecraft[58-63].

Figures 12(B-a), 12(B-b), and 12(B-c) show the variations of slosh reaction moments acting on the dewar container due to bubble deformations driven by gravity gradient acceleration associated with slew motion with components along the x, y, and z axes, respectively. These figures show the following results: (a) The values of slosh reaction moment fluctuations are (ΔM_x, ΔM_y, ΔM_z) = (770.6, 10784.5, 0.0004) dyne·cm. The maximum absolute values of slosh reaction moment are Max ($|M_x|$, $|M_y|$, $|M_z|$) = (770.6, 8595.9, 0.0004) dyne·cm. (b) Because slew motion is in the y-axis, the magnitudes of both ΔM_y and $|M_y|$ are the maximum. (c) As slew motion is in the y-axis, the value of the moment arm along the y-axis is zero; and also, because the y-component of the major driving force of gravity gradient acceleration associated with slew motion in the y-axis is equal to zero, the magnitude of $|F_y|$ is near zero. Both $|F_y| \sim L_y \sim 0$; thus, $M_z = L_x F_y - L_y F_x \sim 0$.

Figures 12(C-a), 12(C-b) and 12(C-c) show time fluctuations of the moment arms of slosh reaction moments exerted on the dewar container due to bubble deformations driven by gravity gradient acceleration associated with slow motion in the y-axis for components along the x-, y-, and z-axes, respectively. These figures show the following results: (a) The values of moment arm fluctuation are $(\Delta L_x, \Delta L_y, \Delta L_z) = (119.2, 11.7, 156.1)$ cm. The maximum absolute values of slosh reaction moment are Max $(|L_x|, |L_y|, |L_z|) = (91.3, 11.7, 257.8)$ cm. This shows $\Delta L_x > \Delta L_y > \Delta L_z$ and $|L_x| > |L_y| > |L_z|$. (b) Spacecraft slew motion s along the y-axis; thus, the value of L_y is the minimum, and that of M_y is the maximum. (c) Because L_z is the function of $F_x M_y$, the value of M_y is the maximum, and that of F_x is near the maximum. Thus, the values of L_z are maximum. (d) The trend of the fluctuations of momentum arm is very much like that of the slosh reaction forces acting on the dewar container of the spacecraft. Also, the trend of the fluctuations of moment arm is very much like that of the major driving forces of gravity gradient acceleration associated with slew motion in the y-axis [see Figs. 12(C) and 9].

(VIII-B) Bubble Deformation Driven by G-Jitter Acceleration Associated With Slew Motion

By using the mathematical formulations illustrated in Equations (2-3) to (2-11) and (2-18), one can numerically simulate spacecraft sloshing dynamics associated with spinning and/or slew motions depending upon the specific scientific missions assigned to the spacecraft.

If slew motion operates with a range of 90° in 10 min (= 600 s), the component of g-jitter acceleration along the (x, y, z) directions acted on the fluid mass located at $(r, \theta, z) = (12 \text{ cm}, \pi/2, 3 \text{ cm})$ is shown in Figure 9(B). This figure shows that the magnitude of slew motion induced acceleration is on the order of 10^{-5} g_o.

The equilibrium shape of the liquid-vapor interface for a dewar with 70%

liquid-fill level under a residual gravity environment below 10^{-6} g_o is a sphere. Figure 10(B) shows the time sequence evolution of the three-dimensional behavior of the interface oscillations driven by g-jitter acceleration associated with slew motion. It is shown in this figure that a time sequence evolution of liquid-vapor interface profiles at time t = 60.4, 258, 323, 354, 379, 403, 430, 528, 572, 628, 663, and 800 s are illustrated. It clearly shows that there are a series of asymmetric oscillations excited along the surface of sloshing dynamics governed liquid-vapor interface driven by asymmetric g-jitter acceleration associated with slew motion[57-59].

For the convenience of explanation for the movement of bubbles at various locations in the figures of x-y, x-z and y-z planes, let us adopt the following conventional ways of direction illustration: (1) Choose positive-x, negative-x, positive-y, negative-y as the eastern, western, northern, and southern directions, respectively, in the x-y plane; (2) Choose positive-x, negative-x, positive-z, and negative-z as the eastern, western, northern and southern directions, respectively, in the x-z plane; and (3) Choose positive-y, negative-y, positive-z, and negative-z as the eastern, western, northern and southern directions, respectively, in the y-z plane.

Figure 9(B) shows that g-jitter acceleration associated with slew motion is pointing toward the southeastern direction at the very beginning and then is pointing toward the southwestern direction at the end in the x-z plane, and also is pointing toward the southern direction in the y-z plane. These indicate that liquid is pushed toward the southeastern and then toward the southwestern directions (the bubble is pushed toward the northwestern and then toward the northeastern directions) while the liquid is pushed toward the southern direction (the bubble is pushed toward the northern direction).

Based on Figure 9(B), it shows that g-jitter acceleration associated with slew motion is pointing toward the eastern direction at the beginning and then

pointing toward the western direction at the end in the x-y plane. This implies that the liquid is pushed toward the eastern direction and then toward the western direction while bubble is pushed toward the western direction and then toward the eastern direction in the x-y plane.

Comparison between Figures 9(B) and 10(B) illustrate some peculiar behavior of helium fluids with temperature below λ-point (2.17 K) in which helium demonstrates a number of remarkable properties of superfluidity such as extremely low viscous and surface tension coefficients reacting to the disturbances driven by jitter acceleration associated with slew motion. It can be concluded as follows: (a) G-jitter acceleration associated with slew motion started at time t = 0. However, bubble mass center fluctuations did not start to react to the driven force until t = 80 s for x_c and t = 160 s for z_c. In other words, bubble configuration was in perfect spherical-shaped at 80 s after g-jitter acceleration associated with slew motion was applied. (b) x-component g-jitter acceleration associated with slew motion was applied to the fluid element with positive value from t = 0 to 300 s; negative value from t = 300 to 600 s; and zero value after t = 600 s. However, westward movement of bubble continued from t = 80 to 450 s, and then switched to eastward movement t = 800 s which was 200 s after acceleration vanished. Obviously, there is a phase-lag between action of force and reaction of motion. (c) The z-component g-jitter acceleration associated with slew motion was applied to the fluid element with negative value from t = 80 to 500 s and the zero value after t = 500 s. However, the northward movement of the bubble started at t = 160 s; bounced back from the wall at t = 530 s; and then the southward movement continued to t = 800 s which was 300 s after acceleration vanished. Obviously, the motion continued for a long period of time even after the applied force vanished due to extremely low viscosity of helium II fluids. (d) An intensive oscillation of bubble with a deformation of irregular concave and convex-shaped continued and sustained for several hundred

seconds after the applied force vanished due to extremely low surface tension coefficient for helium II fluids.

Figure 11(B) shows time evolution of the locations of bubble mass centers of fluids inside the dewar container due to sloshing dynamics driven by g-jitter acceleration associated with slew motion. The values of bubble mass center fluctuations are $(\Delta x_c, \Delta y_c, \Delta z_c) = (28.9, 0.44, 30.2)$ cm. It shows $\Delta z_c > \Delta x_c > \Delta y_c$ for bubble mass center fluctuations driven by jitter acceleration associated with slew motion. Behavior of bubble mass center fluctuations, shown in Figure 11(B) are the exact reflection of the behavior of jitter accelerations, shown in Figure 9(B).

Comparison between Figures 9(B), 10(B) and 11(B) illustrate some peculiar behavior of helium fluids with temperature below λ-point (2.17 K) in which helium demonstrates a number of remarkable properties of superfluidity such as extremely low viscous and surface tension coefficients reacted to the disturbances driven by jitter acceleration associated with slew motion. It can be concluded as follows: (a) g-jitter acceleration associated with slew motion started at time $t = 0$. However, bubble mass center fluctuations did not start to react to the driven force until $t = 80$ s for x_c and $t = 160$ s for z_c. In other words, bubble configuration was in perfect spherical-shaped at 80 s after g-jitter acceleration associated with slew motion was applied. (b) x-component g-jitter acceleration associated with slew motion was applied to the fluid element with positive value from $t = 0$ to 300 s; negative value from $t = 300$ to 600 s; and zero value after $t = 600$ s. However, westward movement of bubble continued from $t = 80$ to 450 s, and then switched to eastward movement to $t = 800$ s which was 200 s after acceleration vanished. Obviously, there is a phase-shift between action of force and reaction of motion. (c) The z-component g-jitter acceleration associated with slew motion was applied to the fluid element with negative value from $t = 80$ to 500 s and the zero value after $t = 500$ s. However, the northward movement

of the bubble started at t = 160 s; bounced back from the wall at t = 530 s; and then the southward movement continued to t = 800 s which was 300 s after acceleration vanished. Obviously, the motion continued for a long period of time even after the applied force vanished due to extremely low viscosity of helium II fluids. (d) An intensive oscillation of bubble with a deformation of irregular concave and convex-shaped continued and sustained for several hundred seconds after the applied force vanished due to extremely low surface tension coefficient for helium II fluids.

Figures 13(A-a), 13(A-b) and 13(A-c) show the computed time variation of the fluctuations of slosh reaction forces exerted on the dewar container driven by g-jitter acceleration associated with slew motion in the y-axis with components along the x-, y-, and z-axes, respectively. These figures show the following results: (a) The values of slosh reaction forces are (ΔF_x, ΔF_y, ΔF_z) = (2.27, 0.04, 1.37) 10^3 dynes, it clearly indicates $\Delta F_x > \Delta F_z > \Delta F_y$). The maximum absolute values of slosh reaction forces are Max $|F_z| > |F_x| > |F_y|$ = (1.15, 0.02, 1.20) 10^3 dynes. It also indicates $|F_z| > |F_x| > |F_y|$. (b) The initial values of F_x, F_y, and F_z all start from zero value because there was no slew motion applied to the system at time = 0. (c) The magnitudes and fluctuations of F_y are much smaller than those of F_x and F_z because the major driving moment of slew motion is along the y-axis. (d) The characteristics of slosh reaction forces and their fluctuations are ore likely to follow the trend of the major driving force of g-jitter acceleration associated with slew motion in the y-axis as that shown in Figure 9(B). Comparison between Figures 13(A) and 9(B) reflects that the fluid systems serves as a damping modulator for the forces acting on the fluid flows and then responds back to the dewar container are due to the disturbances caused by the sloshing dynamics of the fluid system.

Figures 13(B-a), 13(B-b), and 13(B-c) show the variations of slosh reaction moments exerted on the dewar container due to bubble deformations driven by g-

jitter acceleration associated with slew motion with components along the x, y, and z axes, respectively. These figures show the following results: (a) The values of slosh reaction moment fluctuations are (ΔM_x, ΔM_y, ΔM_z) = (7.53, 422.79, 0.0001) 10^3 dyne•cm. The maximum absolute values of slosh reaction moment are Max ($|M_x|$, $|M_y|$, $|M_z|$) = (4.31, 214.53, 0.0006) 10^3 dyne•cm. (b) As slew motion is in the y-axis, the magnitudes of both ΔM_y and $|M_y|$ are the maximum. (c) As slew motion is in the y-axis, the value of the moment arm along the y-axis is zero; and also as the y-component of the major driving force of g-jitter acceleration associated with slew motion in the y-axis is equal to zero, the magnitude of $|F_y|$ is near zero. Since both $|F_y| \sim L_y \sim 0$, it leads $M_x = L_yF_z - L_zF_y \sim 0$ and $M_z = L_xF_y - L_yF_x \sim 0$.

Figures 13(C-a), 13(C-b) and 13(C-c) show the time fluctuations of the moment arms of slosh reaction moments exerted on the dewar container due to bubble deformations driven by g-jitter acceleration associated with slew motion in the y-axis for components along the x-, y-, and z-axes, respectively. These figures show the following results: (a) The values of moment arm fluctuations are (ΔL_x, ΔL_y, ΔL_z) = (190.4, 56.1, 186.6) cm. The maximum absolute values of moment are ($|L_z|$, $|L_x|$, $|L_y|$) = (95.4, 49.8, 186.6) cm. It shows $\Delta L_x > \Delta L_y > \Delta L_z$) and $|L_z| > |L_x| > |L_y|$. (b) As spacecraft slew motion is along the y-axis, the values of L_y are the minimum, and M_y are the maximum. (c) As L_z is the function of F_xM_y ($F_yM_x \sim 0$ because $F_y = 0$), the values of M_y are the maximum and F_x is near the maximum. This makes the values of L_z the maximum. (d) The trend of the fluctuations of omentum arm is very much like that of the slosh reaction forces acting on the dewar container of the spacecraft. Again, the trend of the fluctuations of moment arm is very much like that of the major driving forces of g-jitter acceleration associated with slew motion in the y-axis [see Figures 13(C) and 9(B)].

IX. Rotating Bubble Subject Various Magnitudes of Gravity

Gradient and g-Jitter Accelerations

The characteristics of gravity gradient and g-jitter accelerations, shown in Equations (2-14) and (2-18), respectively, are quite different. Gravity gradient acceleration shows the following characteristics: (a) acceleration acts on any fluid mass inside the container which increases two units of acceleration per unit of distance measured from the container mass center to the location of the fluid mass parallel along the radial axis from the container mass center to the center of the Earth; (b) the acceleration acts on the fluid mass which decreases one unit of acceleration per unit of the shortest distance measured from the location of the fluid mass to the radial axis along the vector from the container mass center to the center of the Earth[1]. For example, Figure 14(A) shows the time variation of gravity gradient accelerations for an assumed turn-around period of 1200 s with a container rotating speed of 0.1 rpm for components along (x, y, z) directions acted on the fluid mass located at (r, θ, z) = (40 cm, $\pi/4$, 10 cm). As the magnitude and direction of gravity gradient acceleration acting on each fluid mass is strongly dependent upon how far the location of the fluid mass deviates from the container mass center measured along the axis parallel to the vector $\hat{r}_c$ which varies with respect to time, it shows that the gravity gradient acceleration acting on the fluid mass is different for fluid mass at different locations in the container. Figure 14(A) shows that the magnitude of gravity gradient acceleration is on the order of 10^{-7} g_o. On the contrary to gravity gradient acceleration which exerts different acceleration on the fluid mass at different locations in the container, g-jitter acceleration drives the same acceleration on the fluid mass at different locations in the container. Figure 14(B) shows the time variation of g-jitter accelerations for a turn-around period of 1200 s with a container rotating speed of 0.1 rpm and a g-jitter frequency of 0.1 Hz for components along (x, y, z) directions acted on the fluid mass everywhere in the container. It is shown in Figure 9(A) that

gravity gradient accelerations are on the order of 10^{-7} g_o for the spacecraft orbit chosen in this example, three ranges of background gravity, 10^{-6}, and 10^{-8} g_o for g-jitter accelerations correspond to the magnitude of acceleration higher, and lower, respectively, than that of the gravity gradient acceleration acting on the fluid system of the spacecraft.

The equilibrium shape of the liquid-vapor interface for a rotating dewar under a residual gravity environment below $10^{-6}g_o$ and rotating speed of 0.1 rpm is very much alike and is a doughnut configuration with a near circular kidney-shape cross-section based on the computation of the numerical algorithm developed in our earlier studies[7-9,20]. In this study, the combined gravity gradient and three ranges of g-jitter (10^{-6}, and 10^{-8} g_o) accelerations acting on the liquid-vapor interface oscillations have been reviewed and investigated[60-64].

(IX-A) Combined Gravity Gradient and 10^{-8} g_o Background g-Jitter Accelerations Acting on Liquid-Vapor Interface Oscillations

In this case, the combined effects of gravity gradient and g-jitter accelerations are completely dominated by the gravity gradient acceleration when the 10^{-8} g_o and less background g-jitter accelerations are applied simultaneously with gravity gradient acceleration [which is on the order of 10^{-7} g_o as shown in Figure 14(A)] for the excitation of slosh waves along liquid-vapor interface oscillations.

Figure 15(A) shows the time sequence evolution of the liquid-vapor interface profiles driven by these combined accelerations. For the convenience of comparison, figures of liquid-vapor interface profiles with the same values of the time sequences chosen throughout this section are at time t = 191, 354, 380, 431, 503, 603, 825, 980, 995, 1050, 1080 and 1200 s. It clearly shows that there is a series of asymmetric oscillations excited along the surface of liquid-vapor interface driven by asymmetric gravity gradient-dominated acceleration.

Careful examination of the case of gravity gradient-dominated acceleration-

effected liquid-vapor interface oscillations, gravity gradient acceleration shown in Equation (2-12), indicate that there are greater negative components of acceleration longitudinal to the direction aligned with spacecraft mass center to the Earth center, and smaller positive components of acceleration transverse to this direction. As we indicated in Equation (2-2), angle ψ_g varies with time. This phenomena shows that the gravity gradient acceleration exerted on the spacecraft is equivalent to the combination of time dependent force with turn-around direction and torsional moment acting on the spacecraft when it is orbiting around the Earth. It shows in Figure 15(A) that the deformation of the bubble is created by asymmetric torsional moment with a twisting force.[65-69]

Figure 15(A) shows the time sequence evolution of the three-dimensional dynamical behavior of the interface oscillations driven by gravity gradient-dominated acceleration. It indicates that the bubble (helium vapor) configurations change from axial symmetric to asymmetric profiles at a plane aligned with the vector of gravity gradient acceleration. The gravity gradient-dominated acceleration produces a combination of time dependent torsional movement with tidal motion of bubble oscillations in the rotating dewar when it is orbiting around the Earth.

Figure 14(C) shows the time evolution of bubble mass center at (x_c, y_c, z_c) for three cases described above. The time history of both gravity gradient and g-jitter accelerations are plotted in Figure 14(B). Time evolution of bubble oscillations driven by gravity gradient-dominated, and g-jitter-dominated acceleration are illustrated in Figures 15(A), and (B), respectively.

Figure 14(C-a) shows time fluctuations of the locations of bubble mass centers of the rotating container due to slosh waves excited by gravity gradient-dominated acceleration. The values of bubble mass center fluctuations are (Δx_c,

Δy_c, Δz_c) = (4.54, 2.83, 2.32) cm. It shows $\Delta x_c > \Delta y_c > \Delta z_c$ for bubble mass center fluctuations driven by gravity gradient-dominated acceleration.

As mentioned earlier, the combined effects of gravity gradient and g-jitter accelerations are completely dominated by gravity gradient acceleration when the 10^{-8} g_o and less g-jitter accelerations are applied simultaneously with gravity gradient acceleration which drive slosh reaction forces and its moment fluctuations due to bubble deformations.

Figure 16(A) shows the computed time variation of the fluctuations of slosh reaction forces exerted on the dewar container driven by gravity gradient-dominated acceleration. This figure shows the following results: (a) The values of slosh reaction force fluctuations are (ΔF_x, ΔF_y, ΔF_z) = (23.7, 18.3, 61.7) dynes, it clearly indicates $\Delta F_x > \Delta F_y > \Delta F_z$. The maximum absolute values of slosh reaction force are Max ($|F_x|$, $|F_y|$, $|F_z|$) = (17.4, 11.5, 32.4) dynes. It also indicates $|F_z| > |F_x| > |F_y|$. (b) The initial values of F_x and F_y start from zero value while that if the F_z starts from non-zero value. This is due to the fact that the shape of rotating bubble is symmetric with respect to the x and y axes which makes F_x and F_y equal to zero at time t = 0 while the resultant force along the rotating axis of z is not equal to zero because of pre-existing gravity force acting along the z-axis at the very beginning. (c) The characteristics of slosh reaction forces and their fluctuations are very much following the trend of dominated gravity gradient acceleration , shown in Figure 7. In other words, gravity gradient acceleration as a major input force, modulated by sloshing dynamics of the fluid system in the dewar, activate on the dewar container with response force. In reality, the fluid system, modulated by sloshing dynamics, acts as a damper in the spacecraft to damp out the acting force of gravity gradient acceleration[43-47].

Figures 16(B-a), 16(B-b), and 16(B-c) show variations of slosh reaction torque exerted on the dewar container due to slosh waves driven by gravity

gradient-dominated acceleration along the x, y, and z axes, respectively. The values of slosh reaction torque fluctuations are (ΔM_x, ΔM_y, ΔM_z) = (761.9, 667.3, 0.06) dyne•cm. The maximum absolute values of slosh reaction torques are Max ($|M_x|$, $|M_y|$, $|M_z|$) = (392.9, 343.4, 0.50) dyne•cm. It shows $\Delta M_x > \Delta M_y > \Delta M_z$ and $|M_x| > |M_y| > |M_z|$. As M_x, M_y, M_z are determined by the Factors (F_x, L_z, F_z, L_x), (F_z, L_y, F_y, L_z) and (F_y, L_x, F_x, L_y), respectively, it was illustrated in Figures 32 and 34 that the magnitudes of force fluctuations give $|F_z| > |F_x| > |F_y|$ and that of moment arm fluctuations give $|L_z| > |L_x| > |L_y|$ in which time averages of L_x and L_y were approaching zero. This explains why the moment of $M_z = L_xF_y - L_yF_x - 0$ even though there is a rolling moment with angular velocity of 0.1 rpm in which the induced rolling moment exerted by the viscous rotating fluids is small in comparison with the induced pitch and yaw moments due to asymmetric slosh wave excitation.

Figure 16(C) shows time fluctuations of moment arms of slosh reaction torques exerted on the dewar container due to bubble deformations excited by gravity gradient-dominated acceleration. The values of moment arm fluctuations are (ΔL_x, ΔL_y, ΔL_z) = (22.8, 19.0, 45.5) cm. The maximum absolute values of moment arm are Max ($|L_x|$, $|L_y|$, $|L_z|$) = (12.2, 10.2, 103.4) cm. It shows $\Delta L_x > \Delta L_y > \Delta L_z$ and $|L_x| > |L_y| > |L_z|$. This trend is very much similar to the driving force of gravity gradient acceleration, shown in Figure 14(A).

(IX-B) Combined Gravity Gradient and 10^{-6} g_o Background g-Jitter Accelerations Acting on Liquid-Vapor Interface Oscillations

In this case, the combined effects of gravity gradient and g-jitter accelerations are completely dominated by the g-jitter acceleration.

Figure 15(B) shows the time sequence evolution of the dynamical behavior of the liquid-vapor interface oscillations driven by g-jitter-dominated acceleration of 0.1 Hz low g-jitter frequency. It clearly shows that there is a series of asymmetric oscillations excited along the surface of liquid-vapor

interface driven by asymmetric g-jitter-dominated acceleration.

Careful examination of the case of g-jitter acceleration-dominate liquid-vapor interface oscillations indicates that there is a sinusoidal oscillation longitudinal to the direction aligned with spacecraft mass center to Earth center. As indicated in Equation (2-2), the angle ψ_g varies with time. This phenomena shows that the g-jitter acceleration exerted on the spacecraft is equivalent to time-dependent oscillatory forces which push the bubble in the combined directions of down-and-up [see z-component of g-jitter acceleration shown in Figure 14(B)] and leftward-and-rightward [see x-and-y components of g-jitter accelerations shown in Figure 14(B)] as the bubble is rotating with respect to the spacecraft rotation axis. The down-and-up motion of the bubble is due to the fact that z-component g-jitter acceleration decreases from the maximum downward direction to the minimum downward direction, during the time period between t = 0 to t = 300 s, which pushes the liquid downward and the bubble upward; while the g-jitter acceleration changes to its downward direction and magnitude from the minimum upward to the maximum upward, and then back to the minimum upward, during the time period between t = 300 s to t = 900 s, which pushes the liquid upward and the bubble downward; in the meanwhile, the g-jitter acceleration changes to its downward direction and magnitude during the period from t = 900 s to 1200 s which repeats the half cycle story of the time period from t = 0 to t = 300 s. The leftward-and-rightward oscillations of bubble are the results of positive and negative directions of g-jitter accelerations in the x- and y-components as that illustrated in Figure 14(B). The positive direction g-jitter acceleration implies that the liquid is pushed rightward and the bubble is driven leftward. The time variations of g-jitter accelerations, shown in Figure 14(B), characterize the leftward and rightward oscillations of the bubbles shown in Figure 15(B).

In addition to the 0.1 Hz low frequency jitter-dominated acceleration, 1.0

Hz medium frequency and 10 Hz high frequency jitter acceleration driven liquid-vapor interface oscillations have also been investigated. The characteristics of these three ranges of g-jitter frequencies have been well-documented in the earlier studies[10-20]. Because of page limitation, oscillations driven by the time-dependent variations of g-jitter-dominated acceleration with medium and high frequencies will not be shown in this review. It is also worthwhile to mention that the natural frequency of a cryogenic helium container is much closer to the low frequency g-jitter acceleration than that of the medium and high frequencies. Results show that lower frequency g-jitter-dominated acceleration contribute more in the driving of asymmetric profiles of the interface than the higher frequency g-jitter-dominated acceleration. These results are agreeable with the earlier studies[10-20].

Figure 14(C-b) shows time fluctuations of the locations of bubble mass centers of the rotating container due to slosh waves excited by asymmetric gravity jitter-dominated acceleration. The values of bubble mass center fluctuations are $(\Delta x_c, \Delta y_c, \Delta z_c) = (17.28, 12.2, 33.83)$ cm. A comparison of Figures 14(C-a) and 14(C-b) for bubble mass center fluctuations driven by gravity gradient-dominated, and g-jitter-dominated accelerations, provides the following conclusions: (a) Torsional moment-and twisting force-equivalent gravity gradient-dominated acceleration exerted on the rotating dewar container produces smaller values of magnitudes and fluctuations of angular momentum and fluid moment than that driven by g-jitter-dominated acceleration. (b) Dynamics of bubble (liquid-vapor interface) driven by torsional moment-and-twisting force-equivalent gravity gradient acceleration produces bubble mass center fluctuations of $\Delta x_c > \Delta y_c > \Delta z_c$ while up and down oscillations of bubble driven by g-jitter-dominated acceleration induces bubble center fluctuations of $\Delta z_c > \Delta x_c > \Delta y_c$. (c) A comparison of the values of bubble mass center fluctuations show that fluctuations of bubble mass center induced by g-jitter-dominated acceleration is

greater than that induced by gravity gradient-dominated acceleration. (d) Fluctuations of both x_c and y_c start from zero while that of the z_c starts from a non-zero value at the middle point of the height of partially filled liquid container. (e) Fluctuation magnitudes of x_c, y_c and z_c associated with higher frequency jitter are lower than those of the frequencies associated with lower jitter frequency for bubble mass center fluctuations driven by g-jitter-dominated acceleration.

Figure 17(A) shows the computed time variation of the fluctuations of slosh reaction forces exerted on the dewar container driven by g-jitter-dominated acceleration with frequency of 0.1 Hz. The values of slosh reaction force fluctuations are $(\Delta F_x, \Delta F_y, \Delta F_z) = (383.0, 315.5, 619.7)$ dynes and the maximum values of slosh reaction force are Max $(|F_x|, |F_y|, |F_z|) = (192.2, 172.3, 359.5)$ dynes. It shows $\Delta F_x > \Delta F_y > \Delta F_z$ and $|F_x| > |F_y| > |F_z|$. Comparison of input and response of forces between Figures 14(B) and 17(A) show that these two sets of curves are very much similar in characteristics and trends with smaller amplitudes and fluctuations shown in the response curve. In other words, it indicates that the fluid system, with modulation of sloshing dynamics, acts as a damping machine in input and response circuit. Comparison between Figures 16(A) and 17(A) for slosh reaction force fluctuations driven by gravity gradient-dominated acceleration and g-jitter-dominated acceleration show that gravity jitter-dominated acceleration are responsible for the excitation of greater values and magnitudes than that driven by gravity gradient-dominated acceleration.

Figures 17(B-a), 17(B-b), and 17(B-c) show variations of slosh reaction torque exerted on the container wall due to bubble deformations excited by g-jitter-dominated acceleration with frequency of 0.1 H along t ex, y, and z axes, respectively. The values of slosh reaction torque fluctuations are $(\Delta M_x, \Delta M_y, \Delta M_z) = (1612.2, 1957.9, 0.10)$ dyne•cm and the maximum absolute values of slosh

reaction torque are Max ($|M_x|$, $|M_y|$, $|M_z|$) = (1013.7, 1139.3, 0.52) dyne•cm. It shows $\Delta M_y > \Delta M_x > \Delta M_z$ and $|M_y| > |M_x| > |M_z|$. Characteristics of the fluctuations of slosh reaction torques driven by g-jitter-dominated acceleration are similar to that drawn for the fluctuations of slosh reaction torque driven by g-jitter-dominated acceleration. However, g-jitter-dominated acceleration excited values and fluctuations of slosh reaction torque exerted on the dewar container have a greater value and magnitude than that driven by gravity gradient-dominated acceleration.

Figure 17(C) shows time fluctuations of moment arm of slosh reaction torque exerted on the dewar container due to bubble deformations excited by asymmetric g-jitter-dominated acceleration. The values of moment arm fluctuations are (ΔL_x, ΔL_y, ΔL_z) = (4.6, 3.9, 5.3) cm. The maximum absolute values of moment arm are Max ($|L_x|$, $|L_y|$, $|L_z|$) = (2.4, 3.3, 77.8) cm. It shows $\Delta L_z > \Delta L_y > \Delta L_x$ and $|L_z| > |L_y| > |L_x|$. Comparison of gravity gradient-dominated and g-jitter dominated accelerations driven fluctuations provide the following conclusions: (a) Torsional moment-and twisting force-equivalent gravity gradient-dominated acceleration exerted on the rotating dewar container produces smaller maximum values and fluctuations of slosh reaction forces and torques than that driven by g-jitter-dominated acceleration. (b) Dynamics of bubble (liquid-vapor interface) driven by torsional moment-and twisting force-equivalent gravity gradient-dominated acceleration produces greater fluctuations and magnitude of slosh reaction moment arm than that produced by up and down oscillations of bubble driven by g-jitter-dominated acceleration. (c) Input and response relation between combined gravity gradient/g-jitter accelerations and slosh reaction forces acting on the dewar container through the modulation of sloshing dynamics show that the characteristics and trends are similar. However, the fluid system acts a damper which, in a realistical sense, helps damping out the spacecraft acceleration activated by the orbital forces[42-45].

X Discussion and Conclusions

Mathematical formulations of the possible accelerations which may exert on the fluid systems of spacecraft in microgravity have been reviewed. Dynamics of non-inertial frame fluid systems governing equations subject to initial and boundary conditions applicable to bubble dynamics in microgravity have been discussed. Bubble deformations and oscillations driven by (a) Spin-up from rest with and without a completion of wrapping around the dewar well, (b) Spin-down from complete wrapping of rotating dewar with steady state, (cc) rotating bubble subject to various magnitudes of gravity gradient and g-jitter accelerations associated with slew motion, (e) bubble deformations driven by orbital accelerations in rotating dewar with and without baffle, and (f) rotating bubble subject to lateral and axial impulses, have been reviewed and discussed.

Bubble mass center fluctuations due to bubble deformations and oscillations driven by various magnitudes of orbital accelerations have caused major problems in spacecraft orbital and attitude controls[34,47]. This problem has been discussed precisely in this review.

Slosh reaction forces and torques fluctuations acting on the dewar due to bubble deformations and oscillations driven by the orbital accelerations have been another source of problems induced in spacecraft controls[34,47]. Precise mathematical formulations of the computations of these slosh reaction and torques have been discussed. Accurate computation and prediction of these slosh reaction forces and torques are essential for the development of orbital and attitude control techniques of spacecraft[34,47].

Similarity rules have been used widely in the prediction of bubble oscillations in dewar container with different geometry and various physical parameters. With help of Hung et al[37], we can extent the discussion covered in this review to various cases with different geometry.

For the purpose to truly validate computation code developed, it is

urgently needed to carry out sloshing experiment in microgravity, in time evolution of both bubble deformation and slosh reaction forces and torque. Computational programs developed for slosh dynamics so far is quite complicated and is not user friendly. It is suggest to spend more effort in developing numerically efficient computational code to be used for future spacecraft real time operation.

References

1. Forward, R. L., Flattening Space-Time Near the Earth, Physical Review, Series D, Vol. 26, pp. 735-744, 1982.

2. Misner, C. W., Thorne, K. S., and Wheeler, J. A., Gravitation, W. H. Freeman Co., San Francisco, CA, pp. 1-1279, 1973.

3. Weinberg, S., Gravitation and Cosmology - Principles and Applications of General Relativity, pp. 657, John Wiley and Sons, New York, 1972.

4. Avduyevsky, V. S. (editor), Scientific Foundations of Space Manufacturing, MIR, Moscow, USSR, 1984.

5. Kamotani, Y., Prasad, A., and Oastrach, S., Thermal Convections in an Enclosure Due to Vibrations Aboard a Spacecraft, AIAA Journal, Vol. 19, pp. 511-516, 1981.

6. Hung, R. J., Tsao, Y. D., Hong, B. B., and Leslie, F. W., Dynamical Behavior of Surface Tension on Rotating Fluids in Low and Microgravity Environments, International Journal for Microgravity Research and Applications, Vol. 11, pp. 81-95, 1989a.

7. Hung, R. J., Tsao, Y. D., Hong, B. B., and Leslie, F. W., Axisymmetric Bubble Profiles in a Slowly Rotating Helium Dewar Under Low and Microgravity Environments, Acta Astronautica, Vol. 19, pp. 411-426, 1989b.

8. Hung, R. J., Tsao, Y. D., Hong, B. B., and Leslie, F. W., Bubble Behaviors in a Slowly Rotating Helium Dewar in Gravity Probe-B Spacecraft Experiment, Journal of Spacecraft and Rockets, Vol. 26, pp. 167-172, 1989c.

9. Hung, R. J., Shyu, K. L., and Lee, C. C., Liquid Hydrogen Slosh Wave Excited by Constant Reverse Gravity Acceleration of Geyser Initiation, Journal of Spacecraft and Rockets, Vol. 29, pp. 523-528, 1992b.

10. Hung, R. J., Shyu, K. L., and Lee, C. C., Medium Frequency Impulsive Thrust Excited Slosh Waves During Propellant Reorientation with Geyser, Journal of Propulsion and Power, Vol. 8, pp. 778-785, 1992a.

11. Hung, R. J., Shyu, K. L., and Lee, C. C., (1991) Slosh Wave Excitation Associated with High Frequency Impulsive Thrust Reverse Gravity Acceleration of Geyser Initiation, Microgravity Quarterly, 1, 125-133.

12. Hung, R. J., and Lee, C.C., (1994) Dynamic Characteristics of the Partially Filled Rotating Dewar of the Gravity Probe-B Spacecraft, Acta Astronautica, 32, 199-209.

13. Hung, R. J., and Shyu, K. L., (1992) Medium Frequency Impulsive Thrust Activated Liquid Hydrogen Reorientation with Geyser, Journal of Propulsion and Power, 8, 987-994.

14. Hung, R. J., and Shyu, K. L., (1992) Excitation of Slosh Waves Associated with Low Frequency Impulsive Reverse Gravity Acceleration of Geyser Initiation, Acta Astronautica, 26, 425-433.

15. Hung, R. J., and Shyu, K. L., (1992) Constant Reverse Thrust Activated Reorientation of Liquid Hydrogen with Geyser Initiation, Journal of Spacecraft and Rockets, 29, 279-285.

16. Hung, R. J., and Shyu, K. L., (1991) Space-Based Cryogenic Liquid Hydrogen Reorientation Activated by Low Frequency Impulsive Reverse Gravity Thruster of Geyser Initiation, Acta Astronautica, 25, 709-719.

17. Hung, R.J., Tsao, Y.D., and Leslie, F.W., (1990) Effect of G-Jitters on Stability of Rotating Bubble Under Microgravity Environment, Acta Astronautica, 21, 309-321.

18. Hung, R. J., and Shyu, K. L., (1991) Cryogenic Liquid Hydrogen Reorientation Activated by High Frequency Impulsive Reverse Gravity Acceleration of Geyser Initiation, Microgravity Quarterly, 1(2), 81-92.

19. Hung, R. J., Lee, C. C., and Shyu, K. L., (1991) Reorientation of Rotating Fluid in Microgravity Environment With and Without Gravity Jitters, Journal of Spacecraft and Rockets, 28, 71-79.

20. Hung, R. J., and Leslie, F. W., (1988) Bubble Shapes in a Liquid-Filling Rotating Container Under Low Gravity, Journal of Spacecraft and Rockets, 25, 70-74.

21. Leslie, F.W., (1985) Measurements of Rotating Bubble Shapes in a Low Gravity Environment, Journal of Fluid Mechanics, 161, 269-275.

22. Mason, P., Collins, D., Yang, L., Edeskuty, F., Schuch, A., and Williamson, K., (1978) The Behavior of Superfluid Helium in Zero Gravity, Proceedings 7th International Cryogenic Engineering Conferences, Surrey, England, Science and Technology Press.

23. Van Sciver, S.W., (1986) Helium Cryogenics, Plenium Press, New York.

24. Donnelley, R.J., (1991) Quantized Vortices in Helium II, Cambridge University Press, Cambridge.

25. Hung, R.J., Pan, H.L., and Long, Y.T. (1994) Peculiar Behavior of Helium II Disturbances Due to Sloshing Dynamics Driven by Jitter Accelerations Associated with Slew Motion in Microgravity. Cryogenics, 34, 641-648.

26. Hochstein, J.I., Aydelott, J.C., Mjolsness, R.C., and Torrey, M.D., (1994) On Orbit Propellant Motion Resulting from an Impulsive Acceleration, Journal of Propulsion and Power, 10, 653-660.

27. Hung, R.J., and Shyu, K.L., (1994) Liquid Hydrogen Shut-Off Geyser Excitation Induced by Sloshing Dynamics During Draining in Microgravity, Aeronautical Journal (Royal Aeronautical Society of United Kingdom), 98, 237-250.

28. Bauer, H.F., (1991) Liquid Sloshing Response in Spin-Stabilized Missiles or Satellites Due to Axial Excitation, Zeitscrift Fur Flugwissenschaften und Weltraumforschung, 15, 225-256.

29. Baner, H.F. (1991) Liquid Sloshing Response in a Spinning Container due to Pitching Excitation, Zeitscrift Fur Flugwissenschaften und Weltraumforschung, 15, 386-392.

30. Hoare, F.E., Jackson, L.C., and Kurti, N. (1961) Experimental Cryogenics;

Liquid Helium II, Butterworths, London, U.K.

31. Wilks, J., (1967) The Properties of Liquid and Solid Helium, Clarendon Press, Oxford, U.K.

32. Hung, R.J., Lee, C.C., and Leslie, F.W., (1991) Slosh Wave Excitation in a Partially Filled Rotating Tank Due to Gravity Jitters in a Microgravity Environment, Acta Astronautica, 25, 523-551.

33. Hung, R.J., Lee, C.C., and Leslie, F.W., (1991) Response of Gravity Level Fluctuations on the Gravity Probe-B Spacecraft Propellant System, Journal of Propulsion and Power, 7, 556-564.

34. Hung, R.J., Lee, C.C., and Leslie, F.W., (1992) Spacecraft Dynamical Distribution of Fluid Stresses Activated by Gravity Jitter Induced Slosh Waves, Journal of Guidance, Control and Dynamics, 15, 817-824.

35. Hung, R.J., and Pan, H.L., (1994) Gravity Gradient or Gravity Jitter Induced Viscous Stress and Moment Fluctuations in Microgravity, Fluid Dynamics Research, 14, 29-51.

36. Sussman, M., Smereka, P., and Osher, S., (1994) A Level Set of Computing Solutions to Incompressible Two-Phase Flow, Journal of Computational Physics, 114, 146-159.

37. Hung, R.J., Lee, C.C., and Leslie, F.W., (1993) Similarity Rules in Gravity-Jitter Related Spacecraft Liquid Propellant Slosh Waves Excitation, Journal of Fluids and Structures, 6, 493-522.

38. Hung, R.J., Lee, C.C., and Leslie, F.W., (1993) Effect of the Baffle on the Spacecraft Fluid Propellant Viscous Stress and Moment Fluctuations, Transaction of the Japan Society for Aeronautical and Space Sciences, 35, 187-207.

39. Hung, R.J., Lee, C.C., and Leslie, F.W., (1993) Effect of the Baffle on the Asymmetric Gravity-Jitter Excited Slosh Waves and Spacecraft Moment and Angular Momentum Fluctuations, Journal of Aerospace Engineering, 207 (United

Kingdom), 105-120.

40. Landau. L.D., and Lifshitz, (1959) Fluid Mechanics, Pergamon Press, London, 1-656.

41. Hung, R.J., and Pan, H.L., (1993) Asymmetric Slosh Wave Excitation in Liquid-Vapor Interface Under Microgravity, Acta Mechanica Sinica, 9, 298-311.

42. Harlow, F. H., Welch, F. E., (1965) Numerical Calculation of Time-Dependent Viscous Incompressible Flow of Fluid with Free Surface, Physics of Fluids, 8, 2182-2189.

43. Hirt, C. W., Nichols, B. D., (1981) Volume of Fluid (VOF) Method for the Dynamics of Free Boundaries, Journal of Computational Physics, 39, 201-225.

44. Salvadori, M. G., Baron, M. L., (1961) Numerical Methods in Engineering, Prentice-Hall, Inc., Englewood Cliffs, NJ.

45. Hageman, L. A., Young, D. M., (1981) Applied Iterative Methods, Academic Press, New York.

46. Young, D., (1954) Iterative Methods for Solving Partial Difference Equations of Elliptical Type, Transactions of American Mathematical Society, 76, 92-111.

47. Hung, R.J., and Pan, H.L., (1995) Fluid Force Activated Spacecraft Dynamics Driven by Gravity Gradient and Jitter Accelerations, Journal of Guidance, Control and Dynamics, 18, in press.

48. Hung, R.J., and Pan, H.L., (1995) Sloshing Dynamics Induced Angular Momentum Fluctuations Driven by Orbital Gravity Gradient and Jitter Accelerations in Microgravity, Applied Scientific Research Journal (International Journal of the Application of Fluid Dynamics), 54, 51-68.

49. Hung, R.J., and Pan, H.L., (1994) Simulation of Sloshing Dynamics Induced Forces and Torques Actuated on Dewar Container Driven by Gravity Gradient and Jitter Accelerations in Microgravity, Journal of Simulation Practice and Theory, 2, 91-120.

50. Hung, R.J., and Long, Y.T., (1995) Response and Decay of Rotating Cryogenic Liquid Helium Reacted to Impulsive Accelerations in Microgravity. Transaction of Japan Society for Aeronautical and Space Sciences, 37, 291-310.

51. Hung, R.J., and Pan, H.L., (1995) Rotational Speed and Wrapping of Different Size Cryogenic Helium Bubbles Around a Dewar Well in Microgravity, Aeronautical Journal (Royal Aeronautical Society of the United Kingdom), in press.

52. Hung, R.J., and Pan, H.L., (1995) Rotational Speed Spin-Down and Unwrapping of Various Size Symmetric Cryogenic Helium Bubbles Around Dewar Well in Microgravity. Transactions of the Japan Society for Aeronautical and Space Sciences, 37, in press.

53. Greenspan H.P., (1968) The Theory of Rotating Fluids, Cambridge University Press, Cambridge, UK, pp. 327.

54. Hung, R.J., and Long, Y.T., (1995) Response and Decay of Rotating Cryogenic Liquid Helium Reacted to Impulsive Acceleration in Microgravity, Transactions of Japan Society for Aeronautical and Space Sciences, 37, 287-307.

55. Hung, R.J., and Long, Y.T., (1995) Effect of Baffle on Slosh Reaction Forces in Rotating Liquid Helium Subjected to a Lateral Impulse in Microgravity, Cryogenics, 35, in press.

56. Hung, R.J., and Pan, H.L., (1993) Differences in Gravity Gradient and Gravity Jitter-Excited Slosh Waves in Microgravity, Transaction of the Japan Society for Aeronautical and Space Sciences, 36, 153-169.

57. Hung, R.J., Long, Y.T., and Pan, H.L., (1994) Sloshing Dynamics Induced Angular Momentum Fluctuations Driven by Jitter Accelerations Associated with Slew Motion in Microgravity, Transactions of the Japan Society for Aeronautical and Space Sciences, 37, 217-234.

58. Hung, R.J., and Pan, H.L., (1995) Sloshing Modulated Liquid-Vapor Interface Fluctuations Activated by Orbital Accelerations Associated with Spinning

and/or Slew Motions, Journal of Colloid and Interface Science, 170, 538–549.

59. Hung, R.J., and Pan, H.L., (1995) Orbital Spacecraft Cryogenic Helium Dewar Sloshing Dynamics Driven by Gravity Gradient Acceleration Associated with Slew Motion, Japan Society of Mechanical Engineers International Journal/Fluid and Thermal Engineering, in press.

60. Hung, R.J., and Lee, C.C., (1994) Effect of a Baffle on Slosh Waves Excited by Acceleration in Microgravity, Journal of Spacecraft and Rockets, 31, 1107–1114.

61. Hung, R.J., and Lee, C.C., (1995) Effect of Baffles on Sloshing Modulated Fluid Force and Torque Fluctuations on the Dewar Driven by Gravity Gradient Acceleration in Microgravity, Applied Scientific Research Journal, (International Journal of the Application of Fluid Dynamics), 54, 69–94.

62. Hung, R.J., and Pan, H.L., (1995) Effect of baffle on Sloshing Modulated Torques Responded to Orbital Accelerations in Microgravity, Journal of Spacecraft and Rockets, 31, in press.

63. Hung, R.J., and Lee, C.C., (1995) Effect of Baffle on Gravity Gradient Acceleration Excited Slosh Waves and Associated Viscous Stress Force Activated Spacecraft Dynamic Fluctuations, Aeronautical Journal (Royal Aeronautical Society of United Kingdom), in press.

64. Hung, R.J., Lee, C.C., and Leslie, F.W., (1994) Dynamic Characteristics of the Partially Filled Rotating Dewar of the Gravity Probe-B Spacecraft, Acta Astronautica, 32 (3), 199–209.

65. Hung, R.J., Pan, H.L., and Leslie, F.W., (1994) Fluid Systems Angular Momentum and Moment Fluctuations Driven by Gravity Gradient or Gravity Jitter in Microgravity, Journal of Flight Sciences and Space Research (Zeitschrift fur Flugwissenschaften und Weltraumforschung), 18, 195–202.

66. Hung, R.J., and Pan, H.L., (1994) Numerical Modeling of Bubble Oscillations in Microgravity, Scientific Computing and Automation, 10 (6), 21–25.

67. Hung, R.J., and Shyu, K.L., (1994) Liquid Hydrogen Suction Dip and Slosh Wave Excitation During Draining Under Normal and Reduced Gravity Environments, Transactions of the Japan Society for Aeronautical and Space Sciences, 36, 225-248.

68. Hung, R.J., Pan, H.L., and Long, Y.T., (1994) Sloshing Dynamics Modulated Cryogenic Helium Fluids Driven by Gravity Gradient or Jitter Accelerations Associated With Slew Motion in Microgravity, Acta Mechanica Sinica, 10, 367-381.

69. Hung, R.J., and Lee, C.C., (1994) Effect of Baffles on Imbalance Bubble Configuration Due to Sloshing Dynamics Driven by Gravity Gradient Acceleration in Microgravity, Canadian Aeronautics and Space Journal, 40, 185-202.

Figure Captions

Figure 1 AXAF-S spacecraft coordinate systems with azimuth angle ψ_E from spacecraft mass center to the center of the Earth. Coordinate (x", y", z") for slew motion and coordinate (x, y, z) for fluid mechanics computation.

Figure 2 Computational algorithm for sloshing dynamics.

Figure 3 (A) Time sequence evolution of three-dimensional cryogenic helium II bubble fluctuations for spin-up rotating dewar. Liquid filled level=95%, ω = 0.4 rpm, and We = 226.62. (B) Various equilibrium profiles of horizontal cross section at height z=72.5 cm.

Figure 4 Time sequence evolution of cryogenic helium II bubble mass center fluctuations for spin-up rotating dewar with and without completion of bubble wrapping around dewar well.

Figure 5 Final equilibrium bubble profiles in r-z plane and θ = 0° and 180°, in r-θ plane at height z = 72.5 cm and in three-dimensional with liquid level of 85% (A) ω = 0.15 rpm, We = 31.87, t = 480 s, (B) ω = 0.05 rpm, We = 3.54, t = 1600 s.

Figure 6 (A) Three-dimensional configuration of container with baffle, (B) distribution of grid points in the radial-axial plane, and (C) in the radial-circumferential plane.

Figure 7 Time evolution of three-dimensional bubble oscillations for time between 225 and 427 s for rotating dewar in response to lateral impulse without and with baffle.

Figure 8 (A) Time sequence evolution of fluid mass center fluctuations in response to lateral impulse for container with and without baffle. (a) Fluid mass center fluctuations in x-axis, (b) Fluid mass center fluctuations in y-axis, and (c) Fluid mass center fluctuations in absolute values of radial direction. (B) Time sequence evolution of

fluid mass center fluctuations in response to axial impulse for container with and without baffle.

Figure 9 (A) Time variation of AXAF-S spacecraft gravity gradient acceleration acting on fluid mass located at (r, θ, z) = (12cm, $\pi/2$, 3 cm) for 90° slew motion in 600 s along the y"-axis and orbital period of 97.6 min. (B) Time variation of AXAF-S spacecraft jitter acceleration associated with slew motion acting on fluid mass located at (r, θ, z) = (12 cm, $\pi/2$, 3 cm) for 90° slew motion in 10 min. along the y"-axis and orbital period of 97.6 min.

Figure 10 (A) Time sequence evolution of three-dimensional bubble oscillations for dewar driven by gravity gradient acceleration associated with slew motion in the y"-axis. (B) Time sequence evolution of three-dimensional bubble oscillations for dewar driven by g-jitter acceleration associated with slew motion in the y"-axis. 90° slew motion in 600 s is applied to the spacecraft operation.

Figure 11 (A) Time sequence of the AXAF-S spacecraft fluid moment fluctuations due to sloshing dynamics driven by gravity gradient acceleration associated with slew motion in the y-axis. (B) Time sequences of the AXAF-S spacecraft bubble mass center fluctuations due to the sloshing dynamics driven by g-jitter acceleration associated with slew motion in the y-axis. 90° slew motion in 600 s is applied to spacecraft operation.

Figure 12 Time sequence of the fluctuations of (A) slosh reaction forces (B) slosh reaction moment, and (C) slosh reaction moment arm exerted on the dewar due to bubble deformations driven by gravity gradient acceleration associated with slew motion.

Figure 13 Time sequence of the fluctuations of (A) slosh reaction forces (B) slosh reaction moment, and (C) slosh reaction moment arm exerted on

the AXAF-S dewar due to sloshing dynamics driven by g-jitter acceleration associated with slew motion.

Figure 14 (A) Time variation of gravity gradient acceleration acting on fluid mass located at $(r,\theta,z)=(40\text{ cm}, \pi/4, 10\text{ cm})$ for turn-around period of 1200 s with rotating speed of 0.1 rpm. (B) Time variation of jitter acceleration acting on the fluid system under background gravity of 10^{-8} , 10^{-7} and 10^{-6} g_o, rotating speed of 0.1 rpm, turn-around period of 1200 s and jitter frequency of 0.1 Hz. (C) Time sequence of bubble mass center fluctuations caused by slosh wave excitation under gravity turn-around time of 1200 s rotation speed of 0.1 rpm.

Figure 15 Time sequence evolution of three-dimensional liquid-vapor interface oscillations for rotating dewar driven by (A) combined gravity gradient and jitter accelerations with magnitude of 10^{-8} g_o and (B) combined gravity gradient and jitter accelerations of 0.1 Hz frequency, and with magnitude of 10^{-6} g_o.

Figure 16 Time sequence of the fluctuations of (A) slosh reaction forces (B) slosh reaction moment and (C) slosh reaction moment arm exerted on the dewar container due to the bubble deformations driven by combined gravity gradient and g-jitter accelerations with 10^{-8} g_o under rotating speed of 0.1 rpm and gravity turn-around time of 1200 s.

Figure 17 Time sequence of the fluctuations of (A) slosh reaction forces (B) slosh reaction moment, and (C) slosh reaction moment arm exerted on the dewar due to the bubble deformations driven by combined gravity gradient and g-jitter accelerations with 10^{-7} g_o, rotating speed of 0.1 rpm, gravity turn-around time of 1200 s and jitter frequency of 0.1 Hz.

ON ORBIT COORDINATE SYSTEM

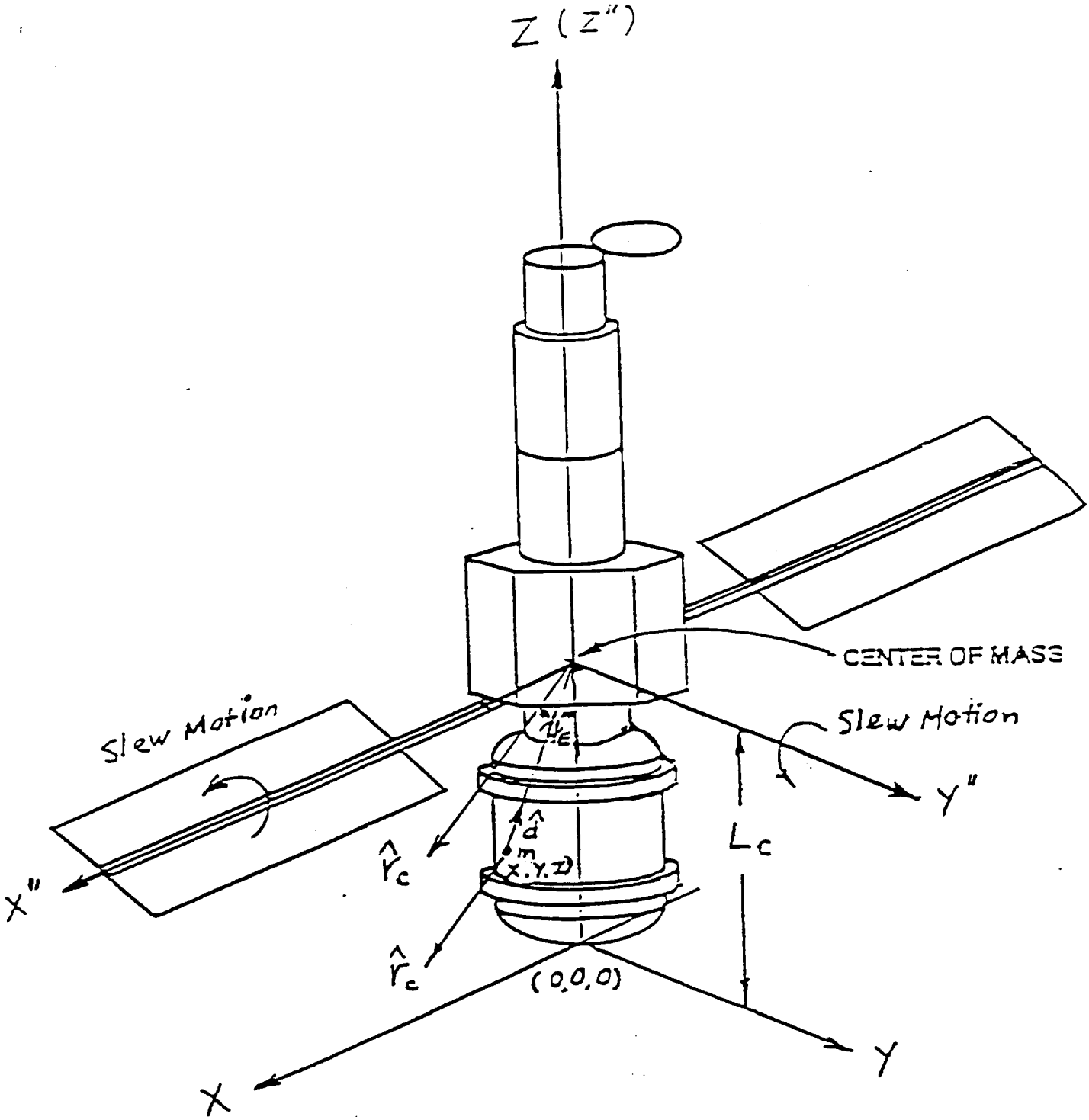

Figure 1

Computational Algorithm for Sloshing Dynamics

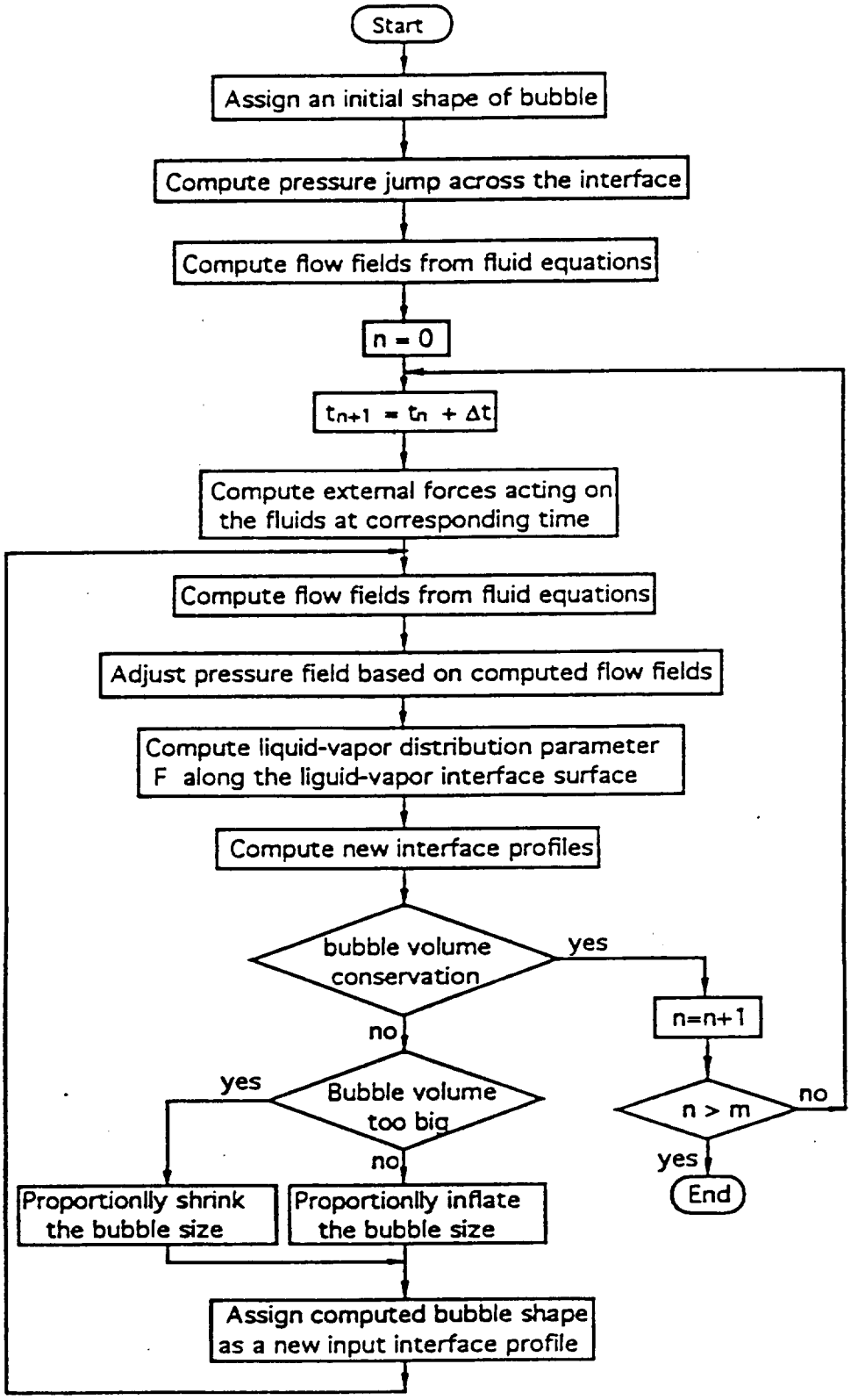

Fig. 2

(A) TIME EVOLUTION OF CRYOGENIC HELIUM BUBBLE SPIN-UP
Liquid Fill Level=95%, ω=0.4 rpm, We=226.62

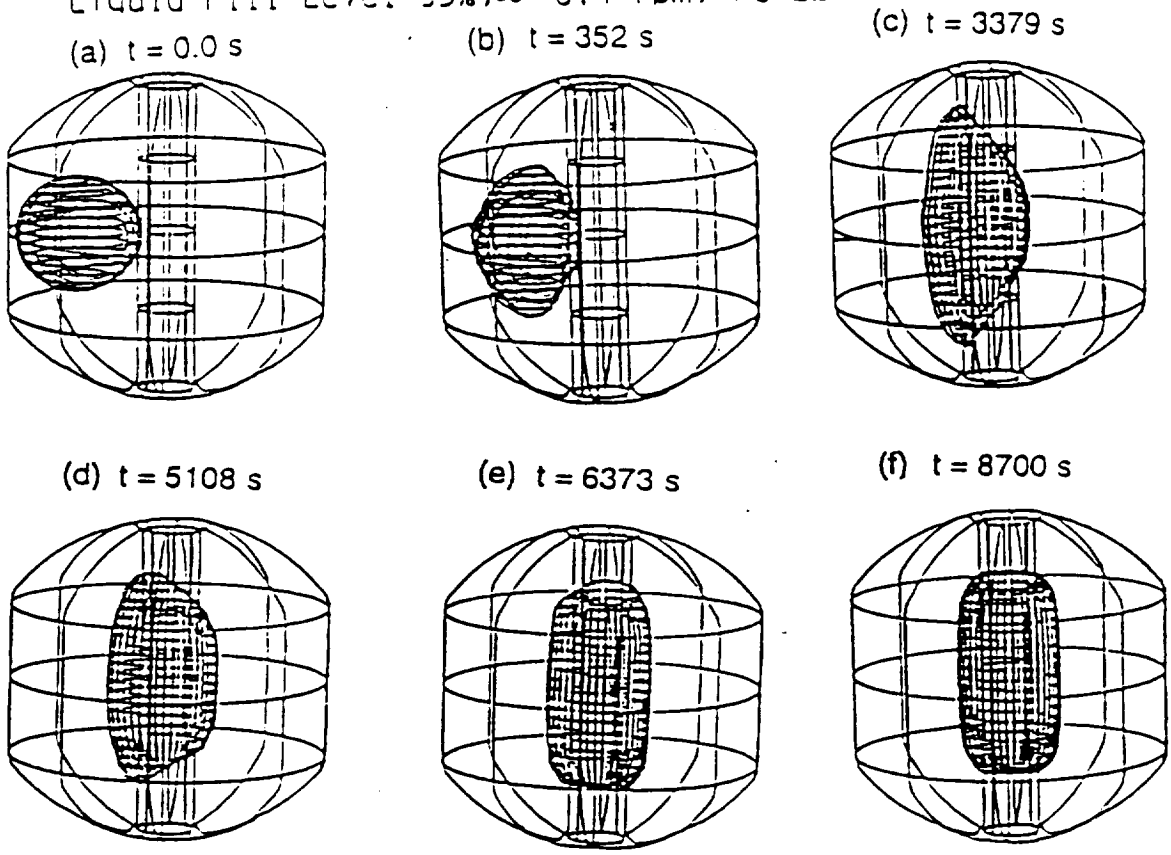

(B) FINAL EQUILIBRIUM BUBBLE PROFILES OF HORIZONTAL CROSS - SECTION AT HEIGHT Z = 72.5 CM WITH VARIOUS SPIN UP SPEEDS

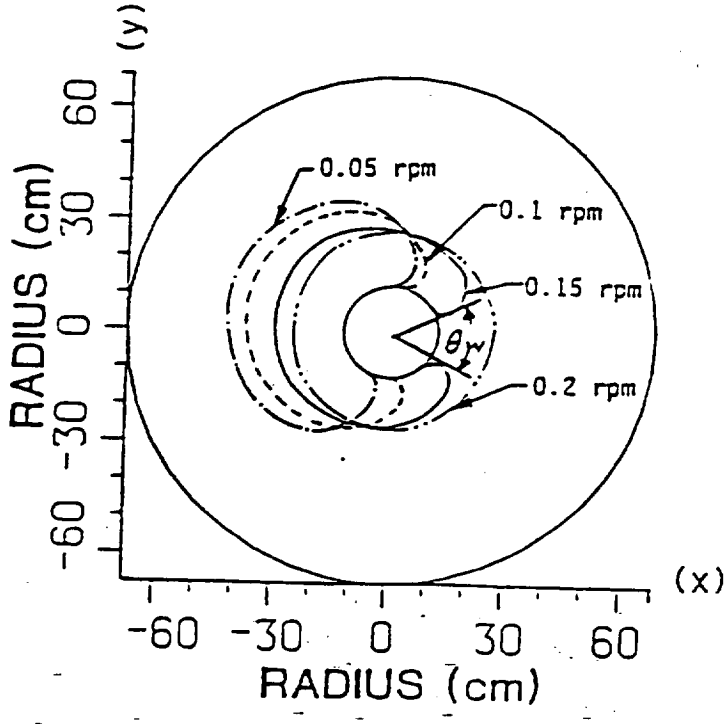

Fig. 3

BUBBLE MASS CENTER EVOLUTION DURING SPIN-UP WITH VARIOUS CONTAINER ROTATING SPEEDS

(A) ω = 0.4 rpm , We = 226.62

Liquid Fill Level=95%

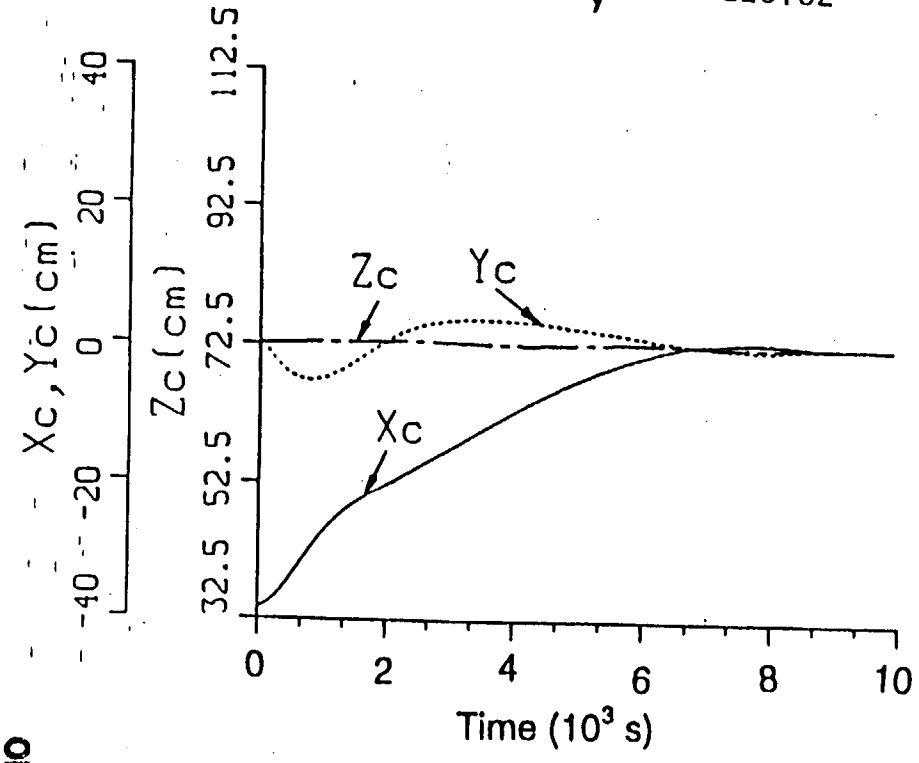

(B) ω =0.2 rpm, We=56.65

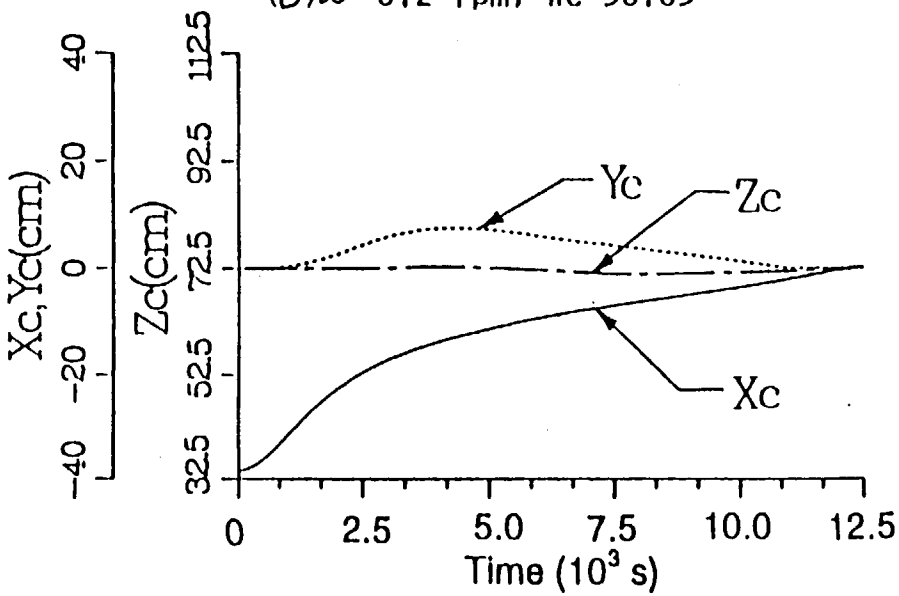

(C) ω=0.15 rpm, We=31.87

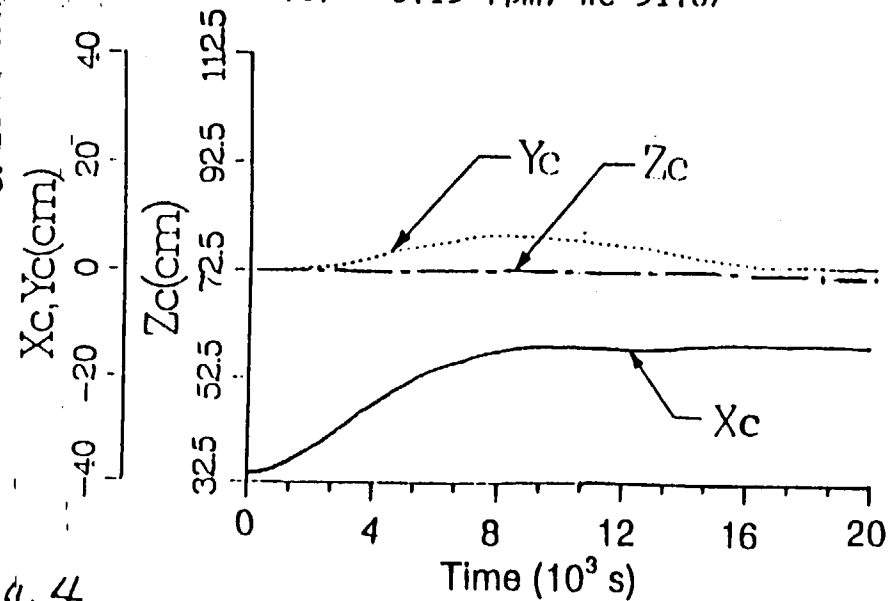

(D) ω =0.05 rpm, We=3.54

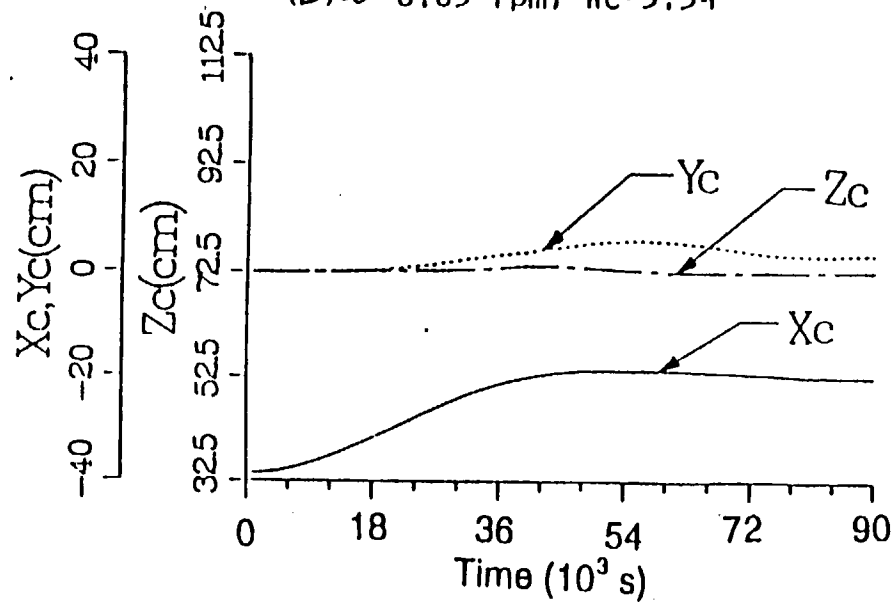

Fig. 4

TIME EVOLUTION CRYOGENIC HELIUM BUBBLE SPIN - DOWN

(A) Liquid Fill Level = 85%, ω = 0.15 rpm, W_e = 31.87

(a) t = 0.0 s

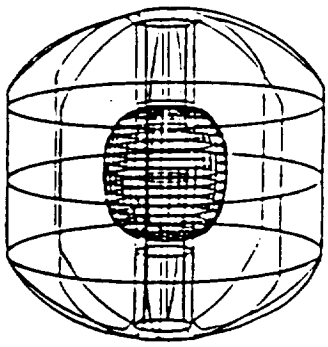

(b) t = 1750 s

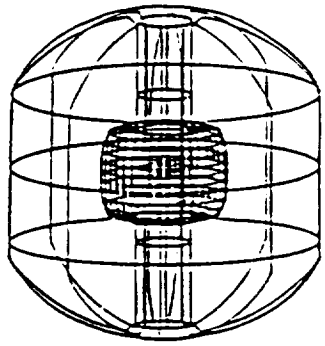

(c) t = 3325 s

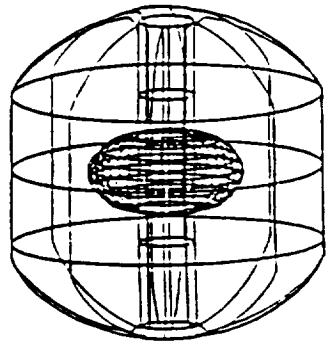

(d) t = 5460 s

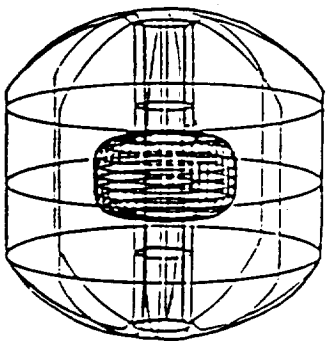

(e) t = 10500 s

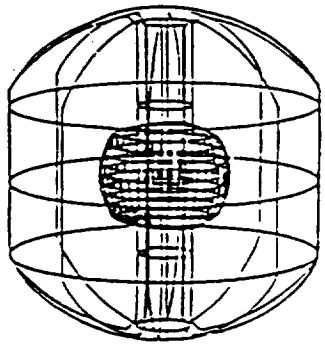

(f) t = 15800 s

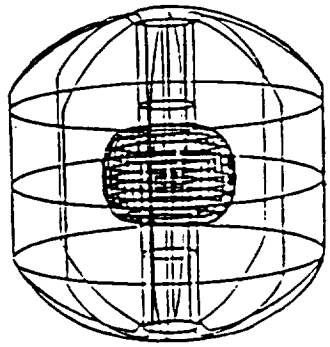

(B) Liquid Fill Level = 95%, ω = 0.05 rpm, W_e = 3.54

(a) t = 0.0 s

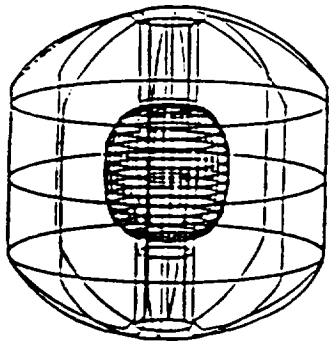

(b) t = 2350 s

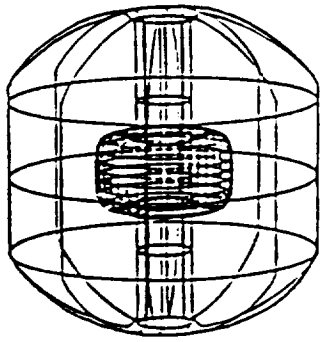

(c) t = 3500 s

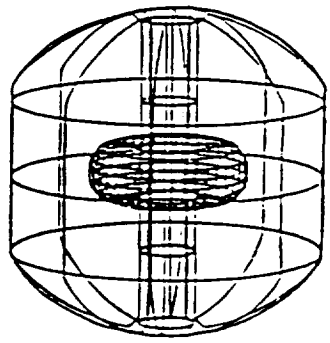

(d) t = 4200 s

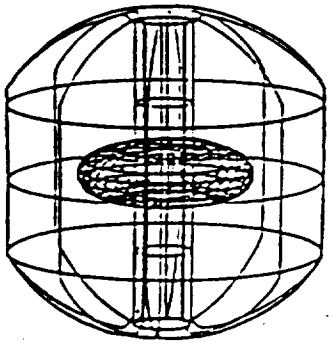

(e) t = 4650 s

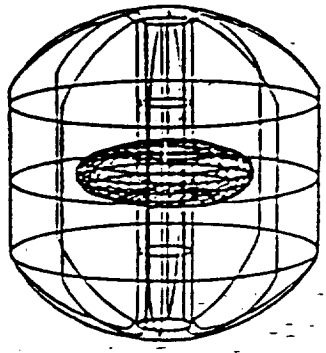

(f) t = 5500 s

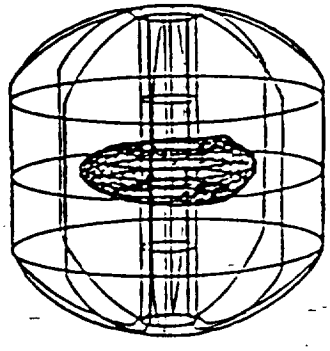

Fig. 5

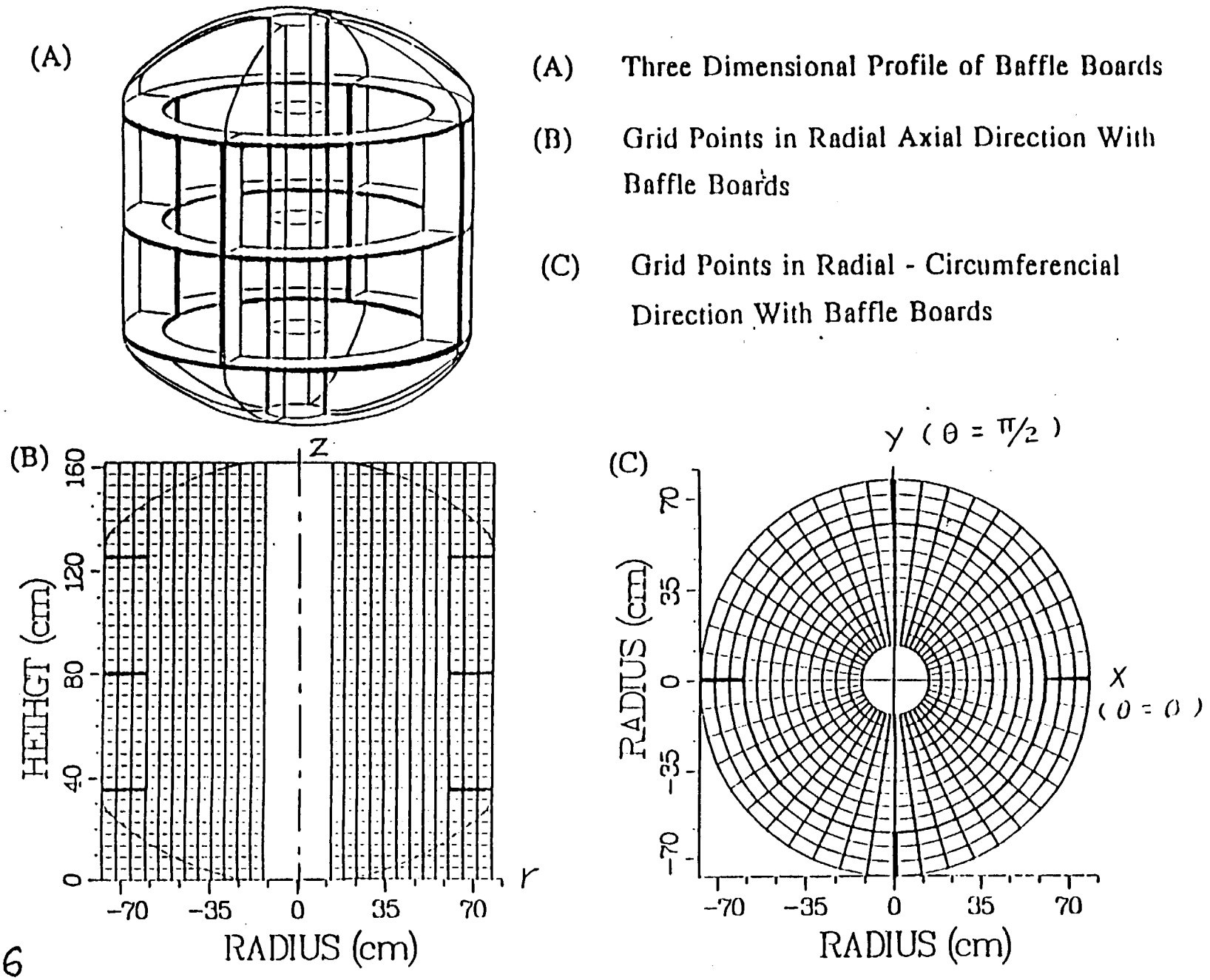

(A) Three Dimensional Profile of Baffle Boards

(B) Grid Points in Radial Axial Direction With Baffle Boards

(C) Grid Points in Radial - Circumferencial Direction With Baffle Boards

Fig. 6

Three Dimensional Bubble Finite Deformation

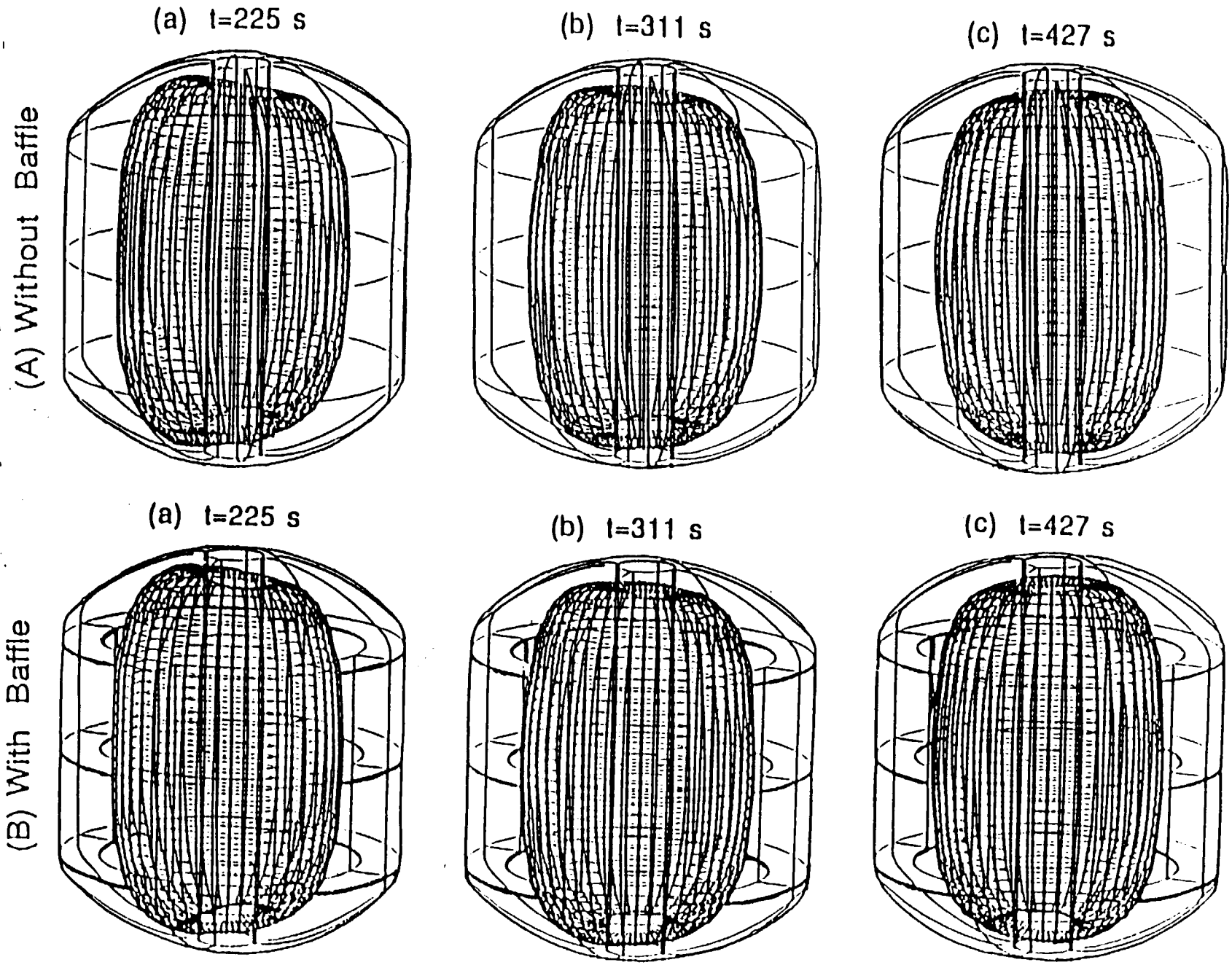

Fig. 7

(A) LATERAL IMPULSE RESPONSE

IMPULSE = $10^{-2}g_0$, in 10 msec

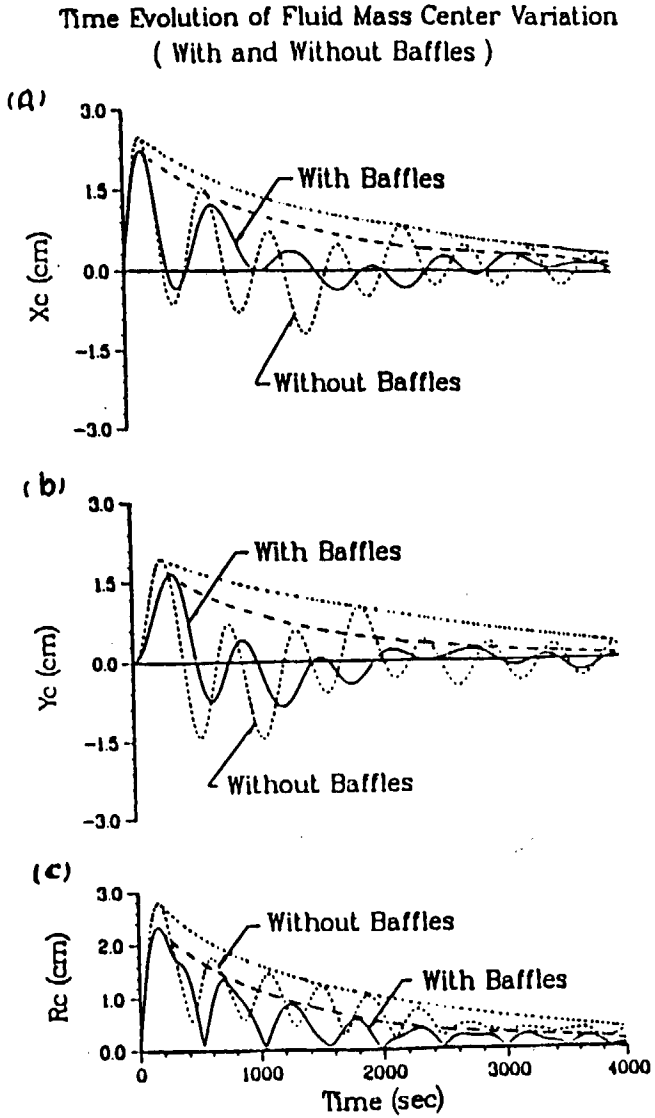

(B) AXIAL IMPULSE RESPONSE

IMPULSE = $10^{-2}g_0$, in 10 msec

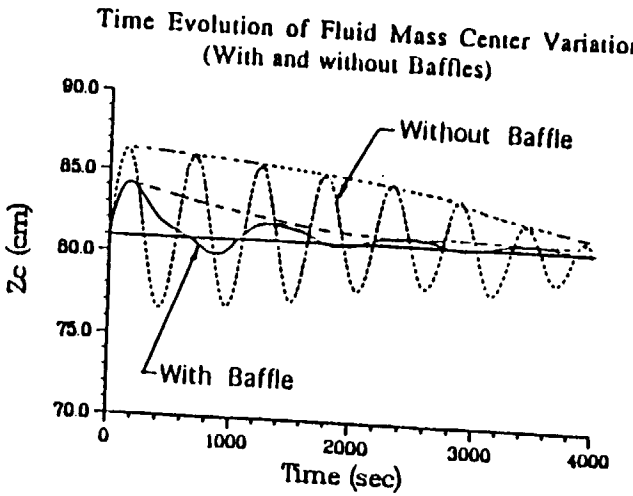

Fig. 8

AXAF-S

(A) Time Variation of Gravity Gradient Acceleration Associated With Slew Motion

(B) Time Variation of Force Acceleration Due to Slew Motion

at $(r, \theta, z) = (12\ \text{cm}, \pi/2, 3\ \text{cm})$

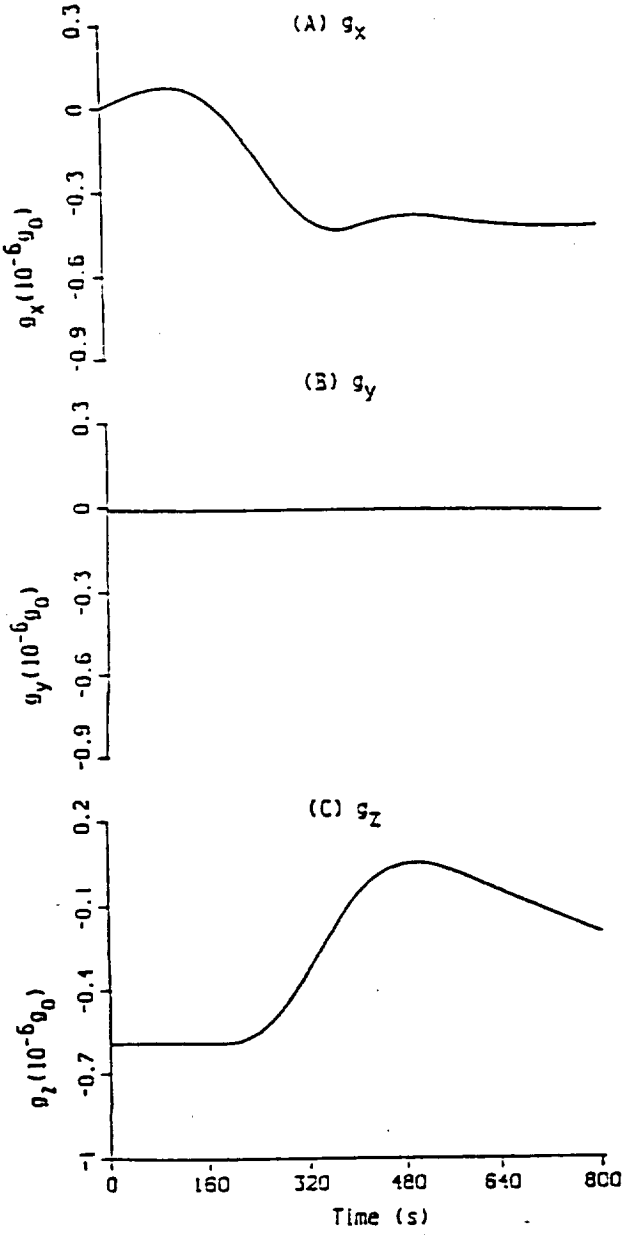

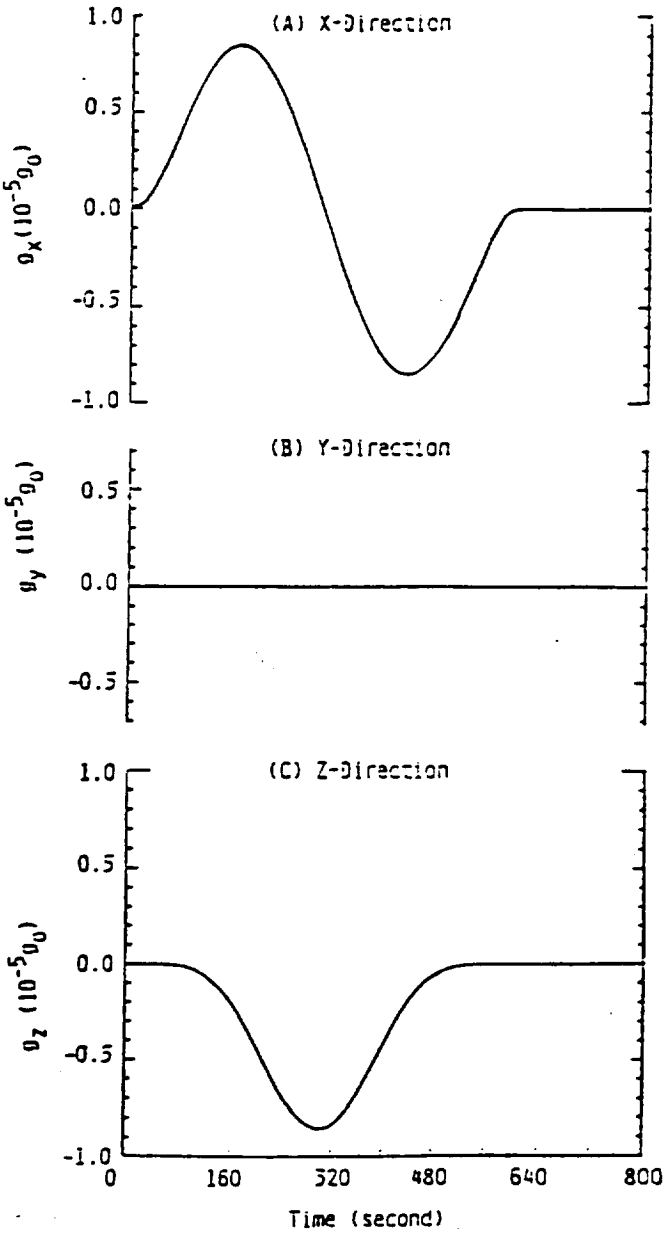

Fig. 9

SLOSHING DYNAMICS OF AXAF-S CRYOGENIC HELIUM II DEWAR

(A) Driven by Gravity Gradient Acceleration

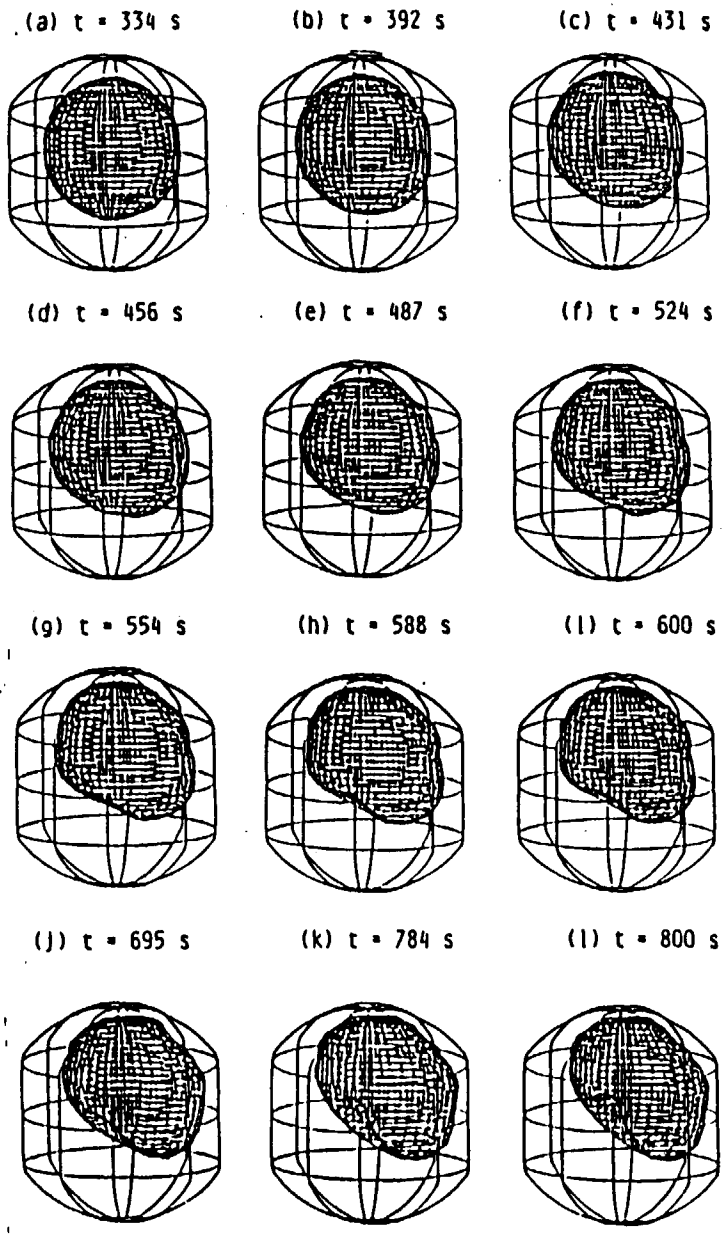

(B) JITTER ACCELERATION WITH SLEW MOTION

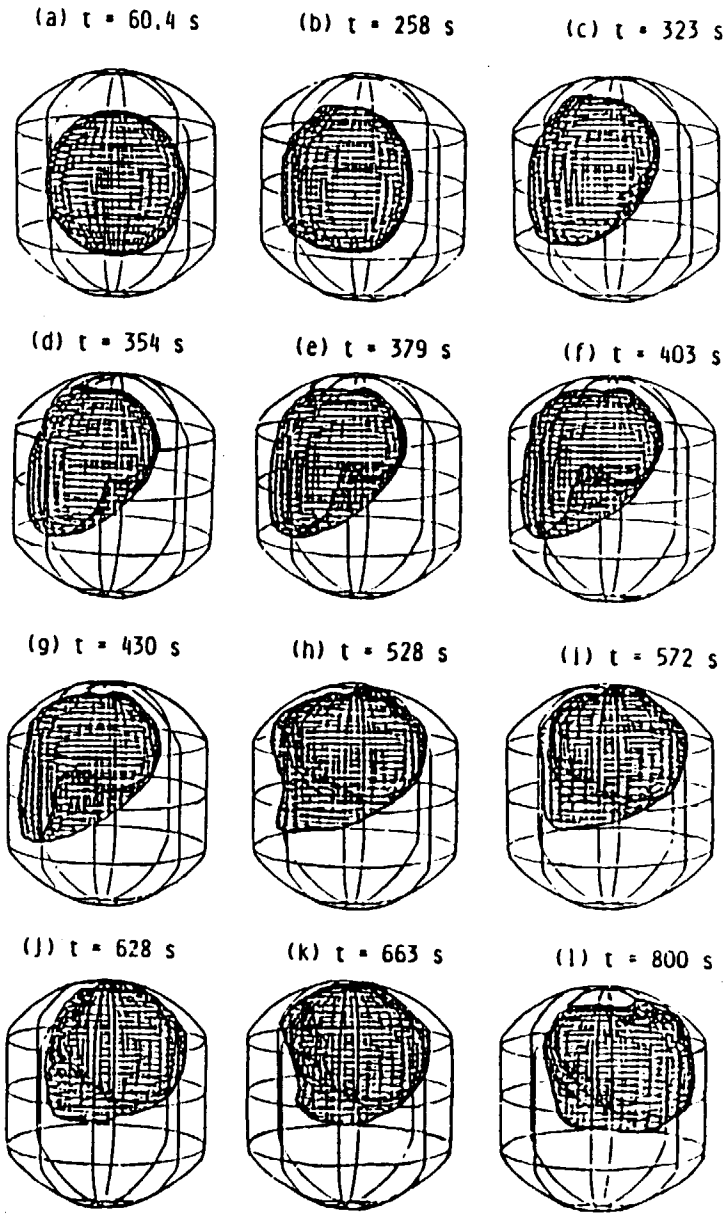

Liquid Filled Level = 70%

Fig 10

AXAF-S SPACECRAFT

VARIATIONS OF BUBBLE MASS CENTER (X_C, Y_C, Z_C)

(A) Driven by Gravity Gradient Acceleration Associated With Slew Motion

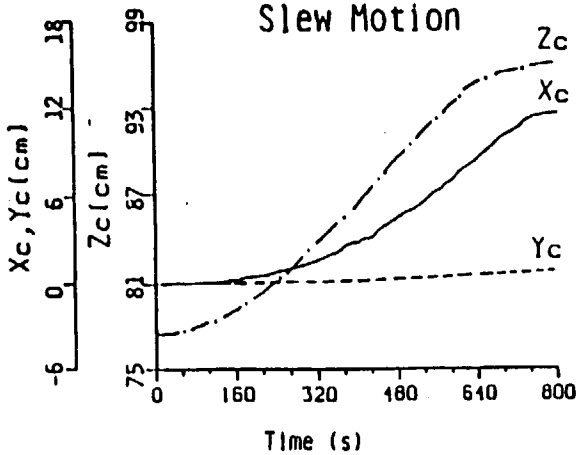

(B) DRIVEN BY JITTER ACCELERATION WITH SLEW MOTION

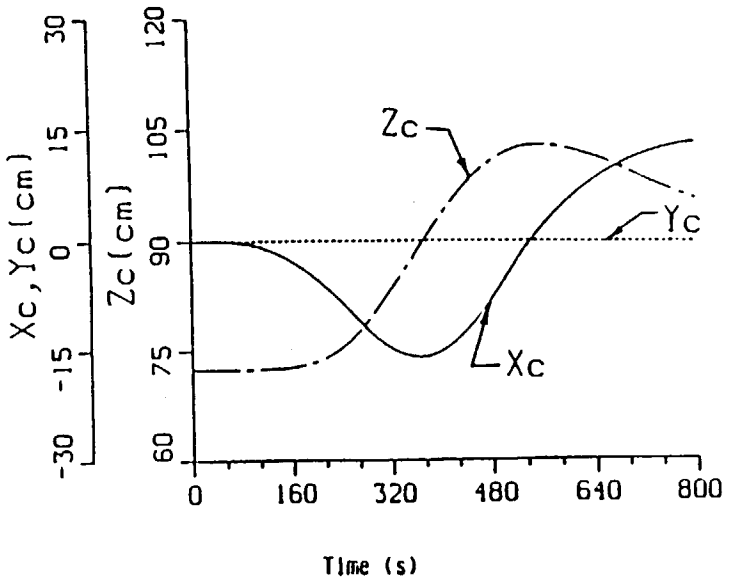

Fig. 11

AXAF-S

Driven by Gravity Gradient Acceleration Associated With Slew Motion

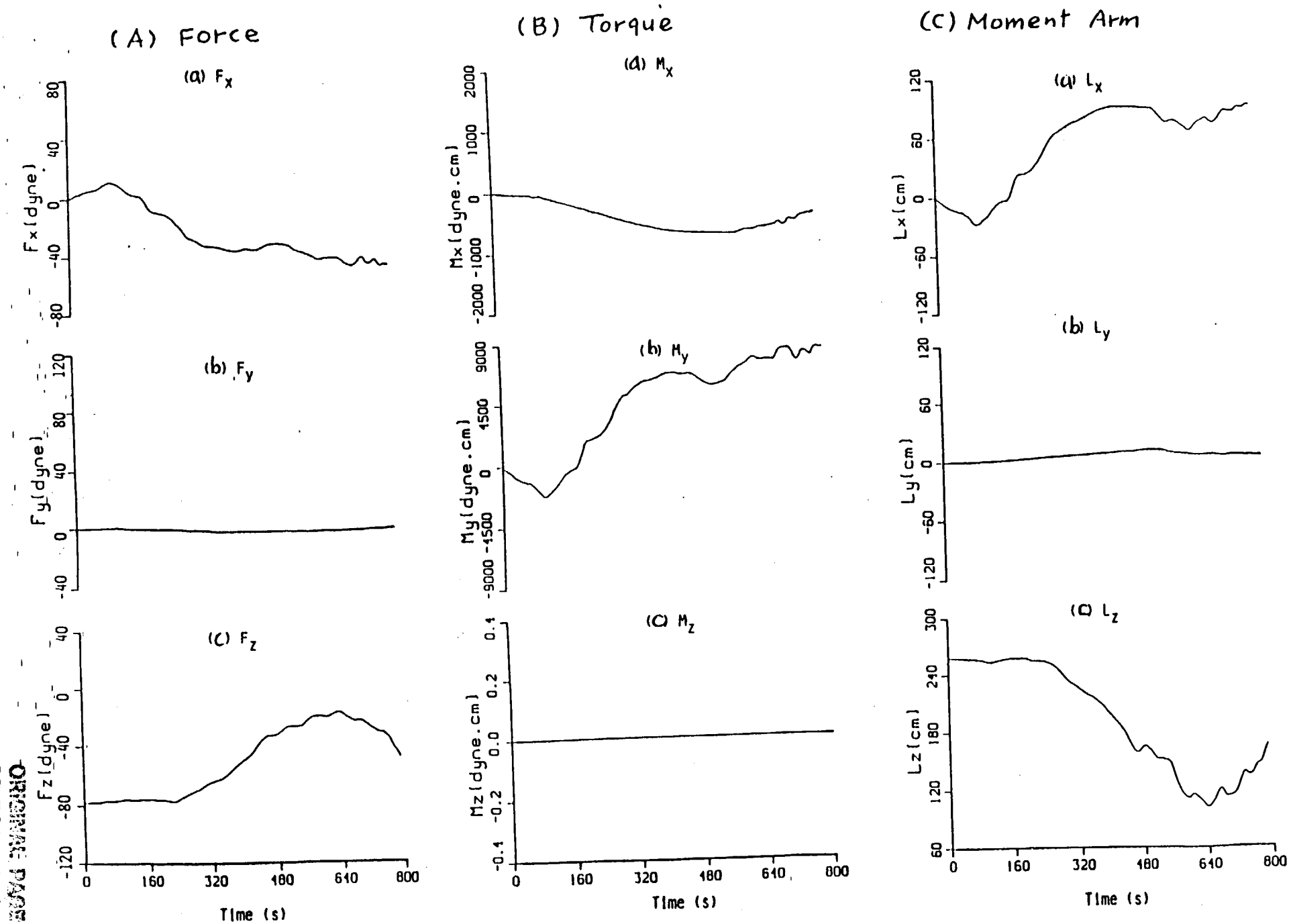

Fig 12

AXAF-S

DRIVEN BY JITTER ACCELERATION ASSOCIATED WITH SLEW MOTION

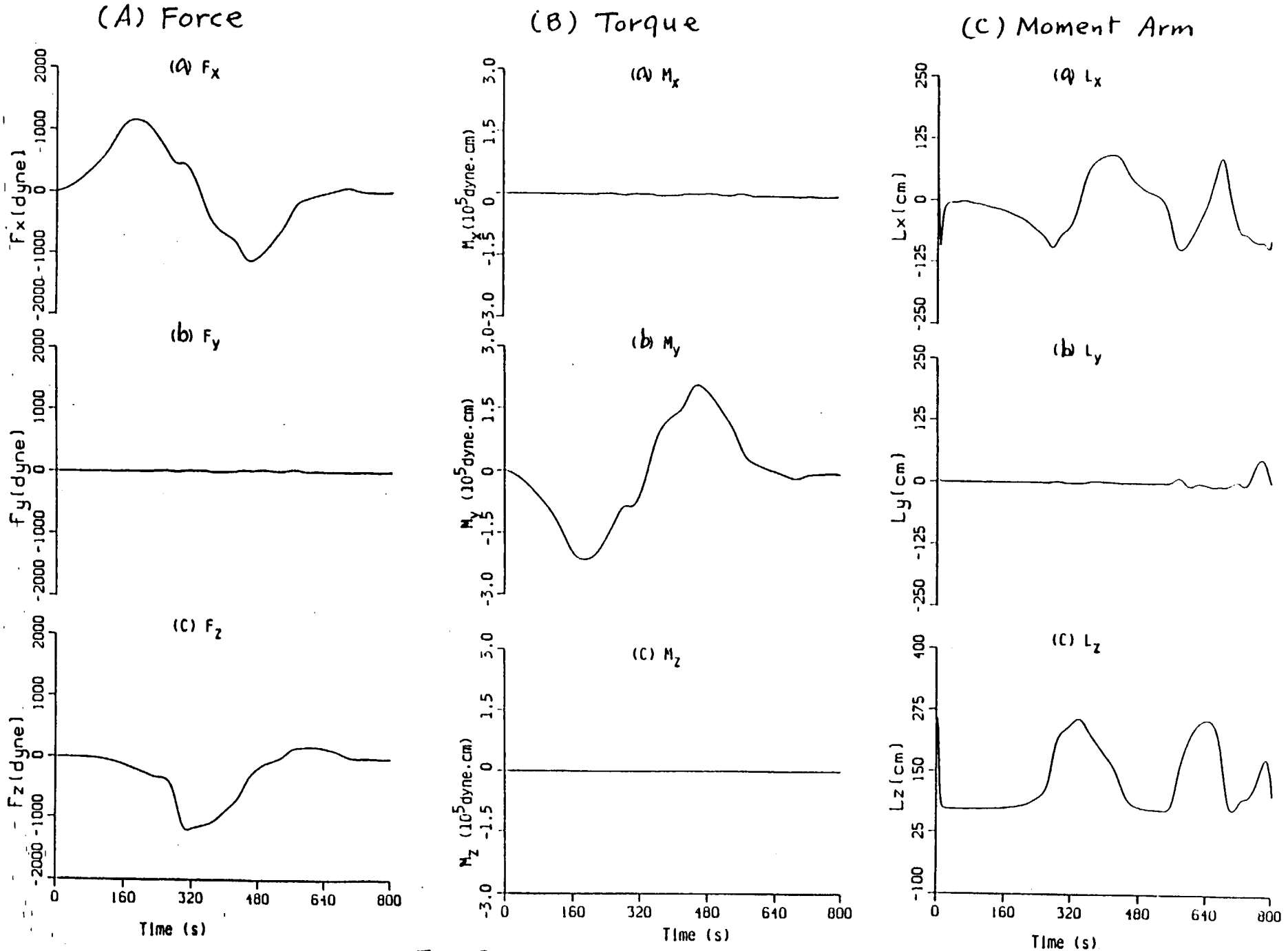

Fig. 13

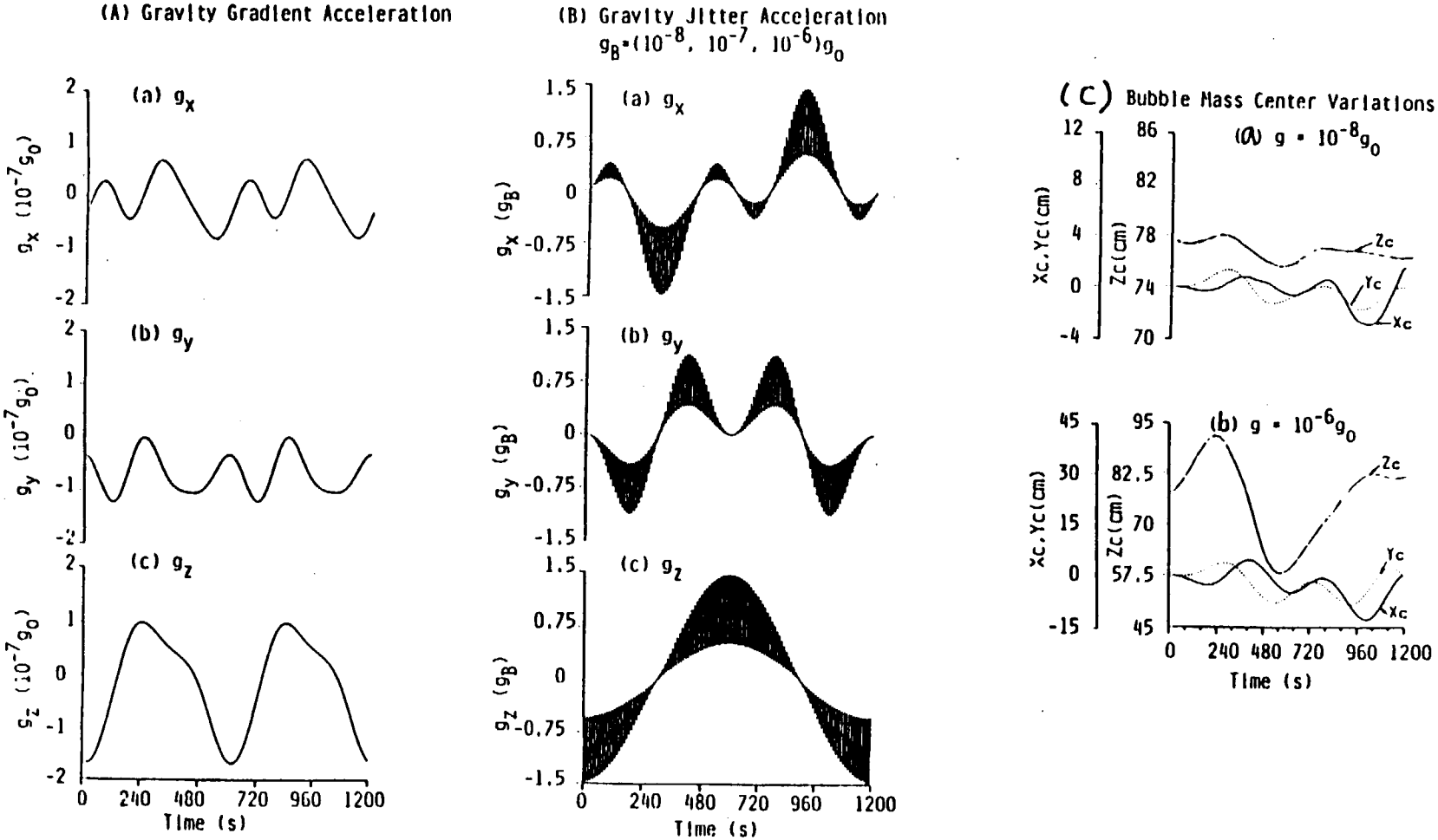
(A) Gravity Gradient Acceleration
(a) g_x
(b) g_y
(c) g_z
g_x ($10^{-7}g_0$)
g_y ($10^{-7}g_0$)
g_z ($10^{-7}g_0$)
Time (s)
(B) Gravity Jitter Acceleration
$g_B=(10^{-8}, 10^{-7}, 10^{-6})g_0$
g_x (g_B)
g_y (g_B)
g_z (g_B)
(C) Bubble Mass Center Variations
(a) $g = 10^{-8}g_0$
(b) $g = 10^{-6}g_0$
Xc,Yc(cm)
Zc(cm)
Zc
Yc
Xc

Fig. 14

THREE DIMENSIONAL LIQUID AND VAPOR INTERFACE

The Effect of Gravity Jitter and Gravity Gradient

A. Gravity Gradient *Dominated*: $g = 10^{-8} g_0$

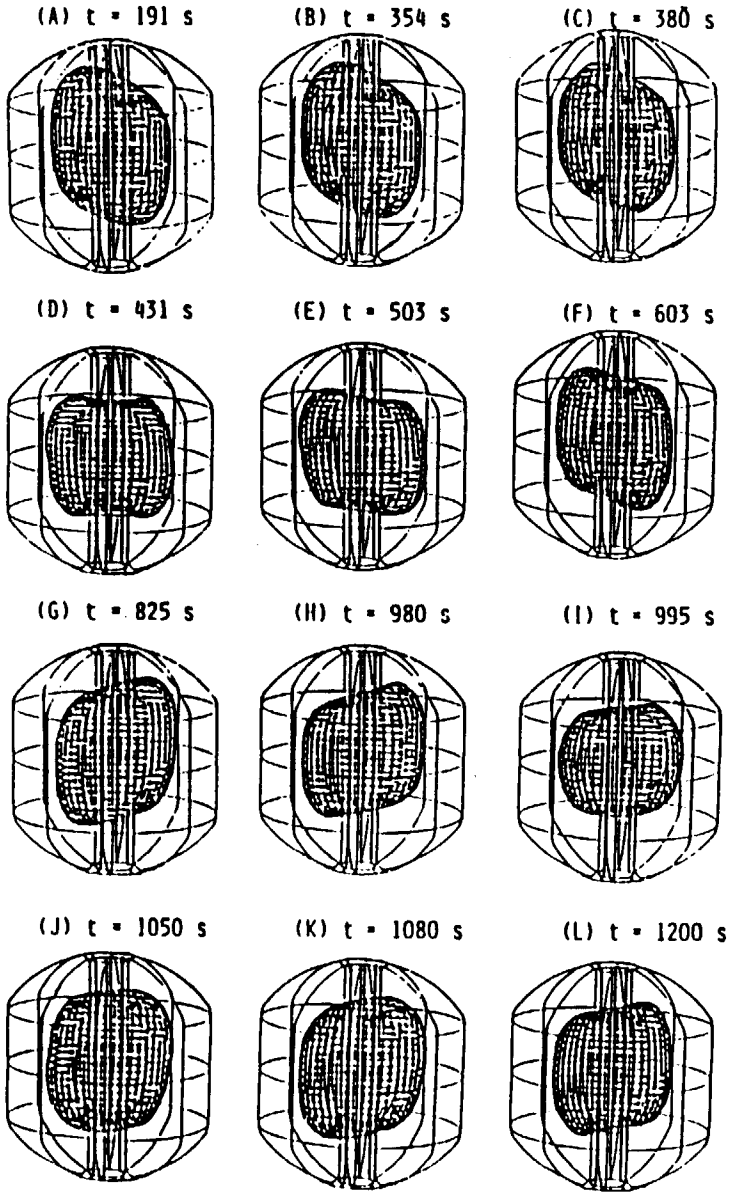

B. Gravity Jitter *Dominated*: $g = 10^{-6} g_0$

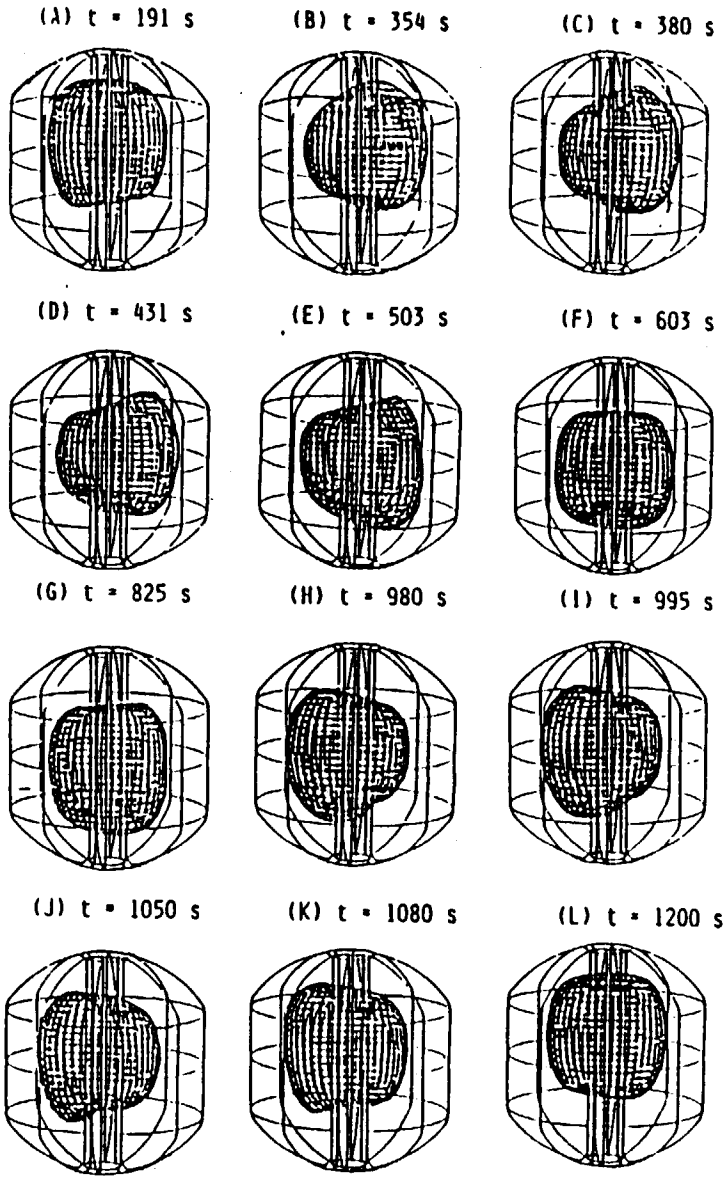

Fig. 15

Slosh Reaction Force, Torque and Moment Arm

$g = 10^{-8} g_0$, $\tau = 1200$ s

$\omega = 0.1$ rpm, $f = 0.1$ Hz

A. Force

B. Torque

C. Moment Arm

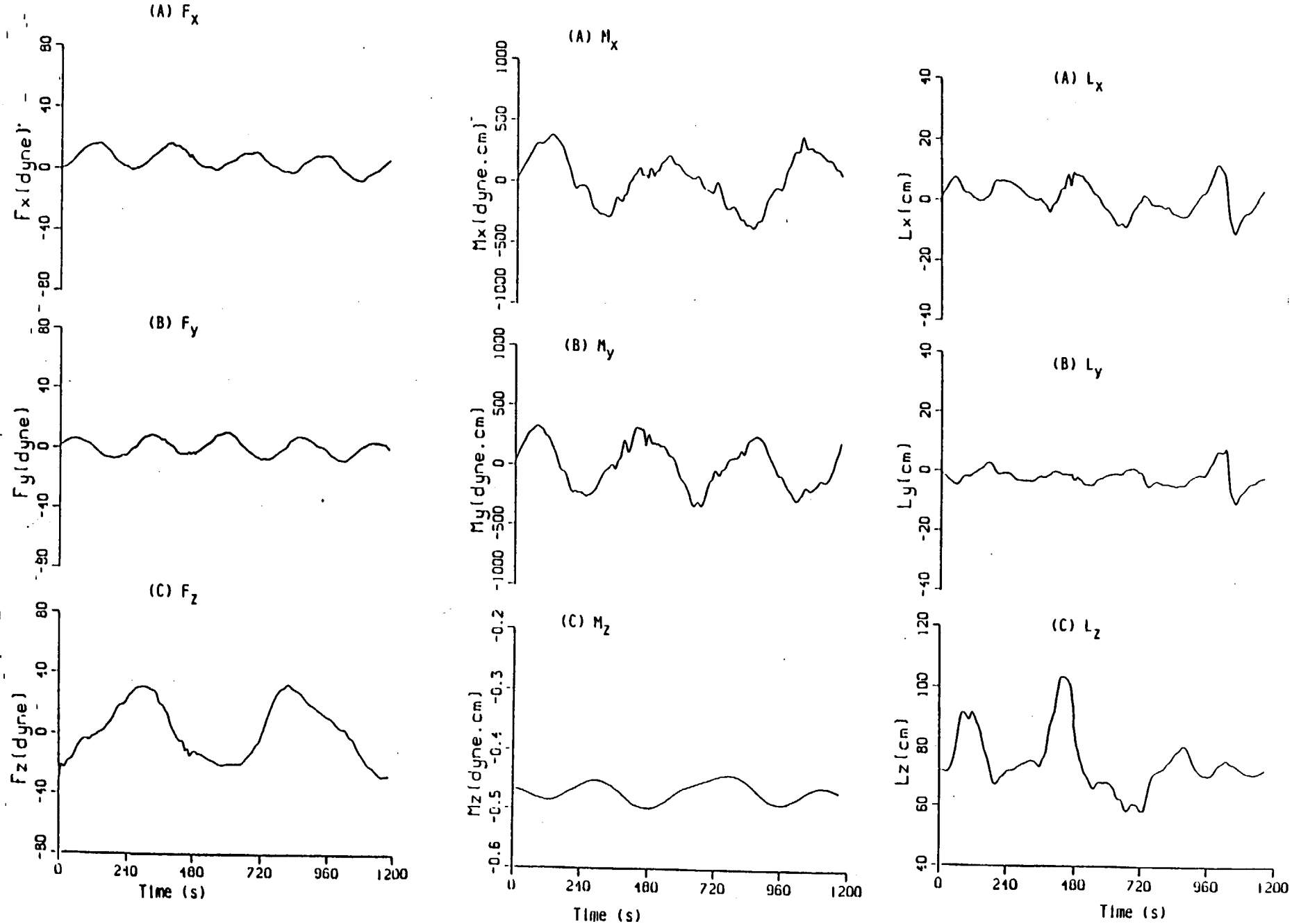

Fig 16

Slosh Reaction Force, Torque and Moment Arm

$g = 10^{-8} g_0$, $\mathcal{T} = 1200$ s

$\omega = 0.1$ rpm, $f = 0.1$ Hz

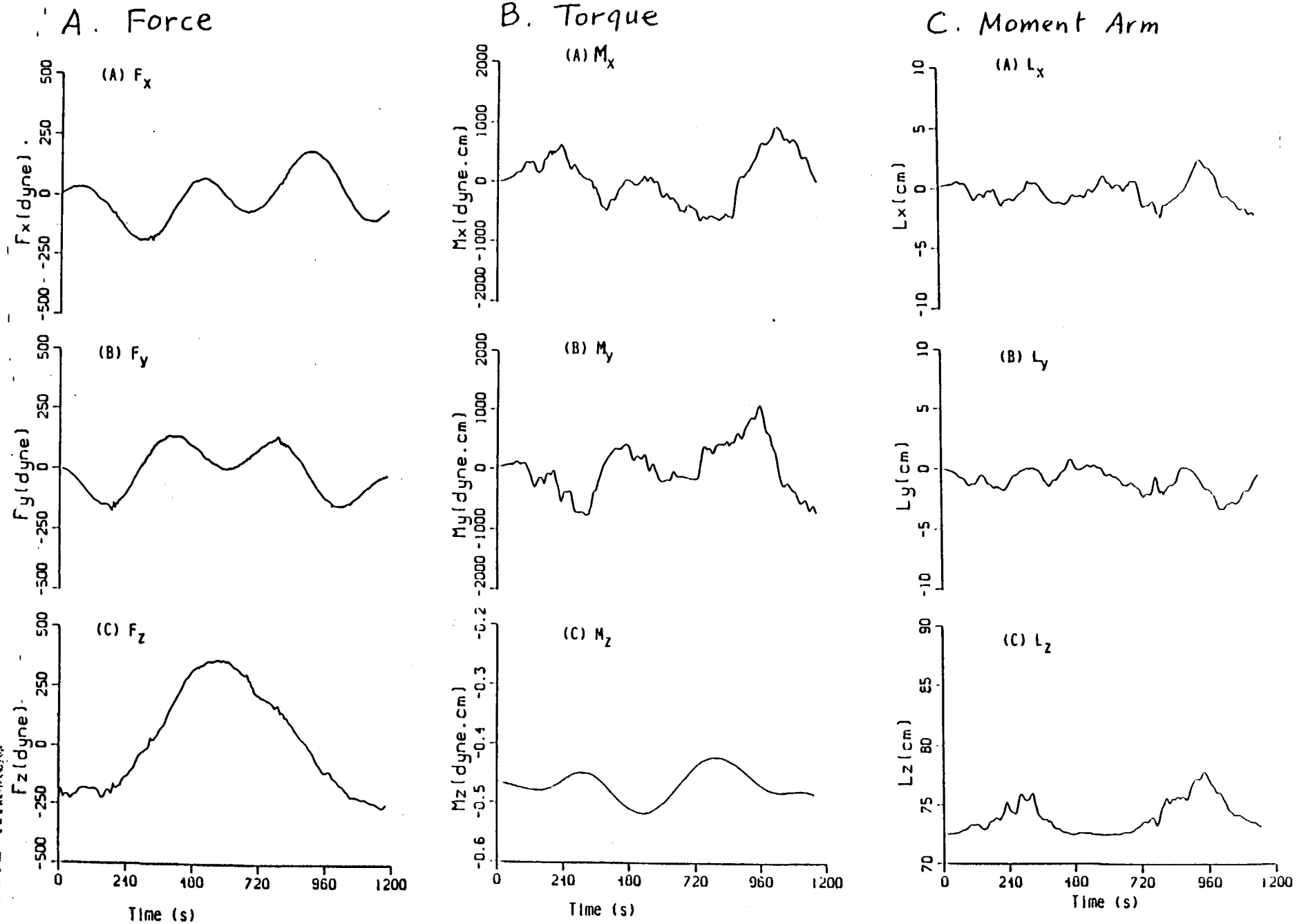

Fig 17